Title

Attosecond Extreme Ultraviolet (XUV) Probing of Ultrafast Nuclear Dynamics in Molecules

ISBN

9798276022079

Author

Ou, Jen-Hao

Publication Date

2025-12-06

Peer reviewed|Thesis/dissertation

Attosecond Extreme Ultraviolet (XUV) Probing of Ultrafast Nuclear Dynamics in Molecules

By

Jen-Hao Ou

A dissertation submitted in partial satisfaction of the

requirements for the degree of

Doctor of Philosophy

in

Chemistry

in the

Graduate Division

of the

University of California, Berkeley

Committee in charge:

Professor Stephen R. Leone, Chair

Professor Michael W. Zuerch

Professor David Attwood

Fall 2025

Attosecond Extreme Ultraviolet (XUV) Probing of Ultrafast Nuclear Dynamics in Molecules

By

Jen-Hao Ou

Abstract

Attosecond Extreme Ultraviolet (XUV) Probing of Ultrafast Nuclear Dynamics in Molecules

by

Jen-Hao Ou

Doctor of Philosophy in Chemistry

University of California, Berkeley

Professor Stephen R. Leone, Chair

Time-dependent motion (dynamics) of nuclei in molecules often occurs on ultrafast (picosecond (10^{-12} second) or femtosecond (10^{-15} second)) timescales. Experimentally, it is a question how to launch and detect these ultrafast nuclear dynamics in molecules in real time? In this dissertation, I studied two representative systems with the technique Extreme Ultraviolet (XUV)-Attosecond Transient Absorption Spectroscopy (ATAS). One is the coherent vibrational dynamics in CBr_4 in the electronic ground state of the fully symmetric stretch mode, with a period of 125 fs. The results on CBr_4 show that XUV-ATAS can resolve tiny bond-length displacements down to the order of 10^{-4} Å with 26 fs temporal resolution, with the knowledge of calculated core-excited potential energy surfaces. Such spatial and temporal resolution of XUV-ATAS is exceptional. It provides roughly 1,000 times better spatial resolution and 5 times better temporal resolution compared to the current MeV-UED at SLAC.

The other is the photodissociation dynamics of Br_2 in the electronically excited C $^1\Pi_u$ 1_u state. The presented measurement has the shortest temporal resolution (26 ± 1 fs) among all other reported time-resolved studies, to the best of our knowledge. In this work, it is found that the measured rise time varies based on the probing transition. For the atomic Br 3d $^2P_{3/2} \rightarrow$ 4p $^2D_{5/2}$ and $^2D_{3/2}$ absorptions at 64.31 and 65.34 eV, the rise times are different, 38 ± 1 fs and 20 ± 5 fs, respectively. With simulations, these results show that measured probe signals record the dissociative wavepacket dynamics and how the different probing transitions affect the apparent progress toward dissociation. These probe-dependent effects should be considered when interpreting measured signals and their timescales. In addition, the presented broadband XUV absorption spectra cover both Br 3d core-to-valence and core-to-Rydberg transitions simultaneously, and our time-resolved measurements trace out the whole transformation from Br_2 molecules to Br atoms. This work unifies the molecular and atomic static absorption spectra scattered in the literature, highlighting the distinct advantages of time-resolved absorption spectroscopy with broadband XUV light.

In particular, this dissertation is a combined study of experiments, simulations, and analytical theories. The simulated time-resolved XUV absorption spectra are compared to measured ones, which help to assign and interpret the measured spectra. In addition, analytical theories are developed or adapted from literature to describe the measured physical phenomenon. Under proper approximations, closed-form relations between key physical quantities are obtained, and the essential physical picture is revealed. This dissertation demonstrates how ATAS can be used to successfully capture and resolve ultrafast molecular dynamics, and highlights how such experiment-theory combined study effectively pinpoints and deepens our understanding of the underlying physical picture.

In honor of my mother Yi-Ling Lee and my father Chin S. Ou,
who gave me life and guide my life.

In honor of my Ph.D. advisor Prof. Stephen R. Leone,
who broadens my horizons on science, research, and education.

You raised me up to more than I can be.

Table of Content

Table of Content ii
List of Figures v
List of Tables xi
Acknowledgements xii
1 Introduction 1
2 Coherent Vibrational Dynamics in CBr_4 2
2.1 Introduction 2
2.2 Experimental Methods 4
2.2.1 400 nm Pump Pulse 4
2.2.2 Few-Cycle Visible-NIR Pulse (Driving Field for High Harmonic Generation) 4
2.2.3 XUV Probe Pulse 4
2.2.4 Static and Time-Resolved (Transient) XUV Absorption Measurement 4
2.2.5 Pump-Pulse Peak-Intensity Dependent Measurements 5
2.3 Computational Methods 5
2.4 Results and Discussion 6
2.4.1 Detection of the Coherent Vibrational Dynamics: Static and Time-Resolved XUV Absorption Spectrum of CBr_4 at Br $M_{4,5}$ $3d_{3/2,5/2}$ Edge 6
2.4.2 Information Encoded in the Time-Resolved XUV Absorption Spectrum: Oscillation Amplitude of XUV Absorption Energy, Excursion Amplitude of Vibrational Wavepacket, and Slope of Core-Excited State Potential Energy Surface 8
2.4.3 Relative Slope between Multiple Core-Excited State PES and Insight into Property of Participating Orbitals 10
2.4.4 Connection between the Excursion Amplitude of Vibrational Wavepacket and Vibrational Eigenstate Populations, in the Small-Displacement Limit 11
2.4.5 Physical Basis for the Phenomenological Equations in the Literature to Fit the Oscillations in Time-Resolved XUV Absorption Spectrum due to Coherent Vibrational Dynamics 13
2.4.6 Controlling the Motion of Vibrational Wavepacket with Different Pump-Pulse Peak Intensities in the Small-Displacement Regime 14
2.5 Conclusions 16

2.6 Appendix 17
2.6.1 Calibration of Pump Pulse 17
2.6.2 Calibration of Time Zero and Temporal Resolution for Time-Resolved XUV Absorption Measurements 21
2.6.3 Calibration of Spectral Axis 22
2.6.4 Measured Relative Slope of Br-3d Core-Excited State Potential Energy Surface (PES) 26
2.6.5 Comment about Initial Phase of Wavepacket Trajectory 26
2.6.6 Nuclear Time-Dependent Schrodinger Equation Simulations 27
2.6.7 Comment about Polarizability Calculations 28
3 Dissociation Dynamics of Br_2 C $^1\Pi_u$ 1_u State 30
3.1 Introduction 30
3.2 Methods 35
3.2.1 Experiments 35
3.2.2 Computations 35
3.3 Results and Discussion: Overview of both the Core-to-Valence and Core-to-Rydberg Absorption Spectrum 36
3.3.1 Before Dissociation: Identification of Br_2 Molecules with Static Core-to-Valence and Core-to-Rydberg Absorption Spectrum 36
3.3.2 During Dissociation: Overview of the Changes in Time-Resolved Core-to-Valence and Core-to-Rydberg Absorption Spectrum 39
3.4 During Dissociation: Changes in Time-Resolved Br Core-to-Valence Absorption Spectrum 41
3.4.1 Ground State Bleaching: Decrease of Br_2 Molecules in The Electronic Ground State (X) 42
3.4.2 Excited State Absorption: Br_2 Molecules Pumped to the Electronic Excited State (C $^1\Pi_u$ 1_u) 42
3.4.3 From Molecules to Atoms: Mapping the Motion of the Nuclear Wavepacket on the C State Potential Energy Curve (PEC) By Core-to-Valence Absorptions 42
3.4.4 Product Absorption: Buildup Signal of Dissociated Br Atoms and its Fitted Rise Time 43
3.4.5 Potential Causes for the Different Rise Times: Comparison between Experiment, Simulation and Theory 46
3.4.6 Bond Length vs Time: General Agreement across the Literature 50

3.4.7 When does a chemical bond break?....50
3.5 During Dissociation: Changes in Time-Resolved Br Core-to-Rydberg Absorption Spectrum....53
3.5.1 Challenges to Interpret the Core-to-Rydberg Absorption Spectrum....53
3.5.2 Ground State Bleaching: Decrease of Br_2 Molecules in the Electronic Ground State (X) 53
3.5.3 Product Absorption: Identification of Dissociated Br Atoms by Core-To-Rydberg Absorption Spectrum at Long Time Delay....55
3.5.4 Product Absorption: Time Evolution of the Atomic Br Core-to-Rydberg Absorptions....56
3.6 Conclusions....59
3.7 Appendix....59
3.7.1 Experimental Method: Time-Resolved XUV Absorption Spectroscopy....59
3.7.2 Computational Method....65
3.7.3 Potential Pathway for Dissociation Product Br ($^2P_{3/2}$) + Br* ($^2P_{1/2}$)....68
3.7.4 Ground State Bleaching: Coherent Vibrational Dynamics in the Electronic Ground State 70
3.7.5 The Relative Polarization of 400 nm Pump and XUV Probe Pulses and its Potential Implications....73
4 Conclusions and Prospect....74
References....75

List of Figures

Figure 2.1. Experimental Scheme. (a) Attosecond transient absorption spectroscopy on the symmetric stretch (a_1) mode of CBr_4. (b) Vibrational eigenstates are coherently excited by non-resonant impulsive stimulated Raman scattering (ISRS) with a 400 nm 26 fs pump pulse, and a vibrational wavepacket is launched on the electronic ground state potential energy surface. (c) Vibrational wavepacket dynamics are monitored by time-resolved absorption of attosecond XUV probe pulses (purple arrows) from the electronic ground state to the $(Br\text{-}3d_{3/2,5/2})^{-1}10a_1^*$ electronic core-excited states around 70 eV. The wavepackets drawn in green and red represent the motion shifting toward negative and positive normal mode displacement q, respectively. 3

Figure 2.2. (Left) Static XUV absorption spectrum of CBr_4 at Br $M_{4,5}$ $3d_{3/2,5/2}$ edges from the electronic ground state to the $(Br\text{-}3d_{3/2,5/2})^{-1}10a_1^*$ core-excited states. The spin-orbit doublet is resolved by fitting to a sum of two Voigt functions. The extracted peak energies are 70.932±0.011 and 69.903±0.008 eV for the Br M_4 $3d_{3/2}$ and M_5 $3d_{5/2}$ edges respectively, with a 1.03±0.01 eV spin-orbit splitting. (Right) Time-resolved XUV absorption spectrum of CBr_4 as a function of time delay between the 400 nm pump and XUV probe pulses. The positive time delay is when the 400 nm pulse arrives before the XUV pulse. The peak intensity of pump pulse is 20.2×10^{12} W/cm^2. Color shade: extracted peak energy with error bars at each time delay. Solid line: a sine function fitted to the extracted peak energies. The fitted period is 123±1 fs, amplitude 10.2±1.4 meV, center 70.934±0.001 eV (black dashed line) for the M_4 $3d_{3/2}$ edge, while the M_5 $3d_{5/2}$ edge yields 123±1 fs, 11.3±1.4 meV, and 69.903±0.001 eV (black dashed line). The oscillations for the two edges are almost temporally in phase with a 0.1±0.4 rad phase difference. 7

Figure 2.3. Computed XUV excitation energies from ROKS along the symmetric stretch a_1 normal mode as a function of C-Br bond length (open circles) around the equilibrium geometry (1.925 Å). The linear fits obtained from fitting to ROKS results for 41 equally spaced bond lengths between 1.9046-1.9446 Å are also shown (solid lines), which align quite well with ROKS results for twelve bond lengths calculated outside the fit interval (six equally spaced points each between 1.8746-1.8996 Å and 1.9496-1.9746 Å). The slopes are about -9.4 eV/Å for the $Br\text{-}3d_{3/2,5/2}\rightarrow10a_1^*$ excitations. 10

Figure 2.4. Calculated populations of the vibrational eigenstates (ν = 0, 1, 2) of the symmetric stretch a_1 mode from nuclear TDSE simulations, as a function of the experimental 400 nm pump-pulse peak intensity. The population of the vibrational first-excited state remains small (around the order of 10^{-3}). This shows that the pump light-matter interaction is in the small-displacement limit for the range of pump-pulse intensities used in this work. The population in the second vibrational excited state is even smaller, indicating that the two-state approximation used for the small-displacement limit is reasonable. 13

Figure 2.5. Pump-pulse peak-intensity dependence of (a) experimentally measured oscillation amplitude of the XUV absorption energy , (b) excursion amplitude of the vibrational wavepacket q_{amp} (retrieved from (a) by Equation 3, given the -9.4 eV/Å slope of the $(Br\text{-}3d_{3/2,5/2})^{-1}10a_1^*$ core-excited state PES from ROKS calculations), and (c) square root of the population transferred to the vibrational first-excited state $\sqrt{p_1}$ (estimated from (b) by Equation 9). All three quantities increase approximately linearly with the pump-pulse intensity for both the Br M_4 $3d_{3/2}$ (orange circle) and M_5 $3d_{5/2}$ (blue square) edges. Estimates

of all three quantities from nuclear TDSE simulations (black open square) for the ISRS process are also provided (scaled by 1/3, see text for details), and show clear linear relationships with the pump-pulse intensities used in this work. The outlier at 10.3×10^{12} W/cm^2 may result from the fluctuation in average power measurement, as the average power is close to the lower limit of the working range for the power meter head (Coherent PowerMax PM10). 15
Figure 2.6. Beam diameter (mean μ) of pump pulse vs iris size. The iris size is read by the numbered marks on the iris. Measured with DataRay beam profiler WinCamD-UHR, 4xsigma mode. Picked off to the location at the same distance to the sample location. The beam diameter (mean μ) remains around 109 μm and does not change significantly when the iris size decreases from full to 3.0. Only when iris size is smaller than 3.0, the beam starts to get significantly cropped and the beam diameter increases appreciably. The averaged value of beam diameters from size 3.0 to full is 109 μm with 1 μm standard deviation. 17
Figure 2.7. Average power of pump pulse vs iris size. The iris size is read by the numbered marks on the iris. The average power at the sample location (red circle) is estimated as 65% of that measured right after the iris (black square), according to a previous power calibration. There are 5 mirrors and 1 thin glass window between the iris and the sample cell. 18
Figure 2.8. Self-Diffraction Frequency-Resolved Optical Gating (SD-FROG) measurement for 400 nm pump pulse. (a) Measured and (b) Reconstructed spectrogram. (c) Measured (black line) and reconstructed (black dash) spectrum, and reconstructed spectral phase (blue dash). The central wavelength is around 400 nm. (d) Reconstructed temporal intensity envelope (black line) and temporal phase (blue dash). The pulse duration is considered as 26±1 fs FWHM from fitting the main pulse to a Gaussian function. 20
Figure 2.9. The cross-correlation measurement of pump and probe pulses in He 2s2p state. The positive time delay is when the XUV pulse arrives first before the 400 nm pulse. (a) Time-resolved XUV differential absorption (ΔA) spectrum of He 2s2p state. The XUV absorption is suppressed (ΔA turns negative) by the pump pulse when pump and probe pulses overlap. (b) Circle: Lineout of negative of measured differential absorption (-ΔA) at 60.16 eV. Black solid line: Fit by a convolution of two Gaussian (main and satellite pulses) and an exponential decay function in time delay. Red dash line: Gaussian (main pulse). The fitted FWHM and center of this Gaussian is 26±6 fs and -1±3 fs, and these are taken as the instrument response function and time zero for this work, respectively. Red dash line: Gaussian (satellite pulse). 21
Figure 2.10. Static XUV absorption spectrum of He 2snp (n ≥ 2) excited states, as a function of XUV CCD camera pixel. 22
Figure 2.11. The calibration curve for wavelength vs pixel. Cross: Measured resonance location. Red line: Linear fit. This calibration curve enables the conversion from pixel to wavelength and photon energy. 23
Figure 2.12. Calibrated static XUV absorption spectrum of He 2snp (n ≥ 2) excited states, as a function of photon energy. 23
Figure 2.13. Calibrated spectrum of the XUV probe pulses after a 0.1 μm Al filter and a 0.1 μm Zr filter. The cut around 73 eV is due to the Al filter. 24

Figure 2.14. Time-resolved XUV differential absorption spectrum of CBr_4 with pump peak intensity 20.2×10^{12} W/cm^2. The positive time delay is when the 400 nm pulse arrives before the XUV pulse. The negative oscillating signals around 69 to 71 eV encode the coherent vibrational dynamics on the electronic ground state. (Upper) Differential absorption integrated from time delay of 300 to 1100 fs. Three major peaks between 64 to 66 eV correspond to dissociated atomic Br. These are likely to come from two photon absorption of the 400 nm pump pulse (photon energy 3.1 eV), because the lowest transition to valence-excited states (A bands) of CBr_4 starts at 4.9 eV (39550 cm^{-1})[66,67] 25
Figure 2.15. The initial phase at time zero from fitting the measured XUV absorption energy as a function of time-delay to a sine function for different pump-pulse intensities, plotted in the order of experiments. 27
Figure 3.1. Experimental scheme. (a) Attosecond extreme ultraviolet (XUV) transient absorption spectroscopy on the dissociation of Br_2 molecules in the C $^1\Pi_u$ 1_u state. The dissociation is launched by femtosecond 400 nm pump pulses and monitored by the time-resolved absorption of broadband XUV probe pulses at the Br $M_{4,5}$ $3d_{3/2,5/2}$ edges (66 to 80 eV). (b) Femtosecond 400 nm pump pulses bring the Br_2 molecule from the electronic ground X $^1\Sigma_g^+$ state to the excited C $^1\Pi_u$ 1_u state, to initiate the dissociation. As the nuclear wavepacket travels on the C state, it is probed by the absorptions of XUV pulses to the Br core-to-valence $(3d)^{-1}4p$ and core-to-Rydberg $(3d)^{-1}ns$ and $(3d)^{-1}np$ ($n \geq 5$) excited states. Solid lines: Calculated potential energy curves (PEC) of the ground X, C and core-to-valence $(3d)^{-1}4p$ excited states. Dashed lines: Hypothetical PEC of core-to-Rydberg excited state for illustration purposes. 32
Figure 3.2. Static XUV absorption spectrum of Br_2 molecules at Br 3d M edge (a) 3d → 4p core-to-valence and 3d → *n*s, *n*p ($n \geq 5$) core-to-Rydberg absorptions. (b) 3d → *n*s, *n*p ($n \geq 5$) core-to-Rydberg absorptions. Assignments in Table 3.3. 37
Figure 3.3. Measured time-resolved XUV core-to-valence (67-70 eV) and core-to-Rydberg (73-80 eV) absorption spectrum during the dissociation of the Br_2 C $^1\Pi_u$ 1_u state. (a) Static XUV absorption spectrum of the Br_2 molecules before dissociation. (b) Time-resolved XUV differential absorption spectrum $\Delta A(t)$ of the dissociating Br_2 molecule and resulting Br atoms, as a function of the time delay between the 400 nm pump and XUV probe pulses. Positive time delays mean the 400 nm pump pulse arrives before the XUV probe pulse. (c) Time average from 150 to 160 fs of the differential absorption signals $\Delta A(t)$ in (b). New absorptions from dissociated Br atoms lead to positive ΔA, and decreased absorptions from Br_2 molecules cause negative ΔA. Specifically, the Br_2 C state dissociates into two ground state Br atoms, which are probed by the atomic 3d $^2P_{3/2}$ → 4p $^2D_{5/2,\,3/2}$ absorptions at 64.31 and 65.34 eV, respectively. The other atomic 3d $^2P_{1/2}$ → 4p $^2D_{3/2}$ absorption is also observed at 64.89 eV, but this signal originates from another excited state of Br_2 molecules (Appendix). Above 73 eV, ground state bleaching of Br_2 core-to-Rydberg absorptions overlap with the appearance of atomic Br core-to-Rydberg absorptions. 39
Figure 3.4. Measured time-resolved XUV core-to-valence absorption spectrum during the dissociation of the Br_2 C $^1\Pi_u$ 1_u state. (a) The differential absorption spectrum at time zero $\Delta A(t = 0)$. The negative signals around 67.5-69.5 eV are the ground state bleaching of the $3d_{5/2,3/2}$ → 4p σ^* doublet of Br_2 molecules. (b) Time-resolved differential absorption spectrum $\Delta A(t)$ of the dissociating Br_2 molecule and

resulting Br atoms, as a function of the time delay between the 400 nm pump and XUV probe pulses. (c) Time average from 150 to 160 fs of the differential absorption signals ΔA(t) in (b). 41
Figure 3.5. Launch and detection of the nuclear wavepacket and dissociation in the valence excited state C. (a) Potential energy curves. (b) Measured time-resolved XUV differential absorption spectrum records the motion of wavepacket on the PEC of C state and the rise of Br atomic absorptions. White dashed line: calculated energy gap between the C state and the Br $(3d_{5/2})^{-1}4p$ core-to-valence excited state. (d, c) Lineout in time of (b) at 64.31 and 65.34 eV for atomic Br 3d $^2P_{3/2} \rightarrow$ 4p $^2D_{5/2, 3/2}$ absorptions. Black dot and gray shade: the best estimate and the uncertainty of the measured ΔA(t) values (mean and one standard deviation[88] of 93 measurements of ΔA(t) signals). Red solid line: corresponding lineout of theoretically computed (GAMESS) and simulated time-resolved XUV absorption cross section from C state. Orange dash-dotted line: Fit by a Sigmoid function (Equation 1)..... 45
Figure 3.6. Comparison between experimental and simulated time-resolved XUV core-to-valence absorption spectrum and their components. The dissociated atoms are probed by the atomic 3d $^2P_{3/2} \rightarrow$ 4p $^2D_{5/2}$ and $^2D_{3/2}$ absorptions at 64.31 and 65.34 eV (black dotted line and black dash-dotted line). (a) Experimental time-resolved differential absorption spectrum. (b) Simulated time-resolved total absorption cross section $\sigma_{\mathrm{C}}^{\mathrm{total}}(\omega, t)$ of C state. It is the integral over bond length of (c) simulated bond-length dependent total XUV absorption cross section of C state $\sigma_{\mathrm{C}}^{\mathrm{total}}(\omega, R)$ and (d) simulated wavepacket trajectory on C state PEC $|\Psi_{\mathrm{C}}(R, t)|^2$. (e) Lineout of (c). 49
Figure 3.7. (a) Calculated nuclear wavepacket trajectory and its position expectation value (black solid line) on the PEC of excited state C from numerically solving the nuclear TDSE and comparison with the literature. Gray dashed lines: one and double equilibrium bond length R_{eq} = 2.28105 Å.[91] Black dashed line: Adapted with permission from Fig. 5(b) in Ref. [72]. Copyright 2002 AIP Publishing. Black dotted line: Adapted with permission from Fig. S2 in Ref. [75]. Copyright 2010 Springer Nature. Yellow square: Ref. [71]. Red cross: Ref. [74]. Green circle: Ref. [77]. (b) Pump pulse shape (the temporal intensity envelope measured by SD-FROG) used in the TDSE. The effect of small pre- and post-pulses are seen as the additional weaker trajectories before and after time zero. 51
Figure 3.8. Static and time-resolved Br 3d Core-to-Rydberg XUV absorption spectrum of Br_2 molecules and Br atoms. (a) Static absorption spectrum of the Br_2 molecules before dissociation, as assigned earlier in Figure 3.2(b) and Table 3.3. (b) Time-resolved differential absorption spectrum ΔA(t) of the dissociating Br_2 molecule and resulting Br atoms, as a function of the time delay between the visible pump and XUV probe pulses. (c) Time average from 150 to 160 fs of the differential absorption signals ΔA(t) in Figure 3.8(b). New absorptions from dissociated Br atoms lead to positive ΔA (assigned in Table 3.6), while decreased absorptions from original Br_2 molecules lead to negative ΔA. (d) Measured static absorption spectrum of Br atoms by photoelectron spectroscopy (average photon-energy resolution 0.18 eV). Adapted with permission from Ref. [82]. Copyright 1992 American Physical Society. (e) Measured static absorption spectrum of Br atoms by absorption spectroscopy (measurement accuracy ±0.03 eV). Adapted with permission from Ref. [83]. Copyright 1996 American Physical Society. 54
Figure 3.9. Differential absorption ΔA(t) signal as a function of time delay for selected Br_2 core-to-Rydberg absorptions. (a, b, c) Peaks 2, 3 and 7 in Figure 3.8(a) and Table 3.3. Black dot and gray shade: best estimate (mean) and uncertainty (one standard deviation)[88] of 93 measurements. In addition to the

ground state bleaching, a strong negative suppression signal is seen around time zero, potentially due to pump-induced effects.[95] 55
Figure 3.10. Differential absorption ΔA(t) signal as a function of time delay for selected atomic Br core-to-Rydberg absorptions in Figure 3.8(c) and Table 3.6. Black dot and gray shade: best estimate (mean) and uncertainty (one standard deviation)[88] of 93 measurements. 57
Figure 3.11. Spectrum of the broadband XUV probe pulses after a 0.1 μm Al filter and a 0.2 μm Zr filter. 60
Figure 3.12. Spectrum of 400 nm pump pulse in this work (blue solid line) and visible absorption spectrum of Br_2 from the literature.[100,101] Black solid line: total absorption cross section. Black dash-dot, dotted, and dashed lines: X ($^1\Sigma_g^+$) → A ($^3\Pi_u$ 1_u), B ($^3\Pi_u$ 0_u^+), and C ($^1\Pi_u$ 1_u) absorptions, respectively. The individual absorptions are deconvoluted according to Equation 11 in Ref. [100]. 61
Figure 3.13. Self-Diffraction Frequency Resolved Optical Gating (SD-FROG) measurement of 400 nm pump pulse. (a) Measured and (b) reconstructed spectrogram. (c) Measured (solid line) and reconstructed (dash line) spectrum. The central wavelength is around 400 nm. (d) Reconstructed temporal intensity envelope. The pulse duration is 26±1 fs FWHM from fitting the main pulse to a Gaussian function. 62
Figure 3.14. The cross-correlation measurement of 400 nm pump and XUV probe pulses in He 2s2p state. (a) Time-resolved XUV differential absorption (ΔA) spectrum of He 2s2p state at 60.16 eV (60.147 eV in the literature[65]). (b) Circles: Time trace extracted by singular value decomposition (SVD) of (a). Red solid line: Fit by an exponentially modified Gaussian function. The FWHM of the fitted Gaussian of the main pulse is 26 ± 3 fs, which is taken as the temporal resolution (instrument response function) for this work. 64
Figure 3.15. The measured and fitted absorption lineshape of He 2s2p state. Black circles: measured data. Black line: total fit of Fano-Gaussian lineshape function. Red dotted line: fitted Fano lineshape function. The fitted center E_r is 60.144 ± 0.001 meV, width Γ is 45 ± 11 meV. Blue dashed line: fitted Gaussian function. The fitted FWHM is 32 ± 14 meV, which is taken as the spectral resolution of the XUV spectrograph around this photon energy region. 65
Figure 3.16. (a) Cascade one-photon absorptions of pump pulses from the ground state to the C state, then to the Z state. (b) Experimental time-resolved XUV absorption spectrum. (c) Lineout in time from (b) at 64.89 eV for atomic Br 3d ($^2P_{1/2}$) → 4p ($^2D_{3/2}$) absorption. Black dot and gray shade: the best estimate and the uncertainty of the measured value (mean and standard deviation of 93 measurements of time-resolved spectrum). Red solid line: corresponding lineout of simulated time-resolved spectrum from 90% of C state plus 10% of Z state. 69
Figure 3.17. (a) Experimental and (b-f) simulated time-resolved XUV absorption spectrum. The lineout at long time delays indicates the branching ratio Br ($^2P_{3/2}$):Br* ($^2P_{1/2}$). The simulated spectrum from 90% of C state plus 10% of Z state (b) best agrees with the experiment (a). 70
Figure 3.18. Coherent vibrational dynamics in the ground state of Br_2 molecule. (a) Potential energy curves of the relevant electronic states. (b) Time-resolved XUV differential absorption spectrum records the vibration and the ground state bleaching. (d, c) Lineout in time at the equilibrium absorption energy (E_{eq}) 68.10 eV and 69.13 eV for the $3d_{5/2,3/2}$ → 4p σ^* absorption of Br_2 molecules. Black open circle and gray shade: the best estimate and uncertainty of measured ΔA values (mean and one standard deviation[88]

of the 93 measurements). Red solid line: total fit by Equation 13. Green dash-dot line: decay part of the fit as $\Phi(t) \times (D_1 + D_2/2)$. The apparent period of the lineout at E_{eq} is *half* of the vibrational period, as explained with the fit formula. 72

List of Tables

Table 2.1. Excitation energies (eV) of (Br-$3d_{3/2,5/2}$)$^{-1}10a_1^*$ core-excited states in CBr_4. 8
Table 2.2. Properties of pump pulse vs iris size. 19
Table 2.3. Calibration Table with He 2*sn*p (*n* = 2 to 5) States 22
Table 2.4. Energy of dissociated atomic Br 3d absorption. The presented values agree reasonably with the literature. This also confirms the validity of the spectral axis calibration. 25
Table 2.5. Measured relative slope of (Br-$3d_{3/2,5/2}$)$^{-1}10a_1^*$ core-excited state PES along the symmetric stretch mode. Relative slope is determined experimentally as the ratio of measured oscillation amplitude of XUV absorption energy ΔE_{XUV} (Br-$3d_{5/2}$)/ΔE_{XUV} (Br-$3d_{3/2}$). 26
Table 3.1. Experimental time-resolved studies on the dissociation of Br_2 C $^1\Pi_u$ 1_u state[a] 33
Table 3.2. Measurements of Br core-to-valence (3d → 4p) and core-to-Rydberg (3d → *n*s, *n*p, *n* ≥ 5) spectra of ground state Br_2 molecules and Br atoms in the literature.[25,68,80–84] 34
Table 3.3. Br core-to-valence (3d → 4p) and core-to-Rydberg (3d → *n*s, *n*p (*n* ≥ 5)) absorptions from Br_2 molecules in the electronic ground state. The corresponding spectrum is in Figure 3.2. Nomenclature of the core-to-Rydberg absorptions follows Ref. [84]. 38
Table 3.4. Br core-to-valence 3d → 4p absorptions of dissociated Br atoms. 43
Table 3.5. Calculated bond length (*R*) as a function of time (*t*) for dissociation of Br_2 molecules on the C state PEC. 52
Table 3.6. Atomic Br core-to-Rydberg 3d → *n*p (*n* ≥ 5) absorptions (Figure 3.8), assigned according to Ref. [83] 58
Table 3.7. Excitation energies from the electronic ground state ($^1\Sigma_g^+$) at the equilibrium bond length to several low-lying valence excited states of Br_2. 66

Acknowledgements

My life journey, including the chapter at Berkeley, are guided, helped, and supported by numerous people. I would like to thank my parents and family, my Ph.D. advisor Prof. Stephen R. Leone and my previous teachers and mentors, and my mentee students, collaborators and colleagues, and friends.

First, I want to thank my parents, my mother Yi-Ling Lee and my father Chin S. Ou. You gave me life and raised me up, in a worry-less situation. Moreover, you taught me what is right and wrong. You taught me to share with my friends when I have good things, instead of myself having them all. You taught me to respect my teachers, to learn as much as I can from my teachers, and be grateful, even after school, to my teachers. You say you are happy to see I am capable, and you are more than happy to see that I use my capability to help others in need. With you, I get to know Buddhism, and it is my important faith. Also I thank my grandparents and all my family members, both mother's and father's sides.

Second, I want to thank my Ph.D. advisor Prof. Stephen R. Leone. I still remember clearly the first day I stepped into Prof. Leone's office during my visit in October 2019, before my Ph.D. application. On the wall pinned the photos of students and their names. From that "Board of Students", I immediately see your sincere care about students. To Prof. Leone, there are too many things to thank. If I were to summarize into several points, that would be: thank you for your trust in me. Even though I came from a computational chemistry background, with only four months of experience with optics and lasers, you are still willing to trust me, hand over D39 to me, and greatly support me throughout my Ph.D. It is until very recently, when I started to know more about the faculty career, that I realized how expensive and sophisticated D39 is, and how rare such an opportunity to learn and use this kind of beamline is. I greatly appreciate my privilege to work in D39. In addition, thank you for your patience. Coming to Berkeley, I felt as if I am climbing a steep cliff. I feel I learn rather slowly, and often it took a long time for me to correct my errors and implement the better way you suggested. However, I am truly thankful to your patience with me, allowing and waiting for me to digest and grow. In contrast, I realize how impatient I was when I started to collaborate with junior students. More importantly, I am greatly indebted to you for your tremendous support and care, helping and guiding me thru an unexpected time in my life. I truly hope I will become a great and kind professor, pass the guidance and support I receive to the future generations and generations of students, continue to help them to be motivated and inspired, and walk into their bright futures with courage.

Meanwhile, I want to thank all my previous teachers and mentors. It is like a marathon, and all of you together helped me get thru the checkpoints and milestones one by one, and finally I can be here. Special call out to Yuki and Kristina, my leading mentors and role model, John E. Beetar, my laser and optics mentor, Prof. Shang-Da Yang, my laser intern advisor, Prof. Jin-Bih Yaw, my undergraduate advisor in NTU, Dr. Yew Kam Ho, my undergraduate advisor in IAMS, Prof. Chun-Yi Lu, my General Chemistry and Mathematics for Chemistry instructor, and Prof. Yuan-Chung Cheng, my freshman mentor. You helped me build a concrete and long-lasting foundation, not only in science but also in life attitude and philosophy.

Third, I want to thank my mentee students, collaborators and colleagues, and friends. I want to thank Maria, Marko and Danny. Although it may seem that you are learning from me, actually I learned

more, way more than science, from you. I greatly appreciate the opportunity to collaborate with you and grow together. I want to thank Diptarka Hait and Patrick Rupprecht, my research collaborators, for our fruitful interactions, Jonah and Nicki as my cohort company, all Leone Group members, and all friends in Berkeley and Bliss and Wisdom Foundation of Northern California (BWNC). You are an integral part of my life in Berkeley.

You raised me up to more than I can be. Thank you and share with you!

1 Introduction

Ultrafast nuclear dynamics in molecules, or the time-dependent motion of nuclei, are critical in chemistry and they encompass various phenomena. By ultrafast, it means that these dynamics occur on the timescale of picoseconds (10^{-12} second) or femtosecond (10^{-15} second).[1] For instance, the period of a fully symmetric C-H stretch vibration of CH_4 is 11 fs. Dissociation of ICN happens on the order of 100 to 200 fs.[2] Isomerization of rhodopsin (from 11-*cis* to all-*trans* form) is approximately 100 fs.[3] The Jahn-Teller distortion of CH_4^+ from T_d to C_{2v} is approximately 10 fs.[4] However, although ultrafast nuclear dynamics are seemingly common, capturing and resolving them experimentally is not trivial due to the fine time resolution. My research question is: How to launch and detect in real time ultrafast nuclear dynamics in molecules? Specifically, I consider two representative cases for different interplays of electronic and nuclear motions. First is the coherent vibrational dynamics in CBr_4 in the electronic ground state.[5] Second is the photodissociation dynamics of the Br_2 molecule in the electronically excited C $^1\Pi_u$ 1_u state.[6]

In 1987, Zewail and coworkers first employed femtosecond spectroscopy with ultraviolet and visible light to study the dissociation of ICN.[2,7] This technique offers sub-picosecond temporal resolution and first experimentally measured the ultrafast dynamics in molecules. The field of Femtochemistry was opened, and Zewail was awarded the Noble Prize in Chemistry in 1999.[8] However, the pulse duration of the light used in the experiment was usually on the order of 100 fs.[2,8,9] As a result, to study other even faster ultrafast nuclear dynamics that occur on tens of fs or even few or sub fs timescale, a newer technique is needed.

Eventually came the field of attosecond spectroscopy. In 2001, attosecond pulses in the extreme ultraviolet (XUV) region were reported.[10–12] This breaks the femtosecond barrier and was awarded Nobel Prize in Physics in 2023. After their invention, attosecond pulses were applied to time-resolved pump-probe spectroscopy, and this led to a new technique Attosecond Transient Absorption Spectroscopy (ATAS). XUV-ATAS is essentially time-resolved XUV absorption spectroscopy and is in the family of core-level spectroscopy.[13] In 2010, ATAS first successfully measured the valence electron dynamics in krypton ions.[14] Later there was a blossom of ATAS experiments applied to various atoms, molecules and condensed matter systems.[15–19]

In this dissertation, the presented research synthesizes experiments, simulations, and theory. The experimental data (measured time-resolved XUV absorption spectrum) are compared and tested against simulations. Furthermore, to gain deeper insight into the physics behind the experiments and simulations, theory and analytical formulations are used to pinpoint and qualitatively explain the experimental results. Under appropriate approximations, the key physical pictures are revealed, which are able to explain the essence of the experiments. These experimental and computational methods are directly described in the relevant locations of the chapters, instead of one combined, standalone chapter.

2 Coherent Vibrational Dynamics in CBr_4

The material in this chapter has been published and is reprinted with permission from

Ou, J.-H.; Hait, D.; Rupprecht, P.; Beetar, J.E.; Martínez, T. J. and Leone, S. R*.
"Attosecond Probing of Coherent Vibrational Dynamics in CBr_4."
Journal of Physical Chemistry A, **2024,** *128,* 9208-9217.

*Correspondence author

2.1 Introduction

Preparing and controlling vibrational coherent superposition states (referred to as vibrational wavepackets) in molecules with light is a major theme in light-matter interactions.[20,21] This necessitates control over the creation, detection, and manipulation of the vibrational wavepacket.[20,21] In this work (Figure 2.1), such control is achieved in the carbon tetrabromide (CBr_4) molecule by attosecond transient absorption spectroscopy (ATAS).[14,17,18] I employ a 400 nm 26 fs pump laser pulse to generate a vibrational wavepacket in the symmetric stretch (a_1) mode of the electronic ground state of CBr_4 with non-resonant impulsive stimulated Raman scattering (ISRS).[22–24] The resulting vibrational wavepacket dynamics are subsequently monitored by time-resolved absorption of attosecond extreme ultraviolet (XUV) probe laser pulses at the Br $M_{4,5}$ $3d_{3/2,5/2}$ edge around 70 eV, recorded as temporal oscillations in XUV absorption energy. Alternatively, in the electronic state picture, the XUV probe corresponds to the absorption from the electronic ground state to the $(Br\text{-}3d_{3/2,5/2})^{-1}10a_1^*$ electronic core-excited states. Here the -1 superscript notation indicates the excitation from that core orbital to the $10a_1^*$ orbital.

Similar vibrational dynamics in various molecules have been experimentally observed via transient absorption spectroscopy probed at XUV or soft X-ray regions.[18,25–44] Vibrational wavepackets were triggered by pump pulses mostly in the infrared (780, 800, 1200 or 1600 nm),[25–37,41–44] while some in visible[38] or UV[39,40] spectral regions. Among them, pump pulses with high (~10^{14} W/cm^2) peak intensity[25,26,28–36,43,44] often lead to large vibrational amplitudes. In particular, relatively few works[42,43] systematically measured how the pump-pulse peak intensity affects vibrational dynamics. In this work, 400 nm pulses with lower peak intensities (8.1-20.2×10^{12} W/cm^2) are employed, and the dependence of vibrational dynamics on pump-pulse peak intensity is investigated in the small-displacement limit.[42]

To gain a deeper understanding, it is valuable to explicitly understand how the temporal oscillations in XUV absorption energy connect the shape of the corresponding core-excited state potential energy surface (PES) with aspects of the vibrational wavepackets, such as the excursion amplitude of the wavepacket and populations in the vibrational eigenstates. To clearly establish these connections, analytical relations for the above quantities are derived in the small-displacement limit with the harmonic approximation. The slope of the Br 3d core-excited state PES along the symmetric stretch

mode at the ground state equilibrium geometry is computed from restricted open-shell Kohn-Sham (ROKS) calculations.[45–47] This slope is used to retrieve the excursion amplitude of the vibrational wavepacket (in terms of C-Br bond-length displacement) and the population transferred by ISRS to the vibrational first-excited state in the small-displacement limit, from the measured time-resolved XUV absorption spectrum.

Experimentally, the results show that XUV ATAS is capable of resolving small bond-length changes during vibrational wavepacket dynamics to the order of 10^{-4} Å with femtosecond temporal resolution. Moreover, with analytical formulations, I offer a clear physical picture on multiple levels of understanding for how the pump-pulse peak intensity controls vibrational dynamics launched by non-resonant ISRS in the small-displacement limit.

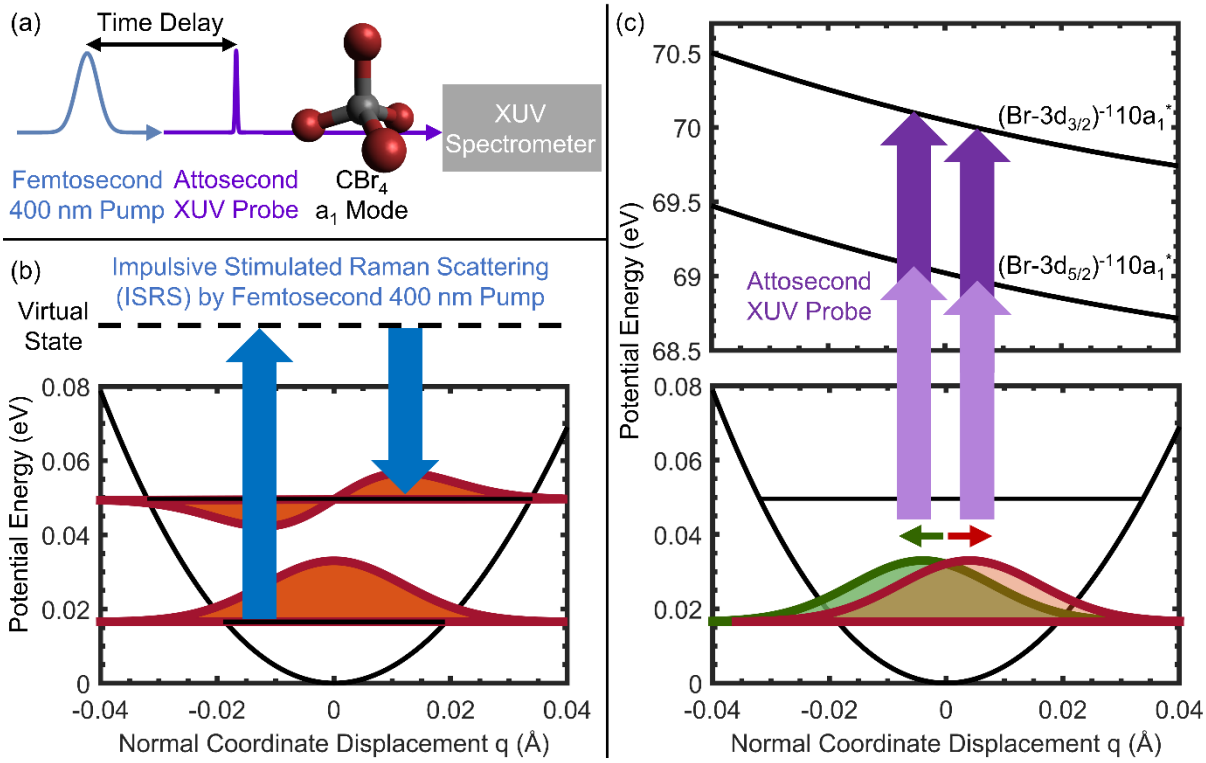

Figure 2.1. Experimental Scheme. (a) Attosecond transient absorption spectroscopy on the symmetric stretch (a_1) mode of CBr_4. (b) Vibrational eigenstates are coherently excited by non-resonant impulsive stimulated Raman scattering (ISRS) with a 400 nm 26 fs pump pulse, and a vibrational wavepacket is launched on the electronic ground state potential energy surface. (c) Vibrational wavepacket dynamics are monitored by time-resolved absorption of attosecond XUV probe pulses (purple arrows) from the electronic ground state to the $(Br\text{-}3d_{3/2,5/2})^{-1}10a_1^*$ electronic core-excited states around 70 eV. The wavepackets drawn in green and red represent the motion shifting toward negative and positive normal mode displacement q, respectively.

2.2 Experimental Methods

The scheme of attosecond transient absorption spectroscopy on CBr_4, the 400 nm pump pulse, and the XUV probe pulse, are briefly outlined here and in Figure 2.1. The laser source is a Coherent Astrella USP (800 nm, 35 fs FWHM, 7 mJ, 1 kHz), and its output is split by a 70:30 beamsplitter into pump and probe arms, respectively.

2.2.1 400 nm Pump Pulse

The pump arm starts with 70% of the Astrella output (800 nm, 35 fs FWHM, 4.9 mJ) and undergoes second harmonic generation (SHG) in a β-barium borate (BBO) crystal and the central wavelength becomes 400 nm. Then it is free-space focused through a Ne-filled (1.7 bar) tube (1.37 m long) to gently broaden the spectrum, and then compressed by chirped mirrors. The pulse duration of the main peak in the intensity envelope is measured to be 26±1 fs FWHM by homebuilt Self-Diffraction Frequency Resolved Optical Gating (SD-FROG) (Figure 2.8).

2.2.2 Few-Cycle Visible-NIR Pulse (Driving Field for High Harmonic Generation)

The probe arm starts with 30% of the Astrella output (800 nm, 35 fs FWHM, 2.1 mJ) and is focused into a Ne-filled (2.4 bar) hollow core fiber (HCF) (1.5 m long, 400 μm inner diameter), where it undergoes supercontinuum generation, and then the pulses are compressed by chirped mirrors. After the chirped mirrors, the spectrum spans from around 500 to 900 nm. The dispersion is further fine tuned by a piece of 2 mm thick ADP crystal and a pair of thin glass wedges. The output is few-cycle (~ 4 fs) visible-NIR pulses that are used as the driving field for the high harmonic generation (HHG) into XUV region.

2.2.3 XUV Probe Pulse

The few-cycle visible-NIR pulses (referred as the driving field) are focused into a Ne gas cell (~80 mmHg, 300 μm hole diameter) and an XUV probe attosecond pulse train (~50-85 eV photon energy) is produced by high harmonic generation (HHG). The remaining 800 nm driving field is removed by an Al filter (0.1 μm thick).

2.2.4 Static and Time-Resolved (Transient) XUV Absorption Measurement

At the sample cell (4 mm long, 500 μm hole diameter), 400 nm pump and XUV probe beams recombine non-collinearly and interact with CBr_4 vapor. The sample reservoir, delivery line, and cell are heated to 100-120 ℃ to obtain enough vapor pressure from solid CBr_4. The time delay between the pump and probe pulses is controlled by changing the optical path length between the pump and probe beamlines

with a translational stage. After a Zr filter (0.1 μm thick) to block the 400 nm beam, the XUV beam is dispersed by a grating and detected on a XUV CCD camera.

Two types of XUV absorption spectra are collected experimentally. One is the static XUV absorbance $A(E_{\mathrm{EUV}})$,

$$A(E_{\mathrm{XUV}}) = -\log_{10}\frac{I_{\mathrm{XUV}}(E_{\mathrm{XUV}})}{I_{\mathrm{XUV}}^{(0)}(E_{\mathrm{XUV}})}$$

where E_{XUV} is the photon energy of XUV probe pulses, and I_{XUV} and $I_{\mathrm{XUV}}^{(0)}$ are the XUV intensity with and without the CBr_4 molecule in the cell, respectively. The other is the time-resolved (transient) XUV differential absorption $\Delta A(E_{\mathrm{EUV}}, \tau)$,

$$\Delta A(E_{\mathrm{XUV}}, \tau) = -\log_{10}\frac{I_{\mathrm{XUV+pump}}(E_{\mathrm{XUV}}, \tau)}{I_{\mathrm{XUV}}(E_{\mathrm{XUV}}, \tau)}$$

where τ is the time delay between the pump and probe pulses, and $I_{\mathrm{XUV+pump}}$ and I_{XUV} are the XUV spectrum of CBr_4 with and without the pump pulse.

Temporal resolution is calibrated with a cross-correlation measurement of 400 nm pump and XUV probe pulses on the He 2s2p state. The fitted instrument response function is 26±6 fs and the time zero is 1±3 fs. The spectral axis is calibrated with a static XUV absorption spectrum of He 2s*n*p ($n \geq 2$) states. Details are in the Appendix.

2.2.5 Pump-Pulse Peak-Intensity Dependent Measurements

The peak intensity of the 400 nm pump pulse is modified by cropping the beam with an iris, before the pump and probe pulses recombine. The peak intensity at the sample cell location is estimated to range from 8.1 to 20.2×10^{12} W/cm^2. Detailed calibrations are given in the Appendix.

2.3 Computational Methods

Quantum chemical calculations are performed with the Q-Chem software package,[48] utilizing the SCAN0 functional[49] and the decontracted (i.e. all primitives are uncontracted) aug-cc-pVTZ basis set.[50–52] Scalar relativistic effects are included through the use of the spin-free exact two component one-electron (SF-X2C-1e) approach.[53–56] Local exchange-correlation integrals are calculated by quadrature over a radial grid with 250 points and an angular Lebedev grid with 974 points. The electronic ground state is modeled with the standard restricted Kohn-Sham procedure,[57] yielding an equilibrium bond distance of 1.925 Å (vs an experimental[58] value of of 1.942 Å) and a symmetric stretch frequency of 282 cm^{-1} (vs 267 cm^{-1} from experiment[59]).

The isotropic polarizability of the molecule is computed via finite differences of the energy with a five-point stencil (using electric field strengths of 0.005 and 0.01 a.u., see Appendix) over bond lengths ranging from 1.8246–2.046 Å (in increments of 0.001 Å). These polarizabilities are subsequently utilized to carry out nuclear time-dependent Schrödinger equation simulations of the ISRS process induced by the pump laser pulse and the resulting nuclear dynamics along the symmetric stretching mode, as described in detail in the Appendix.

The Br 3d excitation energies are computed with the ROKS approach,[45,46] which has been found to be quite effective at modeling core-level spectroscopies.[47,60] Excited state orbital optimization is carried out with the square gradient minimization algorithm.[61] Spin-orbit effects are subsequently incorporated in the manner described previously[47]. This quasi-degenerate perturbation-theory-based approach constructs a zeroth-order effective Hamiltonian of the spin-orbit free 3d excitation energies at a given geometry, to which a spin-orbit coupling operator $-J\,\vec{L}\cdot\vec{S}$ is added (where $\vec{S}$ is the electron spin operator and $\vec{L}$ the orbital angular momentum for d electrons). The coupling constant J is assumed to be constant for all geometries and chosen to be 0.40 eV since this value reproduces the experimentally observed multiplet splitting of 1.03 eV between the $3d_{5/2}$ and $3d_{3/2}$ absorption energies. Core-level excitation energies are computed over bond lengths ranging from 1.9046–1.9446 Å, in increments of 0.001 Å, and are fitted to a straight line against the bond length (see Figure 2.3) in order to determine the slope of the core-excited PES vs bond elongation.

2.4 Results and Discussion

2.4.1 Detection of the Coherent Vibrational Dynamics: Static and Time-Resolved XUV Absorption Spectrum of CBr_4 at Br $M_{4,5}$ $3d_{3/2,5/2}$ Edge

Figure 2.2 (left) shows the static XUV absorption spectrum of CBr_4 from the electronic ground state to the $(Br\text{-}3d_{3/2,5/2})^{-1}10a_1^*$ core-excited states ($10a_1^*$ is the lowest energy antibonding orbital[62,63]). The spin-orbit doublet is resolved by fitting to a sum of two Voigt functions. The extracted peak energies are 70.932±0.011 and 69.903±0.008 eV for the Br M_4 $3d_{3/2}$ and M_5 $3d_{5/2}$ edges, respectively (three decimal places are included here to compare with the very small (few to tens of meV) oscillation amplitude of XUV absorption energy measured and discussed below). The spin-orbit splitting is 1.03±0.01 eV (Table 2.1). They agree reasonably with previous experimental results[62] (70.5 and 69.6 eV). ROKS calculations yield slightly lower excitation energy values of 70.05 and 69.02 eV, indicating a somewhat larger difference between theory and the current experiment (~0.9 eV) than the ~0.3 eV deviations previously observed for the K- and L- edges of lighter elements.[47,60]

Next, the changes to the XUV absorption due to the vibrational wavepacket launched by 400 nm pump pulse (peak intensity 20.2×10^{12} W/cm^2) are considered. In the time-resolved XUV absorption

spectrum in Figure 2.2 (right), when the vibrational wavepacket travels back and forth on the electronic ground state PES, the XUV absorption peak oscillates correspondingly with the vibrational period. The fitted periods are 123±1 fs for both the Br M_4 $3d_{3/2}$ edge and M_5 $3d_{5/2}$ edge, which agrees with the literature value of 126 fs for the symmetric stretch mode (267 cm^{-1}).[59] The oscillations in the peak position for the two edges are almost temporally in phase with a 0.1±0.4 rad phase difference. Oscillatory behaviors corresponding to the other normal modes of the molecule are not observed (despite such modes being Raman active) because there is no net displacement along such asymmetric modes, as has been observed and discussed in a previous work for CCl_4.[44]

If the launching mechanism of the vibrational wavepacket is a pure non-resonant ISRS from a Gaussian pump pulse centered at time zero, the expectation value of wavepacket position will be a sine function with a zero initial phase.[22,24] Nuclear TDSE simulations reproduce this expectation by retrieving around 0.01 π initial phase of wavepacket position for all intensities, using the temporal intensity envelope of the pump pulse retrieved from SD-FROG (Figure 2.8). Experimentally, there may be a growing time-zero drift over the course of experiments, and it seems to be reflected in the gradual deviation of the initial phase from zero. As a result, I do not attempt to determine the absolute initial phases from the experiments (Figure 2.15).

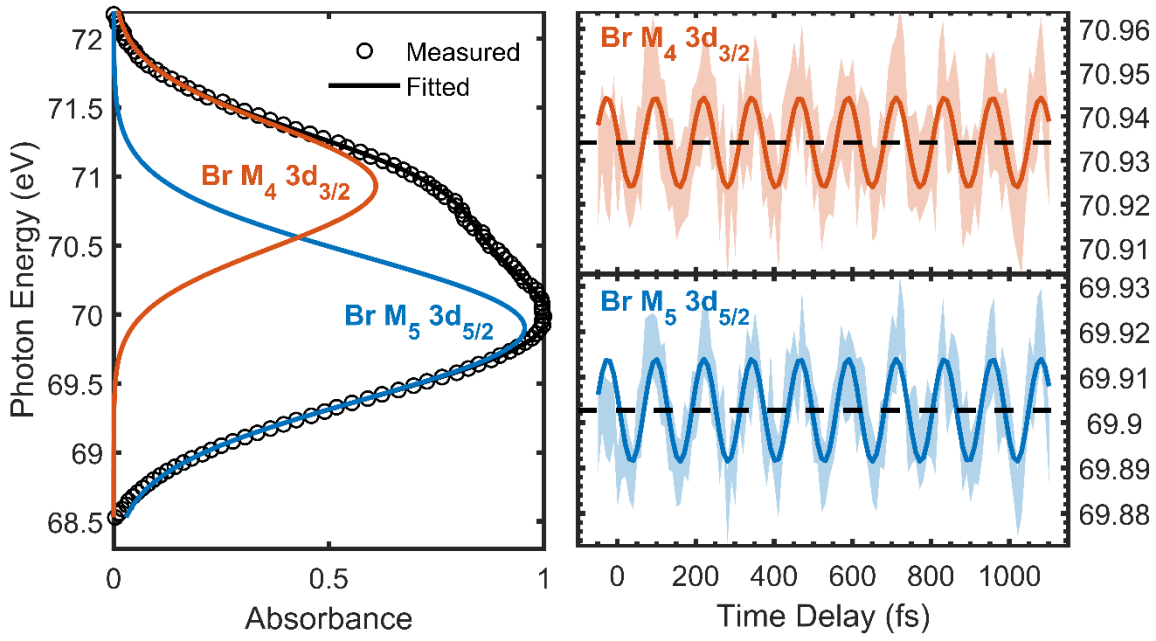

Figure 2.2. (Left) Static XUV absorption spectrum of CBr_4 at Br $M_{4,5}$ $3d_{3/2,5/2}$ edges from the electronic ground state to the $(Br\text{-}3d_{3/2,5/2})^{-1}10a_1^*$ core-excited states. The spin-orbit doublet is resolved by fitting to a sum of two Voigt functions. The extracted peak energies are 70.932±0.011 and 69.903±0.008 eV for the Br M_4 $3d_{3/2}$ and M_5 $3d_{5/2}$ edges respectively, with a 1.03±0.01 eV spin-orbit splitting. (Right) Time-resolved XUV absorption spectrum of CBr_4 as a function of time delay between the 400 nm pump and

XUV probe pulses. The positive time delay is when the 400 nm pulse arrives before the XUV pulse. The peak intensity of pump pulse is 20.2×10^{12} W/cm^2. Color shade: extracted peak energy with error bars at each time delay. Solid line: a sine function fitted to the extracted peak energies. The fitted period is 123±1 fs, amplitude 10.2±1.4 meV, center 70.934±0.001 eV (black dashed line) for the M_4 $3d_{3/2}$ edge, while the M_5 $3d_{5/2}$ edge yields 123±1 fs, 11.3±1.4 meV, and 69.903±0.001 eV (black dashed line). The oscillations for the two edges are almost temporally in phase with a 0.1±0.4 rad phase difference.

Table 2.1. Excitation energies (eV) of $(Br\text{-}3d_{3/2,5/2})^{-1}10a_1^*$ core-excited states in CBr_4.

Core-Excited State	Experiment (This work)	ROKS Calculations (This work)	Previous Experiment[62]
$(Br\text{-}3d_{3/2})^{-1}10a_1^*$	70.932±0.011	70.05	70.5
$(Br\text{-}3d_{5/2})^{-1}10a_1^*$	69.903±0.008	69.02	69.6
Spin-Orbit Splitting	1.03±0.01	1.03	0.9

2.4.2 Information Encoded in the Time-Resolved XUV Absorption Spectrum: Oscillation Amplitude of XUV Absorption Energy, Excursion Amplitude of Vibrational Wavepacket, and Slope of Core-Excited State Potential Energy Surface

When the vibrational wavepacket results in a normal mode displacement q on the electronic ground state PES $E_g(q)$, the XUV absorption energy $E_{XUV}(q)$ from the electronic ground state to the core-excited state PES $E_{ce}(q)$ is $E_{XUV}(q) = E_{ce}(q) - E_g(q)$. If the pump-pulse peak intensity is not too strong to induce a large displacement in q, the harmonic approximation holds and the XUV absorption energy $E_{XUV}(q)$ can be approximated by a Taylor series in q

$$E_{\mathrm{XUV}}(q) \approx \left[E_{\mathrm{ce}}(0) - E_g(0)\right] + \left[\left(\frac{dE_{\mathrm{ce}}}{dq}\right)_0 - \cancel{\left(\frac{dE_g}{dq}\right)_0}\right] q$$

$$= E_{\mathrm{XUV}}(0) + \left(\frac{dE_{\mathrm{ce}}}{dq}\right)_0 q \qquad (1)$$

where the slope of the electronic ground state PES $E_g(q)$ vanishes at the ground state equilibrium position $q = 0$, while the slope of the electronic core-excited state PES $E_{ce}(q)$ will generally be nonzero at the Frank-Condon region, if the equilibrium position of the core-excited PES does not coincide with that of the

ground state.

As the vibrational wavepacket travels between the outer turning point q_{ot} and the inner turning point q_{it} on the electronic ground state PES, the range of XUV absorption peak energies that can be accessed is

$$\left|E_{XUV}(q_{ot}) - E_{XUV}(q_{it})\right| = \left|\left(\frac{dE_{ce}}{dq}\right)_0\right| (q_{ot} - q_{it}) \quad (2)$$

where $\Delta E_{XUV} \equiv \left|E_{XUV}(q_{ot}) - E_{XUV}(q_{it})\right| / 2$ is defined as the *oscillation amplitude of the XUV absorption energy*, and $q_{amp} \equiv (q_{ot} - q_{it}) / 2$, the *excursion amplitude of the vibrational wavepacket*, or physically the maximum displacement from equilibrium. Therefore,

$$\boxed{\Delta E_{XUV} = \left|\left(\frac{dE_{ce}}{dq}\right)_0\right| q_{amp}} \quad (3)$$

and q_{amp} can thus be retrieved from ΔE_{XUV} in the experimentally measured time-resolved XUV absorption spectrum in Figure 2.2 (right), if the slope of the core-excited state PES along the normal mode at the electronic ground state equilibrium geometry is known.

In this work, the slope of the (Br-$3d_{3/2,5/2}$)$^{-1}10a_1^*$ core-excited states PES is calculated from ROKS to be around -9.4 eV/Å along the symmetric stretch mode (by fitting core-excitation energies to a straight line, as shown in Figure 2.3). In other words, this slope suggests that the Br-$3d_{3/2,5/2} \rightarrow 10a_1^*$ excitation energy decreases by 9.4 eV as the C-Br bond length increases by 1 Å. This is consistent with the antibonding character of the $10a_1^*$ orbital, as the energy of this state should significantly decrease with bond elongation. This 9.4 eV/Å value for the slope is in the same order of magnitude (~10 eV/Å) as previous estimates for core-to-antibonding excitations in CCl_4[44] and SF_6[42,43] (typical range 5 – 30 eV/Å depending on which atom).

The ROKS results and the linear fits are shown in Figure 2.3, which indicates that Equation 1 holds quite well for bond stretches as high as ±0.05 Å relative to equilibrium and higher order effects do not appear to be relevant in this regime. The around 10 meV or smaller experimental oscillation amplitudes for XUV absorption energies (Figure 2.2) and the computed slope -9.4 eV/Å collectively indicate that the bond stretches remain on the order of 10^{-4} to 10^{-3} Å, and the linear behavior reported in Equation 1 therefore is sufficient for analyzing the experimental results.

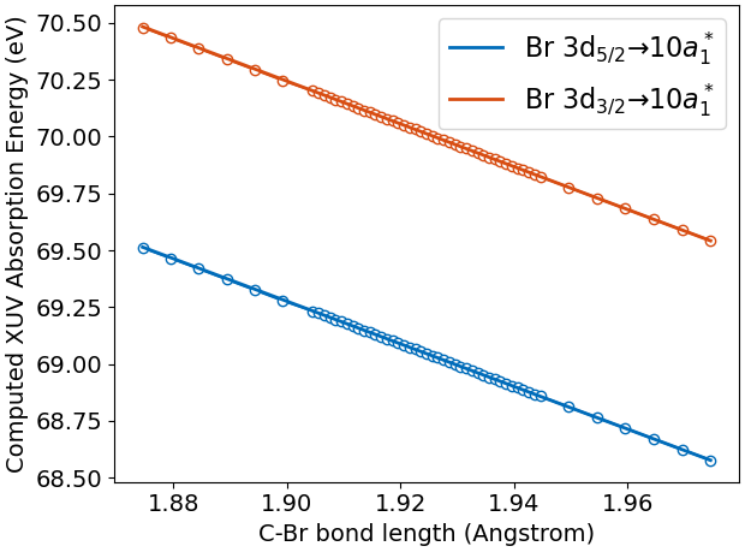

Figure 2.3. Computed XUV excitation energies from ROKS along the symmetric stretch a_1 normal mode as a function of C-Br bond length (open circles) around the equilibrium geometry (1.925 Å). The linear fits obtained from fitting to ROKS results for 41 equally spaced bond lengths between 1.9046-1.9446 Å are also shown (solid lines), which align quite well with ROKS results for twelve bond lengths calculated outside the fit interval (six equally spaced points each between 1.8746-1.8996 Å and 1.9496-1.9746 Å). The slopes are about -9.4 eV/Å for the Br-$3d_{3/2,5/2}$→$10a_1^*$ excitations.

2.4.3 Relative Slope between Multiple Core-Excited State PES and Insight into Property of Participating Orbitals

If multiple electronic core-excited states simultaneously probe the vibrational wavepacket on the electronic ground state, the *relative slope* between two or more core-excited state PES[42–44] along the normal mode at the equilibrium geometry of electronic ground state can be determined experimentally, from the ratio of measured oscillation amplitude of XUV absorption energy ΔE_{XUV} using Equation 3 as

$$\left|\left(\frac{dE_{ce2}}{dq}\right)_0\right| / \left|\left(\frac{dE_{ce1}}{dq}\right)_0\right| = \Delta E_{XUV2} / \Delta E_{XUV1} \quad (4)$$

because here the excursion amplitude of the vibrational wavepacket q_{amp} is the same. In this work, the relative slope between the two (Br-$3d_{3/2,5/2}$)$^{-1}$$10a_1^*$ core-excited states PES is determined experimentally to be 1.1±0.13 as the ratio of measured oscillation amplitude of XUV absorption energy ΔE_{XUV}(Br-$3d_{5/2}$)/ ΔE_{XUV}(Br-$3d_{3/2}$) (Table 2.5). As a result, the shape of the two core-excited state PESs are quite similar around the equilibrium geometry of the electronic ground state.

Such relative slopes not only offer experimental information on the shape of core-excited state

PES, but also shed light on the nature of participating orbitals. For the discussion below, a core-excited state is approximated as a singly excited electronic configuration, where one electron is excited from an initial core orbital to a final orbital that is higher in energy.

One scenario is when the electron is excited from the same core orbital to different final orbitals. The relative slopes of the corresponding core-excited state PESs belonging to the same absorption edge gives a hint about the bonding properties of the final orbitals. For instance, if the final orbital is non-bonding, then the resulting core-excited state will be generally less sensitive to changes in the molecular geometry, and its PES will be relatively flat. As a result, its slope will be smaller than the slope of other core-excited states PES where the final orbital is bonding or anti-bonding. For instance, in the SF_6 molecule[42,43], an electron can be excited from S-2p core orbital to three different final orbitals a_{1g}, t_{2g} and e_g. Because the a_{1g} and e_g orbitals are anti-bonding while the t_{2g} orbital is non-bonding, the slope of $(S\text{-}2p)^{-1}a_{1g}$ and $(S\text{-}2p)^{-1}e_g$ core-excited states is found to be larger than that of $(S\text{-}2p)^{-1}t_{2g}$ state.

The other scenario is when the electron is excited from different core orbitals to the same final orbital, or the corresponding core-excited states originating from different absorption edges. This offers a potential way to compare different core orbitals on the same atom, or core orbitals on different atoms in a molecule. In this work, the electron is excited to the same $10a_1^*$ anti-bonding orbital, but from different Br-$3d_{3/2}$ or Br-$3d_{5/2}$ core orbitals, corresponding to the Br M_4 or M_5 absorption edges. The ratio of slopes of these two core-excited states is close to unity as mentioned above, indicating that the both Br-$3d_{3/2}$ or Br-$3d_{5/2}$ core orbitals respond similarly to the bond-length change. This is reasonable as these two core orbitals come from the same set of Br-3d orbitals, split by spin-orbit coupling. On the other hand, a previous study on CCl_4 molecule[44] found the slope for the $(Cl\text{-}2p_{3/2})^{-1}8t_2^*$ core-excited state to be much larger than that of the $(C\text{-}1s)^{-1}8t_2^*$ core-excited state, despite the same final orbital ($8t_2^*$) for both excitations.

2.4.4 Connection between the Excursion Amplitude of Vibrational Wavepacket and Vibrational Eigenstate Populations, in the Small-Displacement Limit

In the small-displacement limit, only the vibrational ground ψ_0 and first-excited ψ_1 states of a harmonic oscillator need to be considered.[42] Long after the pump pulse, the coherent vibrational wavepacket $\Psi(q, t)$ can be approximated by the following linear superposition,

$$\Psi(q,t) = c_0\psi_0(q)e^{-iE_0t/\hbar} + c_1\psi_1(q)e^{-iE_1t/\hbar} \qquad (5)$$

where q is the normal mode displacement (position), and $E_{0,1}$ is the vibrational energy of the vibrational ground and first-excited states, respectively. The expectation value of position $\langle q(t) \rangle$ of this vibrational wavepacket is:

$$\begin{aligned}\langle q(t)\rangle &= \langle \Psi(q,t)|q|\Psi(q,t)\rangle \\ &= p_0\langle \psi_0|q|\psi_0\rangle + p_1\langle \psi_1|q|\psi_1\rangle \\ &\quad +2\sqrt{p_0 p_1}\langle \psi_0|q|\psi_1\rangle\cos[(E_1-E_0)t/\hbar+\phi]\end{aligned} \quad (6)$$

where $p_{0,1} = |c_{0,1}|^2$ is the population of the vibrational ground and first-excited states, respectively, and ϕ is the initial phase between the two coefficients $c_{0,1}$. (If the launching mechanism of the coherent vibrational wavepacket is non-resonant ISRS from a Gaussian pump pulse centered at time zero, the expectation value of position $\langle q(t)\rangle$ will be a sine function with a zero initial phase,[22,24] or equivalently a cosine function with a -π/2 initial phase in Equation 6.)

Next, because $\langle \psi_0|q|\psi_0\rangle = \langle \psi_1|q|\psi_1\rangle = 0$ and $\langle \psi_0|q|\psi_1\rangle = \sqrt{\frac{\hbar}{2\mu\omega_0}}$ for a harmonic oscillator (where μ is the mass associated with the normal mode, which is four times the mass of Br, and $\omega_0 = (E_1 - E_0)/\hbar$ is the fundamental vibrational frequency of the normal mode), the position expectation value simplifies to:

$$\begin{aligned}\langle q(t)\rangle &= \left(2\sqrt{p_0 p_1}\sqrt{\frac{\hbar}{2\mu\omega_0}}\right)\cos(\omega_0 t+\phi) \\ &= \left(2\sqrt{(1-p_1)p_1}\sqrt{\frac{\hbar}{2\mu\omega_0}}\right)\cos(\omega_0 t+\phi) \\ &= q_{\text{amp}}\cos(\omega_0 t+\phi)\end{aligned} \quad (7)$$

as $p_1 + p_0 = 1$. This shows that the excursion amplitude of the vibrational wavepacket is

$$q_{\text{amp}} = 2\sqrt{(1-p_1)p_1}\sqrt{\frac{\hbar}{2\mu\omega_0}} \quad (8)$$

Furthermore, when $p_1 \ll 1$ (as expected in the small-displacement limit),

$$\boxed{q_{amp} \approx 2\sqrt{p_1}\sqrt{\frac{\hbar}{2\mu\omega_0}}} \quad (9)$$

so q_{amp} is proportional to $\sqrt{p_1}$. Therefore, if the excursion amplitude of the vibrational wavepacket is known, the population in the vibrational first-excited state can be determined from this relation.

The validity of the above formulation is also verified against numerical simulations of the nuclear time-dependent Schrödinger equation (TDSE) along the symmetric stretch mode alone. As shown in Figure 2.4, the calculated population of the vibrational ground state is close to one (on the order of 0.99),

and the calculated population of the vibrational first-excited state is indeed small (around the order of 10^{-3}) for the pump pulse intensities used in this work. As a result, the pump light-matter interaction studied in this work is clearly in the small-displacement limit.

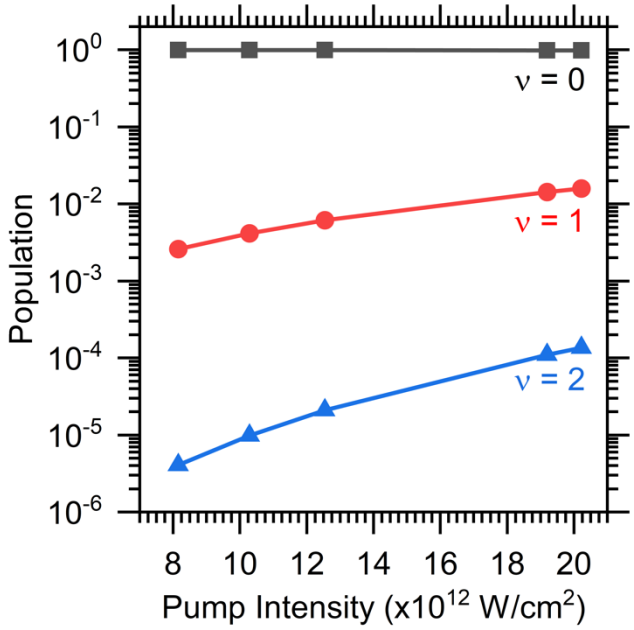

Figure 2.4. Calculated populations of the vibrational eigenstates (ν = 0, 1, 2) of the symmetric stretch a_1 mode from nuclear TDSE simulations, as a function of the experimental 400 nm pump-pulse peak intensity. The population of the vibrational first-excited state remains small (around the order of 10^{-3}). This shows that the pump light-matter interaction is in the small-displacement limit for the range of pump-pulse intensities used in this work. The population in the second vibrational excited state is even smaller, indicating that the two-state approximation used for the small-displacement limit is reasonable.

2.4.5 Physical Basis for the Phenomenological Equations in the Literature to Fit the Oscillations in Time-Resolved XUV Absorption Spectrum due to Coherent Vibrational Dynamics

Based on the formulation above, a physical basis can be provided for the phenomenological equations that have often been used in the literature,[25,28,30,39,40,43] to fit the oscillations in time-resolved XUV absorption spectrum due to coherent vibrational dynamics. If only one vibrational mode is involved, the time-resolved XUV absorption energy is often described empirically as

$$E_{\mathrm{XUV}}(t) = E^{0}_{\mathrm{XUV}} + \Delta E_{\mathrm{XUV}} \cos(\omega_0 t + \phi) \quad (10)$$

where E^{0}_{XUV} is the XUV absorption energy at the equilibrium geometry of electronic ground state, and

ΔE_{XUV} is the oscillation amplitude of XUV absorption energy. Comparing to Equation 3,

$$\Delta E_{XUV} = \left| \left(\frac{dE_{ce}}{dq} \right)_0 \right| q_{amp} \quad (3)$$

it further reveals that oscillation amplitude of XUV absorption energy ΔE_{XUV} is proportional to the slope of core-excited state PES along the normal mode at the electronic ground state equilibrium geometry and the excursion amplitude of vibrational wavepacket q_{amp}, within the harmonic approximation. Larger amplitudes can thus result from steeper slopes of the core-excited PES (which can be attained through excitation to an antibonding orbital, as in this work), or from higher pump-pulse peak intensity to access greater excursion amplitudes of vibrational wavepacket q_{amp}, by adding a greater fraction of the vibrational first-excited state in the small-displacement limit.

2.4.6 Controlling the Motion of Vibrational Wavepacket with Different Pump-Pulse Peak Intensities in the Small-Displacement Regime

The dynamics of the vibrational wavepackets are initiated with five different pump-pulse peak intensities ranging from 8.1 to 20.2×10^{12} W/cm^2 (detailed calibrations in Table 2.2). In Figure 2.5(a), the experimentally measured oscillation amplitudes of XUV absorption energy increase approximately linearly with pump-pulse intensity, which is also observed for the SF_6 molecule[42,43].

In Figure 2.5(b), the excursion amplitudes of the vibrational wavepacket q_{amp} are retrieved from the corresponding oscillation amplitudes of the XUV absorption energy ΔE_{XUV} by Equation 3, given the -9.4 eV/Å slope of the $(Br\text{-}3d_{3/2,5/2})^{-1}10a_1^*$ core-excited state PES from ROKS calculations. In Figure 2.5(c), the square root of population in the vibrational first-excited state $\sqrt{p_1}$ is further estimated from the excursion amplitude of the vibrational wavepacket q_{amp} via Equation 9. All three quantities plotted in Figure 2.5 are found to increase approximately linearly with the pump-pulse peak intensity for both the Br M_4 $3d_{3/2}$ and M_5 $3d_{5/2}$ edges.

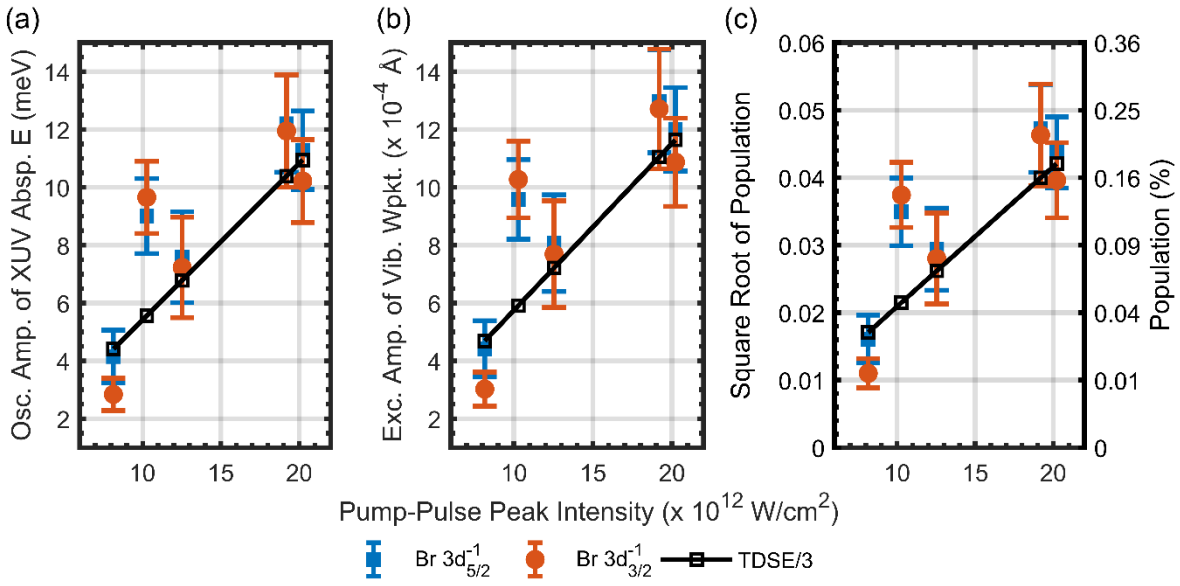

Figure 2.5. Pump-pulse peak-intensity dependence of (a) experimentally measured oscillation amplitude of the XUV absorption energy , (b) excursion amplitude of the vibrational wavepacket q_{amp} (retrieved from (a) by Equation 3, given the -9.4 eV/Å slope of the $(Br\text{-}3d_{3/2,5/2})^{-1}10a_1^*$ core-excited state PES from ROKS calculations), and (c) square root of the population transferred to the vibrational first-excited state $\sqrt{p_1}$ (estimated from (b) by Equation 9). All three quantities increase approximately linearly with the pump-pulse intensity for both the Br M_4 $3d_{3/2}$ (orange circle) and M_5 $3d_{5/2}$ (blue square) edges. Estimates of all three quantities from nuclear TDSE simulations (black open square) for the ISRS process are also provided (scaled by 1/3, see text for details), and show clear linear relationships with the pump-pulse intensities used in this work. The outlier at 10.3×10^{12} W/cm^2 may result from the fluctuation in average power measurement, as the average power is close to the lower limit of the working range for the power meter head (Coherent PowerMax PM10).

The experimentally measured and retrieved values are also compared with nuclear TDSE simulations. The theoretical population of the vibrational first-excited state p_1 and excursion amplitude of the vibrational wavepacket q_{amp} come from numerically solving the nuclear TDSE for the non-resonant ISRS process, and the theoretical oscillation amplitude of XUV absorption energy ΔE_{XUV} is estimated from Equation 3. The TDSE simulation results have to be scaled by 1/3 to match the experiment. A few possible reasons for this large discrepancy between experiment and theory are considered below. I note that the TDSE simulations account for rotational averaging effects on the interaction between the molecule and the pump pulse field through the use of isotropic polarizability.

From an experimental perspective, the differences with theory may arise from a lower effective pump-pulse peak intensity at the sample location than the estimation. A detailed calibration of the experimental peak intensity for the pump pulse is given in the Appendix, which is taken as the best estimation. However, it is uncertain whether the pump and probe pulses spatially overlap right at the

beam center of each other. If the spatial overlap is off-center, the effective pump-pulse peak intensity within the probe beam area will become smaller. Before the measurements on CBr_4, the spatial overlap was confirmed by overlapping the recombined pump beam and the HHG driving-field beam on a beam profiler at a location with equivalent distance to the sample cell, as the XUV probe beam most likely follows the same path of the HHG driving-field beam. However, if there is an angular mismatch, the overlap could be diminished and therefore be a cause of the discrepancy. On the other hand, the outlier at 10.3×10^{12} W/cm^2 may result from the fluctuations in average power measurement, as the average power is close to the lower limit of the working range for the power meter head (Coherent PowerMax PM10).

Potential computational origins of this discrepancy are errors in the Br 3d core-excited PES slope value of -9.4 eV/Å, or inadequacies in modeling the non-resonant ISRS process through TDSE (such as from errors in the molecular polarizabilities). I consider these factors to be somewhat less likely as the slope is quite consistent with previous results for other molecules, and additional effort has been invested into benchmarking molecular polarizabilities used for the TDSE simulations (see Appendix).

2.5 Conclusions

In this work, a coherent vibrational wavepacket is launched in the symmetric stretching (a_1) mode of electronic ground state CBr_4 molecule by non-resonant impulsive stimulated Raman scattering (ISRS) with 400 nm pump pulses. Dynamics of this vibrational wavepacket are studied with time-resolved absorption of attosecond XUV pulses at the bromine $M_{4,5}$ $3d_{3/2,5/2}$ edges around 70 eV, with excitations to the lowest energy antibonding ($10a_1^*$) orbital. The measured XUV absorption energies oscillate in time with the period of the symmetric stretching mode (123 fs), and the oscillation amplitude of XUV absorption energy equals the product of the excursion amplitude of the vibrational wavepacket and the slope of the Br $(Br\text{-}3d_{3/2,5/2})^{-1}10a_1^*$ core-excited state potential energy surface along this mode. Since the measured oscillation amplitude of XUV absorption energy is on the order of few to tens of meV and the slope is -9.4 eV/Å from ROKS calculations, the excursion amplitude of the vibrational wavepacket (C-Br bond-length displacement) is retrieved to be on the order of 10^{-4} to 10^{-3} Å. Harmonic approximation therefore holds quite well in this small-displacement limit.

Experiments with various pump-pulse peak intensities ($8.1\text{-}20.2\times10^{12}$ W/cm^2) show an approximately linear relationship between the intensity and the measured oscillation amplitude of XUV absorption energy, and between the intensity and the retrieved excursion amplitude of vibrational wavepacket as well. Furthermore, the excursion amplitude of vibrational wavepacket is proportional to the square root of the population in the vibrational first-excited state in the small-displacement limit. This relation enables an indirect estimate of this population from the measured oscillation amplitude of XUV absorption energy. These linear relationships are supported by analytical formulations and numerical simulations of the nuclear time-dependent Schrodinger equation along the symmetric stretching mode for the non-resonant ISRS.

The present analytical formulations and approach to extract information encoded in time-resolved XUV absorption spectra is general and can be readily applied to ISRS combined with other time-resolved electronic absorption spectroscopy probed in different spectral regions. Experimentally, the results show that XUV attosecond transient absorption spectroscopy is capable of resolving the small bond-length changes during vibration with extraordinary 10^{-4} to 10^{-3} Angstrom and tens of femtosecond precision.[42] Moreover, the analytical formulations provide a concrete and thorough understanding of how the pump-pulse peak intensity controls vibrational dynamics in the small-displacement limit.

2.6 Appendix

2.6.1 Calibration of Pump Pulse

In this work, the peak intensity of pump pulse is modified by cropping the beam with an iris before the pump and probe pulses recombine. Detailed measurements of pump-pulse properties are given below.

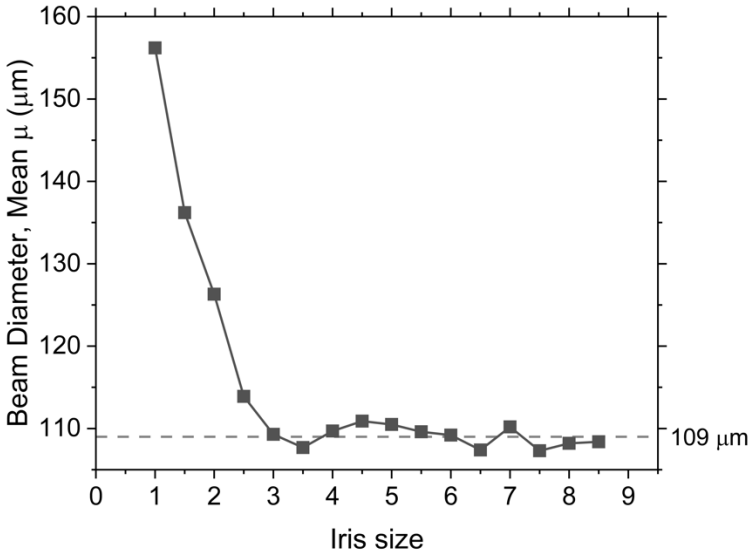

Figure 2.6. Beam diameter (mean μ) of pump pulse vs iris size. The iris size is read by the numbered marks on the iris. Measured with DataRay beam profiler WinCamD-UHR, 4xsigma mode. Picked off to the location at the same distance to the sample location. The beam diameter (mean μ) remains around 109 μm and does not change significantly when the iris size decreases from full to 3.0. Only when iris size is smaller than 3.0, the beam starts to get significantly cropped and the beam diameter increases appreciably. The averaged value of beam diameters from size 3.0 to full is 109 μm with 1 μm standard deviation.

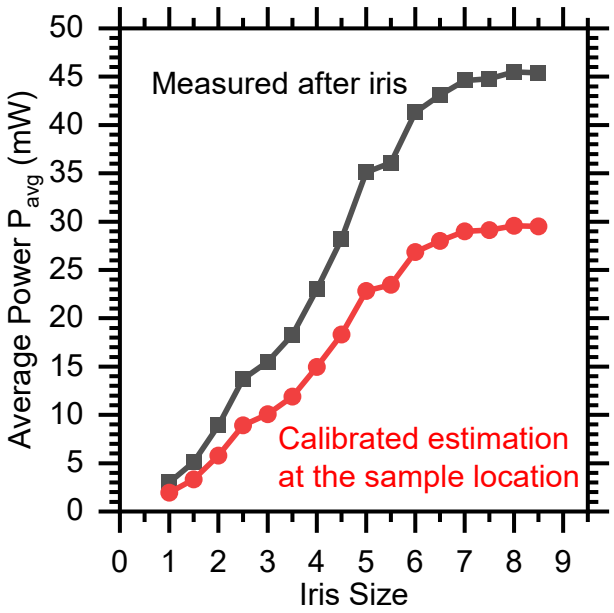

Figure 2.7. Average power of pump pulse vs iris size. The iris size is read by the numbered marks on the iris. The average power at the sample location (red circle) is estimated as 65% of that measured right after the iris (black square), according to a previous power calibration. There are 5 mirrors and 1 thin glass window between the iris and the sample cell.

Table 2.2. Properties of pump pulse vs iris size.

Scan #	Iris size[a]	Average Power (mW)[b]	Beam Diameter, Mean μ (μm)[c]	Pulse Duration (fs)[d]	Pulse Energy (μJ)[e]	Peak Intensity ($\times 10^{12}$ W/cm^2)[f]	Peak Intensity ($\times 10^{-4}$ atomic unit)[g]
2	3.5	11.9	109±1	26±1	11.9	8.15	2.32
3	4	15.0	109±1	26±1	15.0	10.3	2.93
5	4.5	18.3	109±1	26±1	18.3	12.5	3.57
4	6.5	28.0	109±1	26±1	28.0	19.2	5.47
1	full	29.5	109±1	26±1	29.5	20.2	5.76

[a] Iris size is read by the numbered marks on the iris.

[b] At the sample cell location. Estimated according to previous power calibration (Figure 2.7)

[c] Measured with DataRay beam profiler WinCamD-UHR, 4xsigma mode. Details in Figure 2.6.

[d] Measured by SD-FROG (Figure 2.8(d))

[e] Average power divided by 1 kHz repetition rate

[f] Assume Gaussian spatial profile and FROG-retrieved temporal profile (Figure 2.8)

[g] Peak intensity in W/cm^2 divided by the conversion factor from the literature[64].

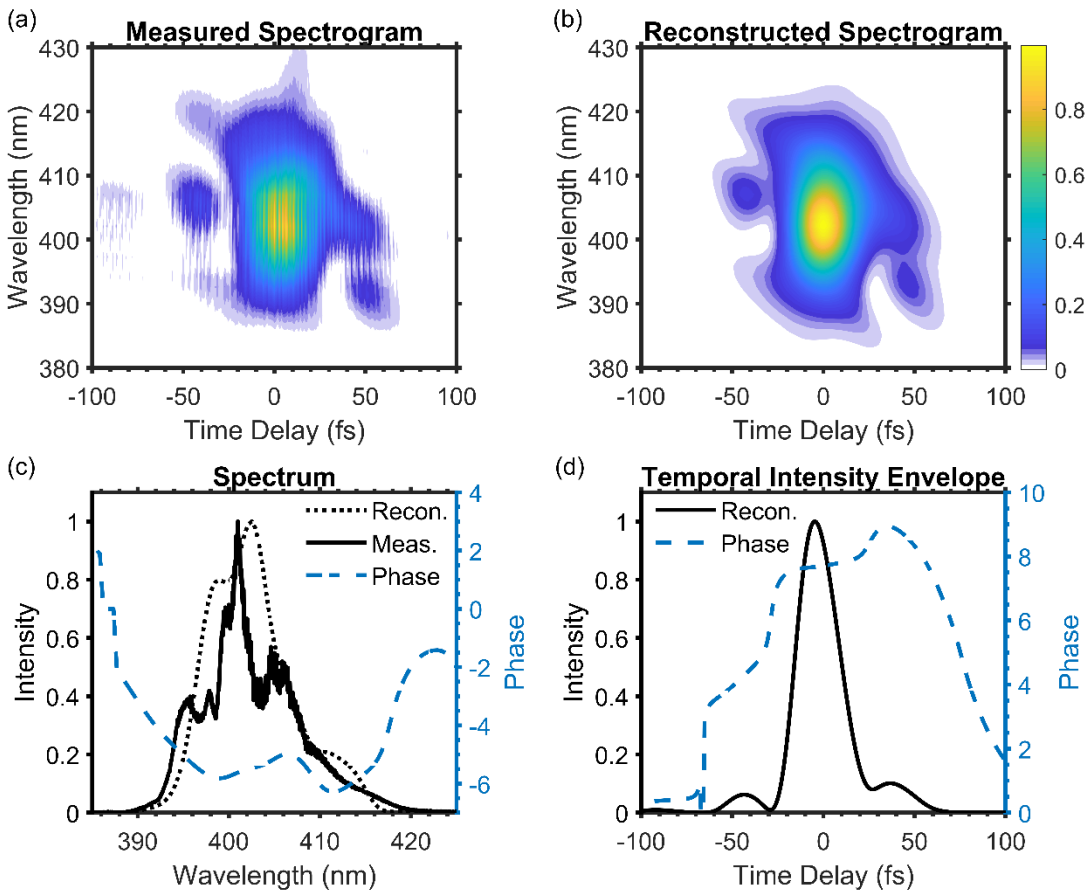

Figure 2.8. Self-Diffraction Frequency-Resolved Optical Gating (SD-FROG) measurement for 400 nm pump pulse. (a) Measured and (b) Reconstructed spectrogram. (c) Measured (black line) and reconstructed (black dash) spectrum, and reconstructed spectral phase (blue dash). The central wavelength is around 400 nm. (d) Reconstructed temporal intensity envelope (black line) and temporal phase (blue dash). The pulse duration is considered as 26±1 fs FWHM from fitting the main pulse to a Gaussian function.

2.6.2 Calibration of Time Zero and Temporal Resolution for Time-Resolved XUV Absorption Measurements

The time zero and temporal resolution (instrument response function) is calibrated with a cross-correlation measurement of pump and probe pulses in He 2s2p state.

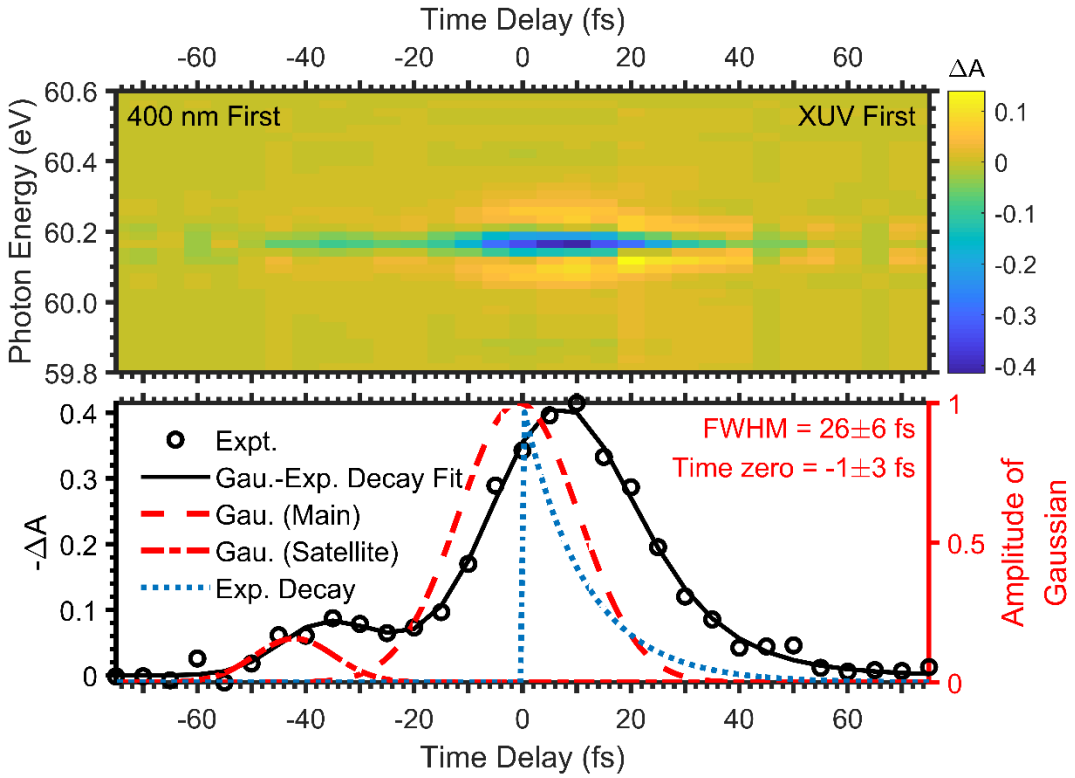

Figure 2.9. The cross-correlation measurement of pump and probe pulses in He 2s2p state. The positive time delay is when the XUV pulse arrives first before the 400 nm pulse. (a) Time-resolved XUV differential absorption (ΔA) spectrum of He 2s2p state. The XUV absorption is suppressed (ΔA turns negative) by the pump pulse when pump and probe pulses overlap. (b) Circle: Lineout of negative of measured differential absorption (-ΔA) at 60.16 eV. Black solid line: Fit by a convolution of two Gaussian (main and satellite pulses) and an exponential decay function in time delay. Red dash line: Gaussian (main pulse). The fitted FWHM and center of this Gaussian is 26±6 fs and -1±3 fs, and these are taken as the instrument response function and time zero for this work, respectively. Red dash line: Gaussian (satellite pulse).

2.6.3 Calibration of Spectral Axis

In this work, the XUV beam is dispersed by a grating onto a XUV CCD camera. As a result, the spectral axis of the raw data is recorded in camera pixels. I measure the static XUV absorption of He 2s*n*p (n = 2 to 5) states, and establish the calibration curve for converting pixel to wavelength and photon energy.

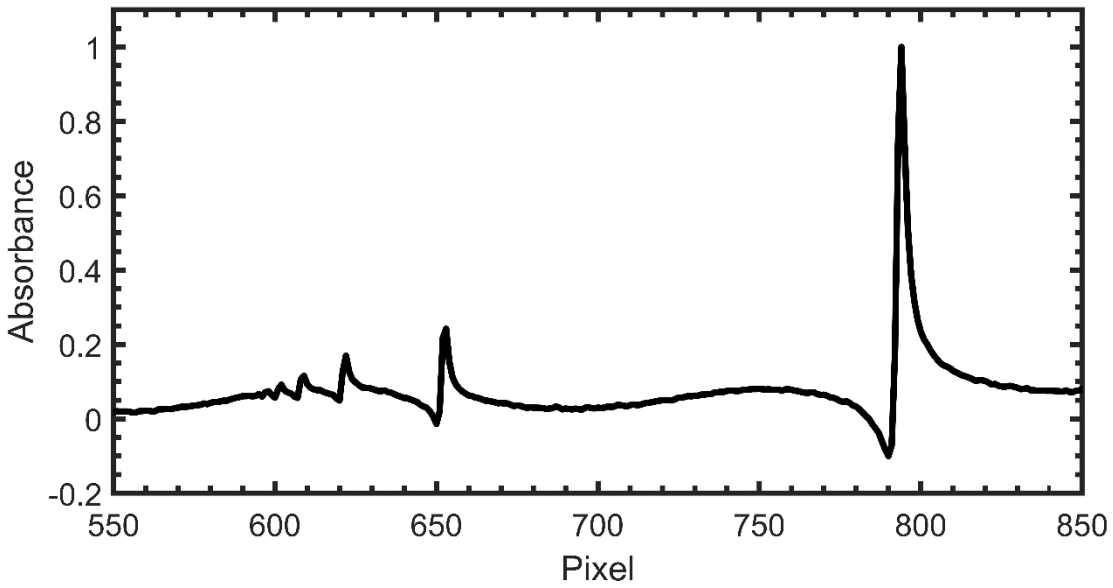

Figure 2.10. Static XUV absorption spectrum of He 2snp (n ≥ 2) excited states, as a function of XUV CCD camera pixel.

Table 2.3. Calibration Table with He 2s*n*p (n = 2 to 5) States

Electronic State	Resonance (Pixel)[a]	Location	Resonance Energy (eV), Literature[65]	Resonance Wavelength (nm)[b]
He 2s5p	608±1		64.814	19.129
He 2s4p	621.2±0.4		64.467	19.232
He 2s3p	652.2±0.2		63.658	19.476
He 2s2p	793.4±0.2		60.147	20.613

[a] Fitted to a convolution of Fano lineshape and Gaussian function, to determine the resonance location in pixel. Estimated manually for 2s5p.

[b] Converted from resonance energy (eV) in the literature.[65]

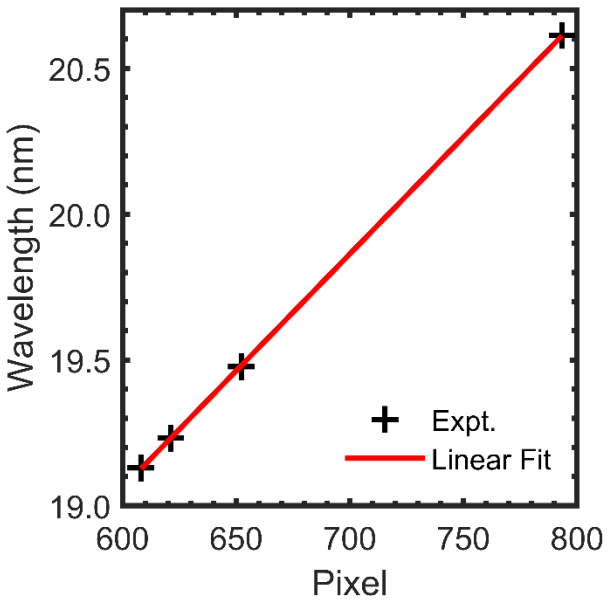

Figure 2.11. The calibration curve for wavelength vs pixel. Cross: Measured resonance location. Red line: Linear fit. This calibration curve enables the conversion from pixel to wavelength and photon energy.

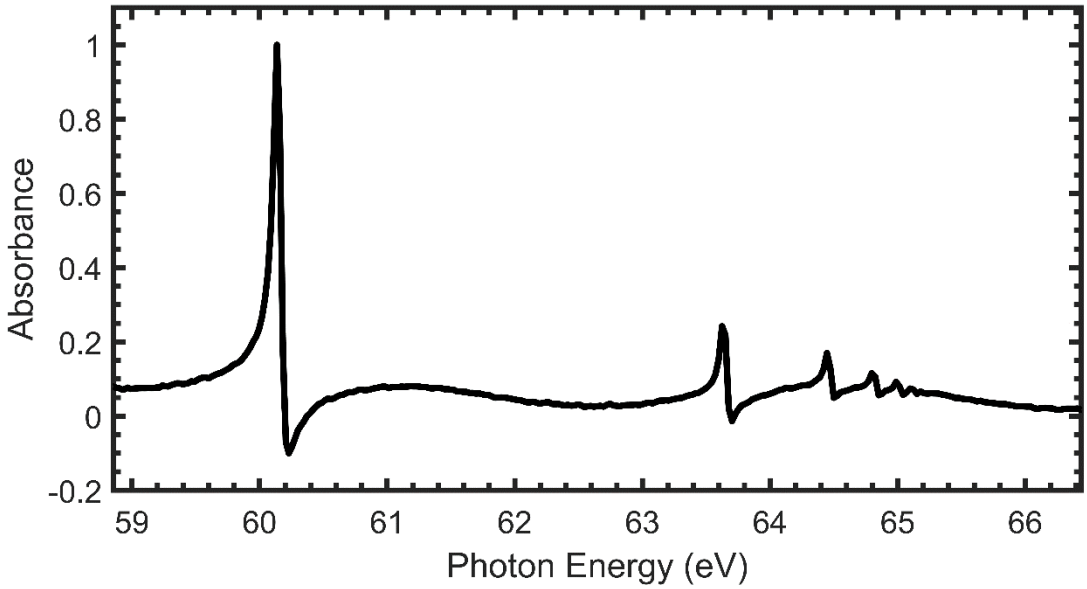

Figure 2.12. Calibrated static XUV absorption spectrum of He 2snp ($n \geq 2$) excited states, as a function of photon energy.

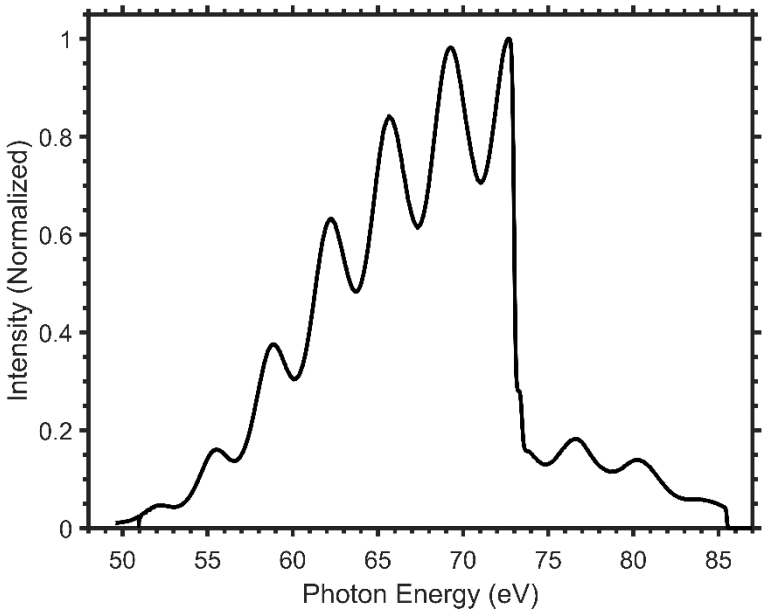

Figure 2.13. Calibrated spectrum of the XUV probe pulses after a 0.1 μm Al filter and a 0.1 μm Zr filter. The cut around 73 eV is due to the Al filter.

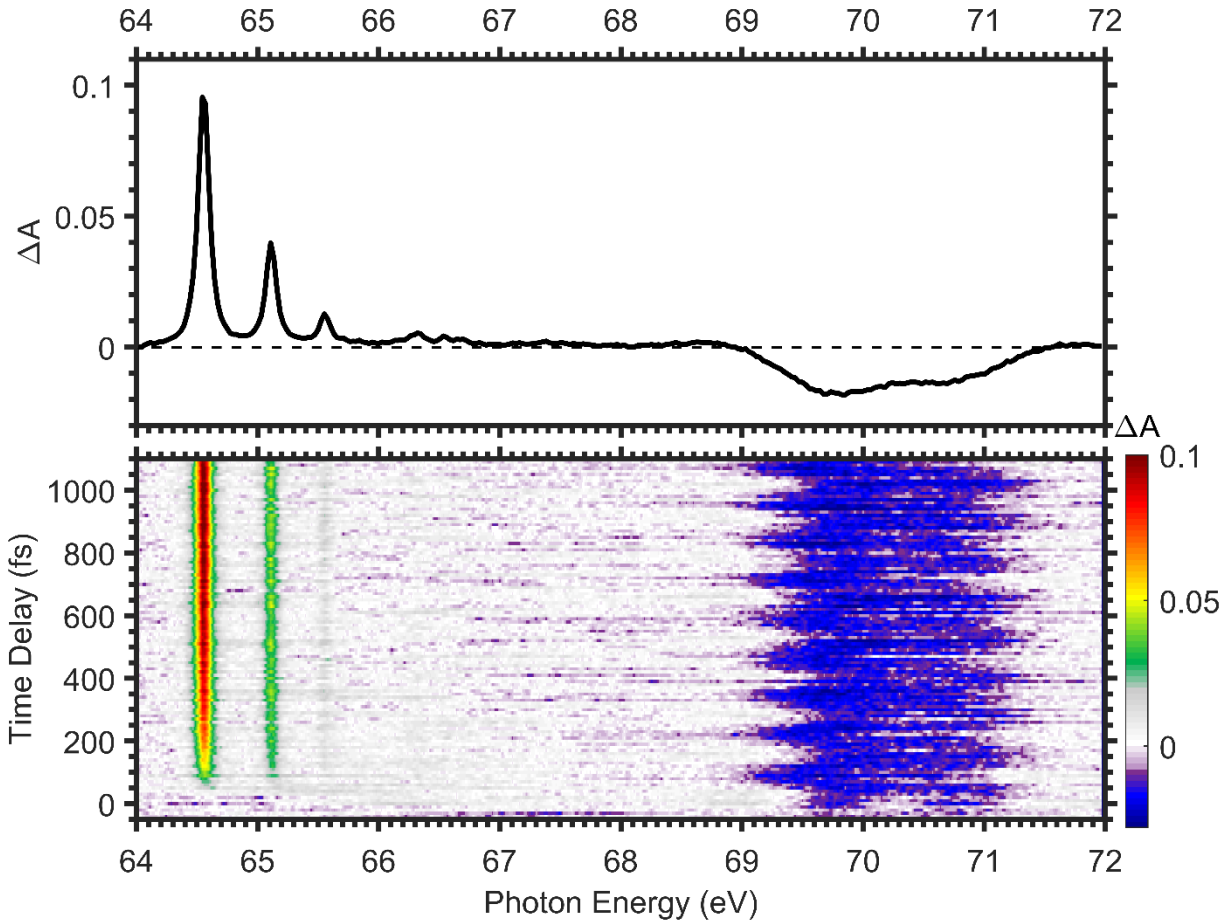

Figure 2.14. Time-resolved XUV differential absorption spectrum of CBr_4 with pump peak intensity 20.2×10^{12} W/cm^2. The positive time delay is when the 400 nm pulse arrives before the XUV pulse. The negative oscillating signals around 69 to 71 eV encode the coherent vibrational dynamics on the electronic ground state. (Upper) Differential absorption integrated from time delay of 300 to 1100 fs. Three major peaks between 64 to 66 eV correspond to dissociated atomic Br. These are likely to come from two photon absorption of the 400 nm pump pulse (photon energy 3.1 eV), because the lowest transition to valence-excited states (A bands) of CBr_4 starts at 4.9 eV (39550 cm^{-1})[66,67]

Table 2.4. Energy of dissociated atomic Br 3d absorption. The presented values agree reasonably with the literature. This also confirms the validity of the spectral axis calibration.

Transition	This work Energy (eV)	Previous Literature[68] Energy (eV)
Br $^2P_{3/2} \rightarrow {}^2D_{3/2}$	65.55	65.58
Br $^2P_{1/2} \rightarrow {}^2D_{3/2}$	65.11	65.13
Br $^2P_{3/2} \rightarrow {}^2D_{5/2}$	64.56	64.54

2.6.4 Measured Relative Slope of Br-3d Core-Excited State Potential Energy Surface (PES)

Table 2.5. Measured relative slope of $(Br\text{-}3d_{3/2,5/2})^{-1}10a_1^*$ core-excited state PES along the symmetric stretch mode. Relative slope is determined experimentally as the ratio of measured oscillation amplitude of XUV absorption energy ΔE_{XUV} (Br-$3d_{5/2}$)/ΔE_{XUV} (Br-$3d_{3/2}$).

Scan #	Peak Intensity ($\times 10^{12}$ W/cm^2)	ΔE_{XUV} (Br-$3d_{3/2}$) (meV)	ΔE_{XUV} (Br-$3d_{5/2}$) (meV)	Relative Slope
2	8.15	2.8±0.6	4.1±0.9	1.5±0.4
3	10.3	9.6±1.2	9.0±1.3	0.9±0.2
5	12.5	7.2±1.7	7.6±1.6	1.0±0.3
4	19.2	11.9±1.9	12.2±1.7	1.0±0.2
1	20.2	10.2±1.4	11.3±1.4	1.1±0.2
Mean±Error				**1.1±0.13**

2.6.5 Comment about Initial Phase of Wavepacket Trajectory

If the launching mechanism of the vibrational wavepacket is a pure non-resonant ISRS from a Gaussian pump pulse centered at t = 0, the expectation value of the wavepacket displacement will be a sine function with a zero initial phase.[22,24] Nuclear TDSE simulations reproduce this expectation by retrieving around 0.01 π initial phase of wavepacket position for all intensities, with the experimental pump pulse intensity profile measured by SD-FROG (as shown in Figure 2.8(d)).

Experimentally, the initial phase from the first experiment is around -0.1π and reasonably close to zero, as shown in the Figure 2.15 below. In the subsequent experiments, the initial phases gradually deviate toward -0.6π. This trend suggests that there may be a growing time-zero drift over the course of experiments (about four hours), and it seems to be reflected in the gradual deviation of the initial phase from zero. As a result, I do not attempt to determine the absolute initial phases from the experiments.

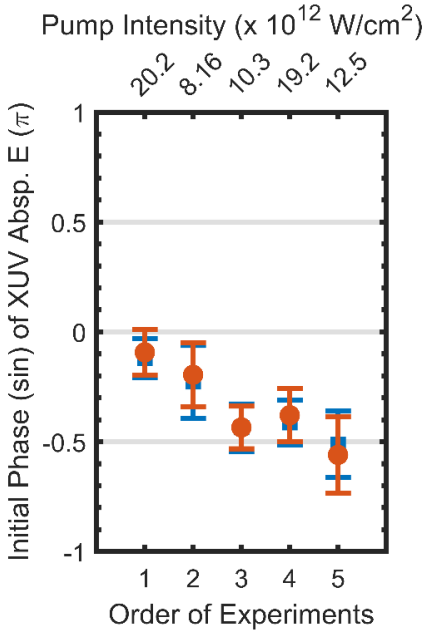

Figure 2.15. The initial phase at time zero from fitting the measured XUV absorption energy as a function of time-delay to a sine function for different pump-pulse intensities, plotted in the order of experiments.

2.6.6 Nuclear Time-Dependent Schrodinger Equation Simulations

I simulated the dynamics of the symmetric stretch mode in a manner similar to what was described in a previous work.[44] In brief, under the harmonic approximation (which is valid in the small-displacement limit), the normal modes are all independent of each other and can be treated separately. The symmetric stretching mode evolves under the influence of the Hamiltonian:

$$\hat{H}(t) = \frac{\hat{p}^2}{2\mu} + \frac{1}{2}\mu\omega_0^2\,\hat{q}^2 - \frac{1}{2}\alpha(\hat{q})|\mathcal{E}(t)|^2$$

where $\hat{p}$ is the momentum operator along this mode, $\hat{q}$ is the operator for bond stretching (relative to the equilibrium bond length), $\alpha(\hat{q})$ is the isotropic polarizability as a function of $\hat{q}$, μ is the normal mode mass, ω_0 is the normal mode frequency, and $|\mathcal{E}(t)|^2 = I(t)$ is the temporal intensity envelope of the pump pulse. Details of the above terms are as follows.

The isotropic polarizability $\alpha(\hat{q})$ tends to increase with bond stretching as the bonding electron density becomes "softer" (i.e. more diffuse) in response.[69] For small displacements, it can be approximated with $\alpha(q) = \alpha_0 + \alpha_1 q + \alpha_2 q^2$. Fitting SCAN0/decontracted aug-cc-pVTZ polarizabilities across 201 uniformly spaced bond stretches spanning ±0.1 Å relative to equilibrium for CBr_4 yields $\alpha_0 = 97.76, \alpha_1 = 38.70, \alpha_2 = 16.90$, in atomic units. The normal mode mass μ = 575437.04 atomic units (i. e. 4 times the mass of a single ^{79}Br atom, assuming all four Br atoms in the molecule correspond to this isotope). The normal mode frequency is 0.00129 atomic units (282.32 cm^{-1}) from the ground state DFT calculations.

The temporal intensity envelope of the pump pulse $|\mathcal{E}(t)|^2 = I(t)$ is calculated as

$$I(t) = I_{\text{pk}}(\text{a.u.}) I_{\text{FROG}}(t) \cos^2(\omega t)$$

where I_{pk} (a.u.) is the calibrated peak intensity in atomic units (Table 2.2), $I_{\text{FROG}}(t)$ is the normalized temporal intensity envelope from SD-FROG measurement (Figure 2.8(d)), ω is the angular frequency of 400 nm pump pulse and equals 0.1139 atomic units.

With these parameters, the time-dependent Schrödinger equation (TDSE) for the symmetric stretching mode was numerically simulated within the interaction picture for each of the experimentally studied pump laser intensities, taking the field-free harmonic oscillator terms as the reference Hamiltonian and the $-\frac{1}{2}\alpha(\hat{q})|\mathcal{E}(t)|^2$ term as the perturbation. The simulations were done in the basis of the ten lowest energy eigenstates of the unperturbed harmonic oscillator Hamiltonian. The wavefunction at t = −4134.14 atomic units (100 fs) was assumed to be the ground state of the unperturbed harmonic oscillator, and the wave-function was subsequently propagated in time to t = 41339.86 atomic units (1000 fs) with step sizes of 2 atomic units (0.048 fs).

2.6.7 Comment about Polarizability Calculations

The TDSE simulations along the symmetric stretch mode appear to predict bond stretches that are roughly three times as great for a given pump power intensity as those estimated from the experimental ΔE_{XUV} values and the computed Br core-excited PES slope of -9.4 eV/Å. A potential source of this discrepancy might be the use of *too large* polarizabilities for the TDSE simulations, as more simplified previous models[24] have indicated that the bond stretch amplitude is directly proportional to α_1 (i.e. the slope of the polarizability vs bond stretch at the equilibrium geometry).

Such an overestimation could potentially arise from either errors in the finite difference approximation used for computing polarizabilities or errors intrinsic to the SCAN0/decontracted aug-cc-pVTZ model chemistry. Both scenarios appear to be unlikely, as discussed below.

2.6.7.1 Finite difference

Q-Chem presently lacks analytic polarizabilities with the X2C relativistic method. As a result, the polarizability was computed via finite differences of the energy with different electric fields. As the polarizability is the negative of the second derivative of the energy vs applied field strength, I can utilize standard finite difference formulae and obtain:

$$\alpha_{zz} = -\left(\frac{d^2}{d\mathcal{E}_z^2} E(\mathcal{E}_z)\right)_{\mathcal{E}_z=0} = \frac{30E(0) - 16E(h) - 16E(-h) + E(2h) + E(-2h)}{12h^2} + O(h^4)$$

where $E(\mathcal{E}_z)$ is the energy of the system computed with an applied field $\mathcal{E}_z$ along the z direction and $h = 0.005$ atomic units is the applied electric field strength for the finite difference calculations. As CBr_4 is tetrahedral, the isotropic polarizability $\alpha = \alpha_{zz}$. Furthermore, the lack of a permanent dipole moment ensures $E(h) = E(-h)$. So the previous five-point stencil simplifies to the following three point formula:

$$\alpha_{zz} = -\left(\frac{d^2}{d\mathcal{E}_z^2}E(\mathcal{E}_z)\right)_{\mathcal{E}_z=0} = \frac{15E(0) - 16E(h) + E(2h)}{6h^2} + O(h^4)$$

As a result, for any given bond stretch, the energies are computed for zero external fields, and with fields of 0.005 a.u. and 0.01 a.u. along the z direction ($E(0), E(h)$ and $E(2h)$, respectively) to compute the polarizability. The scale of the finite difference error can be estimated by comparing the finite difference results in the nonrelativistic (i.e. X2C free) SCAN0/decontracted aug-cc-pVTZ case, for which analytic values can be computed. The resulting values for the 201 uniformly spaced bond stretches spanning ±0.1 Å relative to the equilibrium geometry that were used to fit the quadratic polynomial $\alpha(q) = \alpha_0 + \alpha_1 q + \alpha_2 q^2$ indicate very little finite difference error. Specifically, the largest deviation between analytic and finite difference nonrelativistic SCAN0/decontracted aug-cc-pVTZ isotropic polarizabilities is 0.0008 atomic units for the geometries utilized and fits from the two approaches predict identical α_1 values of 38.18 atomic units. Finite difference errors in the X2C SCAN0/decontracted aug-cc-pVTZ isotropic polarizabilities therefore appear to be not a major concern. I also take the opportunity to note that relativistic effects appear to slightly increase the isotropic polarizability in this molecule. All the computed polarizability values are provided in the accompanying Excel spreadsheet.

2.6.7.2 Electronic Structure

The other potential source for errors in the polarizability may be inadequacies of the SCAN0/decontracted aug-cc-pVTZ model chemistry, even though it has been shown to be accurate for lighter elements[70]. I therefore carried out nonrelativistic CCSD(T)/aug-cc-pVTZ calculations (utilizing the aforementioned finite difference formula) for a few bond stretches to determine if SCAN0/decontracted aug-cc-pVTZ was acceptable. Using 41 equally spaced geometries between 1.9046-1.9446 Å (same as those used in the main text for finding the Br core-excited PES slope from ROKS), I find that nonrelativistic CCSD(T)/aug-cc-pVTZ yields very similar polarizabilities (albeit slightly smaller by 0.1-0.2 atomic units) as nonrelativistic SCAN0/decontracted aug-cc-pVTZ. The fitted α_1 values in this interval are: 38.02 atomic units from SCAN0/decontracted aug-cc-pVTZ and 36.64 atomic units from CCSD(T)/aug-cc-pVTZ. However, the CCSD(T) calculations utilize a frozen core (C 1s, Br 1s 2s 2p) and the decontracted aug-cc-pVTZ basis used in the SCAN0 calculations is more flexible (and hence likely to lead to larger polarizabilities) than the aug-cc-pVTZ basis used for the CCSD(T) calculations. It nonetheless appears clear that the polarizabilities obtained from finite differences on SCAN0/decontracted aug-cc-pVTZ with X2C are quite reasonable, and lead to α_1 within 5% of CCSD(T). The polarizability fits are therefore extremely unlikely to contribute to the factor of 3 difference between the bond stretching amplitude predicted by TDSE simulations and experiment.

3 Dissociation Dynamics of Br_2 C $^1\Pi_u$ 1_u State

The material in this chapter has been published and is reprinted with permission from

Beetar, J.E.†; Ou, J.-H.†; Kobayashi, Y. and Leone, S. R*.
"Different Rise Times of Atomic Br $M_{4,5}$ $3d_{3/2,5/2}$ Core Level Absorptions during Br_2 C $^1\Pi_u$ 1_u State Dissociation via Extreme Ultraviolet Transient Absorption Spectroscopy."
Journal of Physical Chemistry A, **2025,** in press. (https://doi.org/10.1021/acs.jpca.5c06776)

†These two authors contributed equally. *Correspondence author

3.1 Introduction

Dissociation is a fundamental chemical reaction. While dissociation is simple to perceive as a phenomenon, there is not a once-and-for-all definition for dissociation time. In fact, Zewail and colleagues[7] pointed out that "dissociation time" could have more than one definition, when they studied the dissociation of ICN.

A good example of the subtlety of "dissociation times" is the dissociation of the Br_2 C $^1\Pi_u$ 1_u state into two ground state Br atoms (Nomenclature of Br_2 electronic states follows the literature). It is triggered by absorption of 400 nm light from the electronic ground state (X $^1\Sigma_g^+$) of Br_2 as

$$Br_2\,(X\,^1\Sigma_g^+) + 400\text{ nm light} \rightarrow Br_2\,(C\,^1\Pi_u\,1_u) \rightarrow Br\,(^2P_{3/2}) + Br\,(^2P_{3/2}).$$

Over the past twenty years, this dissociation has been extensively studied by numerous time-resolved measurements.[71–78] Surprisingly, these measurements[71–78] report widely different dissociation times from 30 to 340 fs dependent on the various detection methods (Table 3.1).

In general, those detection methods measure two categories of detection, particles (photoelectrons[71–74,79] or photoions[76–78]) or light (emission[75,76]). With the detection of particles, time-resolved photoelectron spectroscopy (TRPES)[71–74,79] showed that the atomic signals appear around 40 fs[71–73] to 85 fs[74,79] after excitation. On the other hand, cold target recoil ion momentum spectroscopy (COLTRIMS)[77] found that the molecular signals persist up to 140 ± 15 fs. In addition, Coulomb explosion imaging (CEI)[78] recorded the rise time as 200 fs for Br^+ ions (probed by a 800 nm pulse) and 340 fs for Br_2^+ ions (probed by a 90.6 eV pulse). With the detection of light emission, high harmonic spectroscopy (interferometry)[75,76] showed that the amplitude of emitted high harmonics converges to an asymptotic value around 300 fs, when the atomic character is considered to be fully established. Such differences in the dissociation time are intriguing, especially when the reactant Br_2 is a simple diatomic molecule.

In this work, attosecond XUV transient absorption spectroscopy[14,15,17,18] is used to track the

dissociation of Br_2 in the $C\,^1\Pi_u\ 1_u$ state by core level absorptions. Specifically, the XUV absorption spectrum covers both the Br 3d core-to-valence and core-to-Rydberg absorptions at the same time. During the dissociation, the XUV absorption energy shifts because the energy gap between the $C\,^1\Pi_u\ 1_u$ and Br 3d core-excited states changes. By following the XUV absorption spectrum as it evolves from the molecular to the atomic limit, the underlying change in the electronic structure from Br_2 molecules to Br atoms is mapped out. I consider the dissociation to be completed based on spectroscopic identification[7] when the XUV absorption spectrum converges to that of the Br atoms, within the temporal and spectral resolution of the experiment.

Previously, the static Br 3d core-to-valence and core-to-Rydberg spectra were measured for either Br_2 molecules or Br atoms separately[25,68,80–84] (Table 3.3). The broadband time-resolved spectra connect these studies scattered throughout the literature with a full evolution from molecules to atoms. This unification demonstrates the unique strength of time-resolved absorption spectroscopy with broadband XUV light.

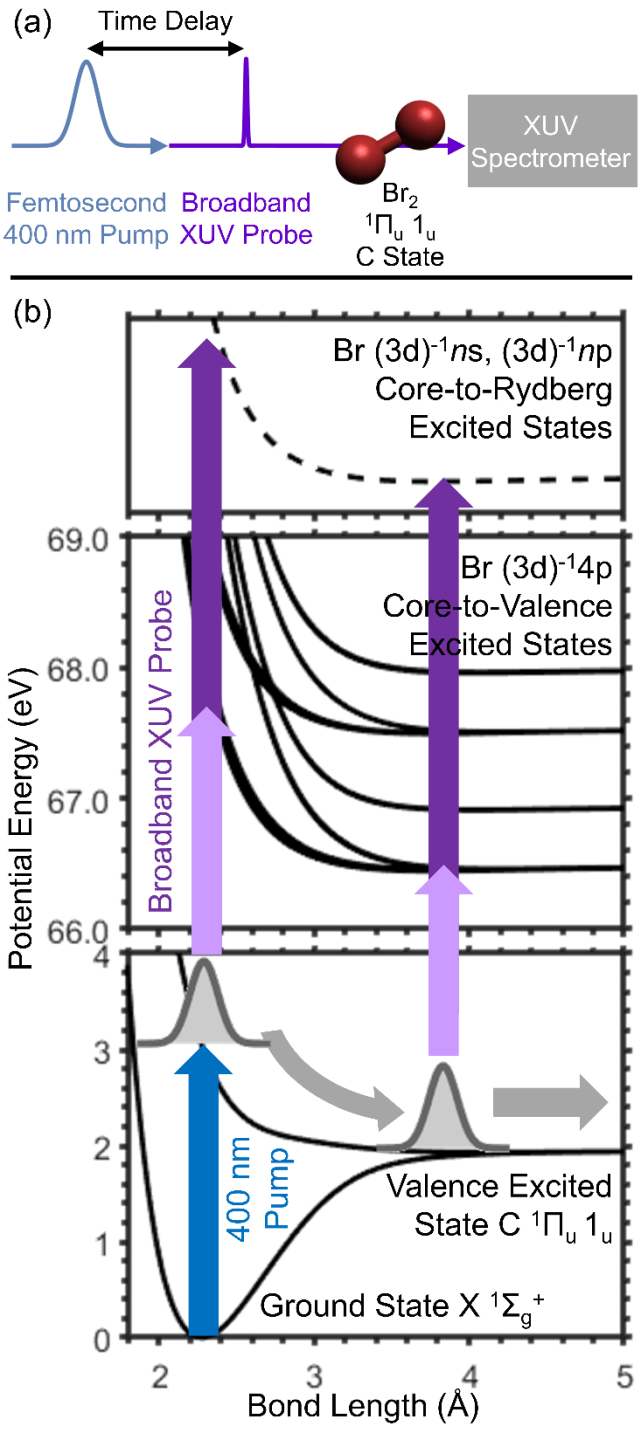

Figure 3.1. Experimental scheme. (a) Attosecond extreme ultraviolet (XUV) transient absorption spectroscopy on the dissociation of Br_2 molecules in the C $^1\Pi_u$ 1_u state. The dissociation is launched by femtosecond 400 nm pump pulses and monitored by the time-resolved absorption of broadband XUV probe pulses at the Br $M_{4,5}$ $3d_{3/2,5/2}$ edges (66 to 80 eV). (b) Femtosecond 400 nm pump pulses bring the Br_2 molecule from the electronic ground X $^1\Sigma_g^+$ state to the excited C $^1\Pi_u$ 1_u state, to initiate the dissociation. As the nuclear wavepacket travels on the C state, it is probed by the absorptions of XUV

pulses to the Br core-to-valence $(3d)^{-1}4p$ and core-to-Rydberg $(3d)^{-1}ns$ and $(3d)^{-1}np$ ($n \geq 5$) excited states. Solid lines: Calculated potential energy curves (PEC) of the ground X, C and core-to-valence $(3d)^{-1}4p$ excited states. Dashed lines: Hypothetical PEC of core-to-Rydberg excited state for illustration purposes.

Table 3.1. Experimental time-resolved studies on the dissociation of Br_2 C $^1\Pi_u$ 1_u state[a]

Timescale Reported (fs)	Temporal Resolution (fs)	Pump Pulse	Probe Pulse	Reference
Object of Detection: Experimental Technique				
Particle (photoelectron): Time-resolved photoelectron spectroscopy (TRPES)				
40 ± 14 (Br^+ $^3P_{2,1,0}$)	300±14	400 nm, 80 fs	H17, 47 nm (26.4 eV), 290 fs	Nugent-Glandorf 2001 ([71])
45 ± 8 (Br^+ $^3P_{2,1,0}$)	340±16	402.5 nm	H17, 47 nm (26.4 eV), 250 fs	Nugent-Glandorf 2002 ([72])
30 ± 19 (Br^+ $^3P_{2,1,0}$)	203±17	402.5 nm	H19, 42 nm (29.45 eV), 190 fs	Nugent-Glandorf 2002 ([72])
40 (Br^+ $^3P_{2,1,0}$)	230	402.5 nm, < 10^{12} W/cm^2	H15, 53.7 nm, (23.1 eV)	Strasser 2007 ([73])
85 ± 15 (Br^+ $^3P_{2,1,0}$)	135±5	395 nm, 60 fs, < 10^{12} W/cm^2	H15, 23.5 eV, 120 fs	Wernet 2009 ([74])
Particle (photoion): Cold target recoil ion momentum spectroscopy (COLTRIMS)				
140 ± 15 (Br^+)		400 nm, 40 fs, 2×10^{11} W/cm^2	800 nm, 30 fs, 4×10^{13} W/cm^2	Li 2010 ([77])
Particle (photoion): Coulomb explosion imaging (CEI)				
200 (Br^+)		400 nm, 100 fs, 1×10^{12} W/cm^2	800 nm, 100 fs, 5×10^{13} W/cm^2	Rouzée 2013 ([78])
340 (Br_2^+)	300		15.7 nm (90.6 eV), 50 fs, 10^{13} W/cm^2	Rouzée 2013 ([78])
Particle (photoion) and light (emission): High harmonic spectroscopy				
300	50 to 60 (H18)	400 nm, 5×10^{11} W/cm^2	800 nm, 1.5×10^{14} W/cm^2	Wörner 2010 ([76])

Light (emission): High harmonic transient grating spectroscopy				
300	50 (H20)	400 nm, 10^{12} W/cm^2	800 nm, 10^{14} W/cm^2	Wörner 2010 ([75])
Light (absorption): XUV transient absorption spectroscopy				
38 ± 1	26 ± 3	400 nm, 26 ± 1 fs, 5×10^{12} W/cm^2	50-80 eV broadband	Present work
Br 3d ($^2P_{3/2}$) → 4p ($^2D_{5/2}$)				
20 ± 5				
Br 3d ($^2P_{3/2}$) → 4p ($^2D_{3/2}$)				

[a]H# means the #-th harmonic of the 800 nm fundamental light.

Table 3.2. Measurements of Br core-to-valence (3d → 4p) and core-to-Rydberg (3d → *n*s, *n*p, *n* ≥ 5) spectra of ground state Br_2 molecules and Br atoms in the literature.[25,68,80–84]

	Transition	
System	Core-to-valence 3d → 4p (67-70 eV)	Core-to-Rydberg 3d → *n*s, *n*p, *n* ≥ 5 (73-80 eV)
Br_2 molecule	EELS[80] XUV-TAS[25]	XAS[84]
Br atom	EELS[80] PES[68] XAS[81,83] XUV-TAS[25]	PES[82] XAS[83]

EELS: Electron impact Energy Loss Spectroscopy

PES: Photoelectron Spectroscopy

XAS: XUV/X-ray Absorption Spectroscopy (static)

XUV-TAS: XUV Transient Absorption Spectroscopy (time-resolved)

3.2 Methods

The experimental and computational methods are described briefly here with details in the Appendix.

3.2.1 Experiments

The laser source is a Coherent Astrella USP (800 nm, 35 fs FWHM, 7 mJ, 1 kHz). The pump pulses (400 nm, 26 ± 1 fs FWHM) come from second harmonic generation (SHG) of 70% of the Astrella output (4.9 mJ) in a β-barium borate (BBO) crystal, the 400 nm light is focused through a neon-filled (1.7 bar) tube (1.37 m long), and the output is then compressed by 8 chirped mirrors. The XUV probe pulses (50-85 eV photon energy) come from high harmonic generation (HHG) in a neon gas cell with 800 nm driving field pulses. The driving field pulses are produced by taking 30% of the Astrella output (2.1 mJ), focusing it into a neon-filled (20 psi) stretched hollow core fiber (HCF) (1.5 m long, 400 μm inner diameter), and then temporally compressing the output by 16 chirped mirrors and a piece of 2 mm thick ADP crystal. The driving field is then removed by a 0.1 μm thick Al filter. At the sample cell, pump and probe beams recombine non-collinearly and interact with Br_2 vapor. After a 0.1 μm thick Zr filter, the XUV beam is detected by a homebuilt spectrograph. The time-resolved (transient) differential absorption $\Delta A(\omega, t)$ is calculated from the XUV absorption spectrum of Br_2 with and without pump pulses.

3.2.2 Computations

Potential energy curves (PECs) and transition dipole moments (TDMs) for valence and 3d-to-4p core-to-valence excited states are calculated with a developer version of GAMESS.[85] The nuclear wavepacket trajectory on the PEC of the C state is numerically solved from the nuclear time-dependent Schrödinger equation (TDSE) where the transition due to the pump pulse is explicitly considered. The time-resolved (transient) XUV absorption cross section[86] from the C state to core-to-valence excited states are calculated from the TDMs and wavepacket trajectory.

3.3 Results and Discussion: Overview of both the Core-to-Valence and Core-to-Rydberg Absorption Spectrum

In this study, a 400 nm pump pulse excites Br_2 from the electronic ground state ($X\ ^1\Sigma_g^+$) to the excited $C\ ^1\Pi_u\ 1_u$ state, which causes the dissociation into two Br atoms in the electronic ground state ($^2P_{3/2}$).

$$Br_2\ (^1\Sigma_g^+ X) + 400\ \text{nm light} \rightarrow Br_2\ (C\ ^1\Pi_u\ 1_u) \rightarrow Br\ (^2P_{3/2}) + Br\ (^2P_{3/2})$$

The above processes are monitored with XUV probe pulses via changes in the absorption spectrum from the molecular to atomic limit over time. Furthermore, due to the broad bandwidth of the XUV probe pulse, not only core-to-valence but also core-to-Rydberg absorptions are measured. Both absorptions will be overviewed in this section, then elaborated for core-to-valence absorptions in Section 3.4, then core-to-Rydberg absorptions in Section 3.5.

3.3.1 Before Dissociation: Identification of Br_2 Molecules with Static Core-to-Valence and Core-to-Rydberg Absorption Spectrum

Before the pump pulse, the Br_2 molecules in the electronic ground state are identified with its XUV absorption spectrum (Figure 3.2 and Table 3.3). Both core-to-valence (3d → 4p, 67 to 70 eV) and core-to-Rydberg (3d → *n*s, *n*p ($n \geq 5$), 73 to 79 eV) transitions are observed together. For core-to-valence absorptions (Figure 3.2(a)), the $3d_{5/2,3/2} \rightarrow 4p\sigma^*$ spin-orbit doublet is at 68.10 and 69.13 eV. The spin-orbit splitting is 1.03 eV. For core-to-Rydberg absorptions (Figure 3.2(b)), a series of 3d → *n*s, *n*p ($n \geq 5$) absorption peaks are observed. The presented results agree with the literature using electron impact energy loss spectroscopy[80] and photoelectron spectroscopy[84].

A clear XUV absorption spectrum of Br_2 molecules marks the starting point for the study of dissociation. As the dissociation is launched by the pump pulse, the absorption from Br_2 molecules decreases and is observed as ground state bleaching signals in the time-resolved XUV absorption spectrum in the next section.

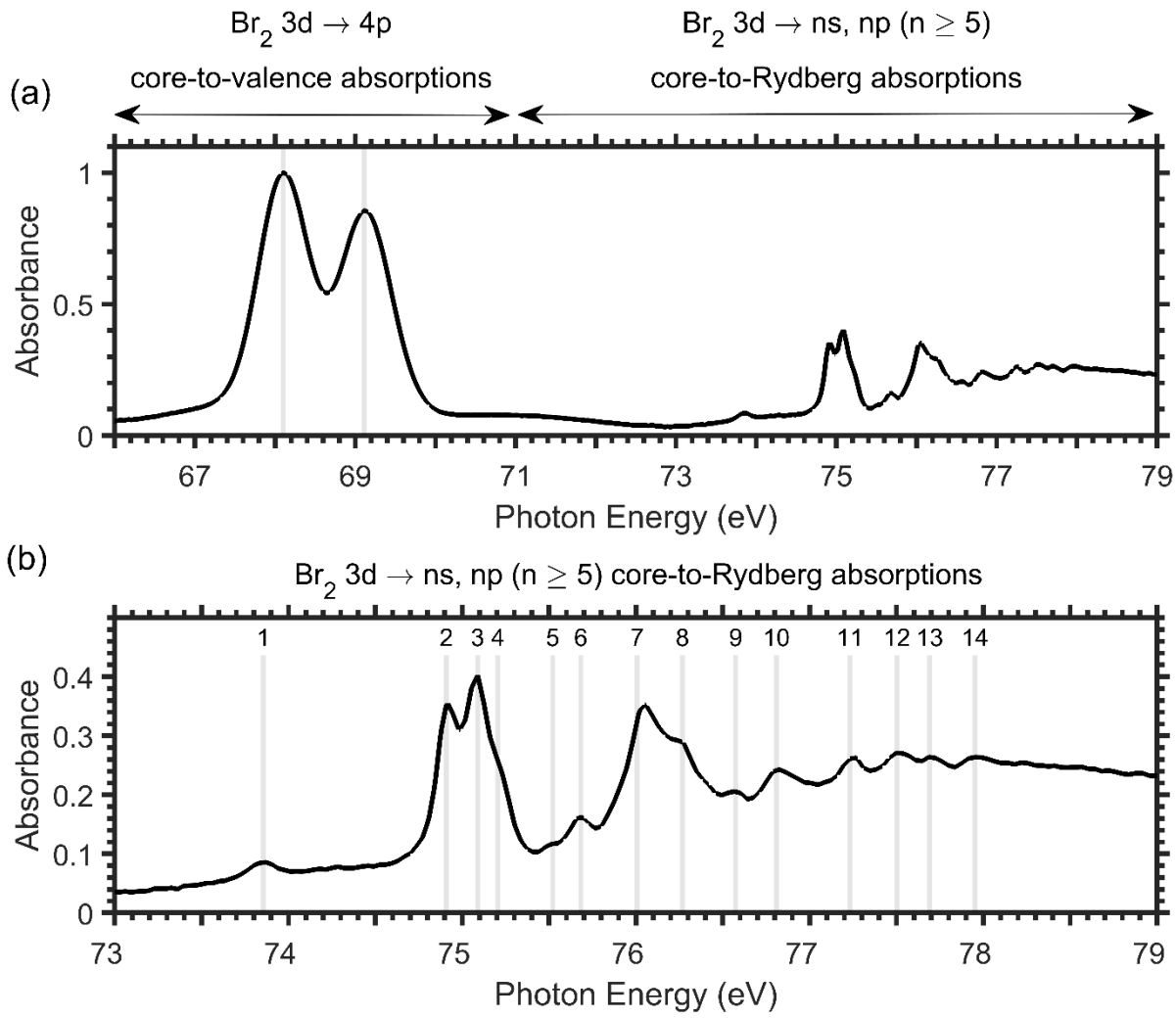

Figure 3.2. Static XUV absorption spectrum of Br_2 molecules at Br 3d M edge (a) 3d → 4p core-to-valence and 3d → *n*s, *n*p (*n* ≥ 5) core-to-Rydberg absorptions. (b) 3d → *n*s, *n*p (*n* ≥ 5) core-to-Rydberg absorptions. Assignments in Table 3.3.

Table 3.3. Br core-to-valence (3d → 4p) and core-to-Rydberg (3d → *n*s, *n*p ($n \geq 5$)) absorptions from Br_2 molecules in the electronic ground state. The corresponding spectrum is in Figure 3.2. Nomenclature of the core-to-Rydberg absorptions follows Ref. [84].

Peak	Electronic Transitions	E (eV) This work[a]	E (eV) Ref. [80,b]	E (eV) Ref. [25,a]	E (eV) Ref. [84,c]
	core-to-valence				
	$3d_{5/2} \rightarrow 4p\sigma^*$	68.10	68.189	68.3	
	$3d_{3/2} \rightarrow 4p\sigma^*$	69.11	69.209	69.4	
	core-to-Rydberg				
1	3d → 5s	73.85			
2	$3d_{\delta 5/2} \rightarrow 5p$	74.91	74.890		74.946
3	$3d_{\pi 3/2} \rightarrow 5p$	75.09	75.047		75.112
4	$3d_{\sigma 1/2} \rightarrow 5p$	75.21			75.238
5	$3d_{\delta 5/2} \rightarrow 6s$	75.52			75.518
6	$3d_{\pi 3/2} \rightarrow 6s$	75.68			75.672
7	$3d_{\delta 3/2} \rightarrow 5p$	76.01	75.962		76.007
8	$3d_{\pi 3/2} \rightarrow 6p$	76.27			76.272
9	$3d_{\delta 5/2} \rightarrow 7p$	76.57			76.555
10	$3d_{\pi 1/2} \rightarrow 6s$	76.81			76.771
11	$3d_{\delta 3/2} \rightarrow 6p$	77.23			77.178
12	$3d_{\pi 1/2} \rightarrow 6p$	77.50			77.419
13	$3d_{\delta 3/2} \rightarrow 7p$	77.69			77.613
14	$3d_{\pi 1/2} \rightarrow 7p$	77.95			77.809

[a] XUV absorption spectroscopy

[b] Electron impact energy loss spectroscopy.[80] Energy resolution (FWHM) is 75 meV.

[c] Photoelectron spectroscopy.[84] Photon resolution is 50 meV at 90 eV photon energy.

3.3.2 During Dissociation: Overview of the Changes in Time-Resolved Core-to-Valence and Core-to-Rydberg Absorption Spectrum

The dissociation is monitored by the changes in the time-resolved XUV absorption spectrum. Figure 3.3(b) shows the time-resolved XUV differential absorption ΔA(t) spectrum as a function of the time delay between the 400 nm pump and XUV probe pulses. Positive time delays mean the 400 nm pump arrives before the XUV probe pulse. The differential absorption ΔA(t) signals represent the change in XUV absorption after the pump pulse. Positive and negative ΔA(t) signals correspond to new or increased absorptions and decreased absorptions, respectively. I will analyze the core-to-valence absorptions first in Section 3.4, then core-to-Rydberg absorptions in Section 3.5.

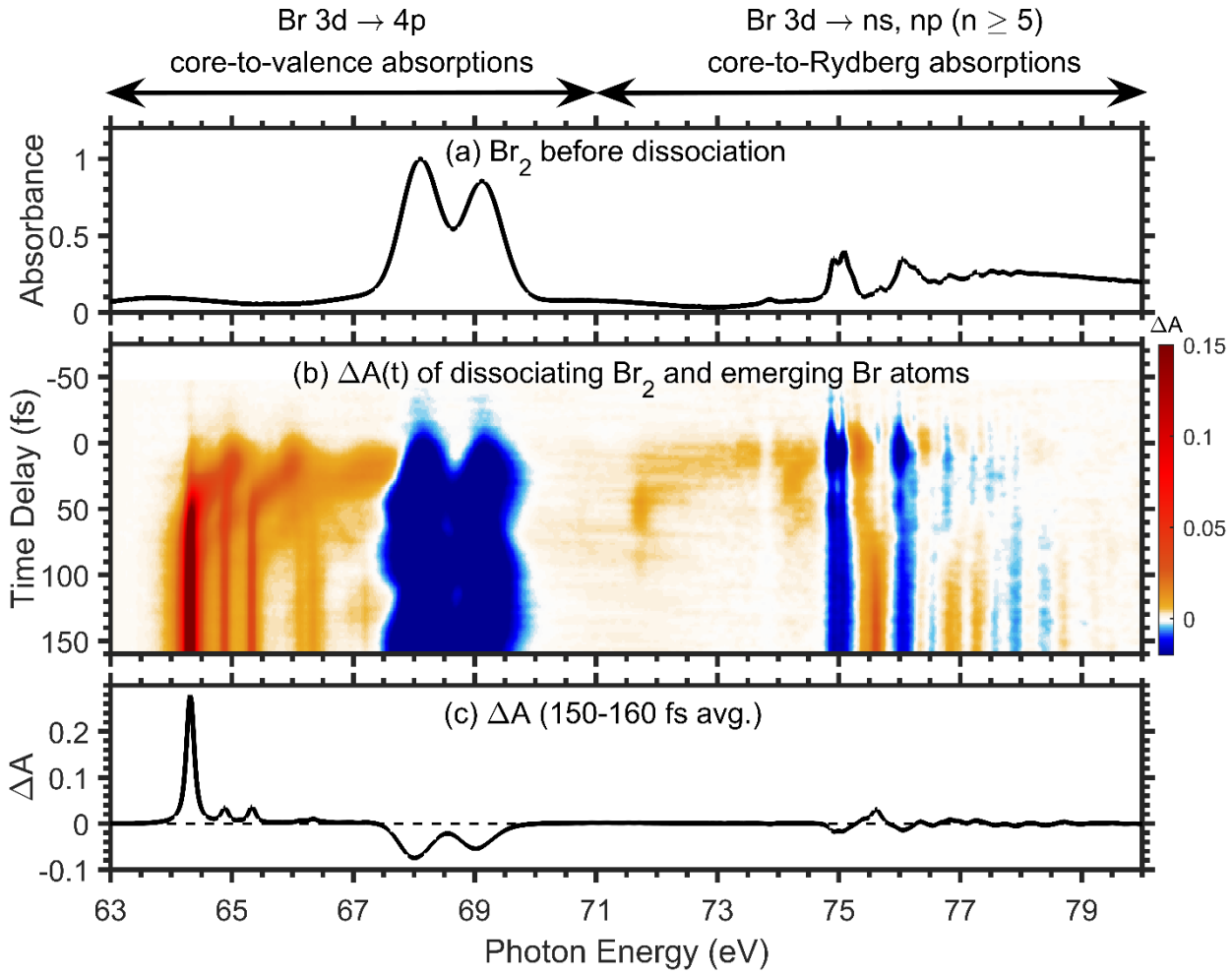

Figure 3.3. Measured time-resolved XUV core-to-valence (67-70 eV) and core-to-Rydberg (73-80 eV) absorption spectrum during the dissociation of the Br_2 C $^1\Pi_u$ 1_u state. (a) Static XUV absorption spectrum of the Br_2 molecules before dissociation. (b) Time-resolved XUV differential absorption spectrum ΔA(t) of the dissociating Br_2 molecule and resulting Br atoms, as a function of the time delay between the 400 nm pump and XUV probe pulses. Positive time delays mean the 400 nm pump pulse

arrives before the XUV probe pulse. (c) Time average from 150 to 160 fs of the differential absorption signals ΔA(t) in (b). New absorptions from dissociated Br atoms lead to positive ΔA, and decreased absorptions from Br_2 molecules cause negative ΔA. Specifically, the Br_2 C state dissociates into two ground state Br atoms, which are probed by the atomic 3d $^2P_{3/2} \rightarrow$ 4p $^2D_{5/2, 3/2}$ absorptions at 64.31 and 65.34 eV, respectively. The other atomic 3d $^2P_{1/2} \rightarrow$ 4p $^2D_{3/2}$ absorption is also observed at 64.89 eV, but this signal originates from another excited state of Br_2 molecules (Appendix). Above 73 eV, ground state bleaching of Br_2 core-to-Rydberg absorptions overlap with the appearance of atomic Br core-to-Rydberg absorptions.

3.4 During Dissociation: Changes in Time-Resolved Br Core-to-Valence Absorption Spectrum

The terminology here on differential absorption signals follows the literature.[87] During the dissociation, several phenomena occur such as *ground state bleaching* of absorptions from Br_2 molecule, *excited state absorptions* from the Br_2 molecule pumped to the excited C $^1\Pi_u$ 1_u state, and *product absorptions* from the dissociating Br atoms, which are explained in the following subsections.

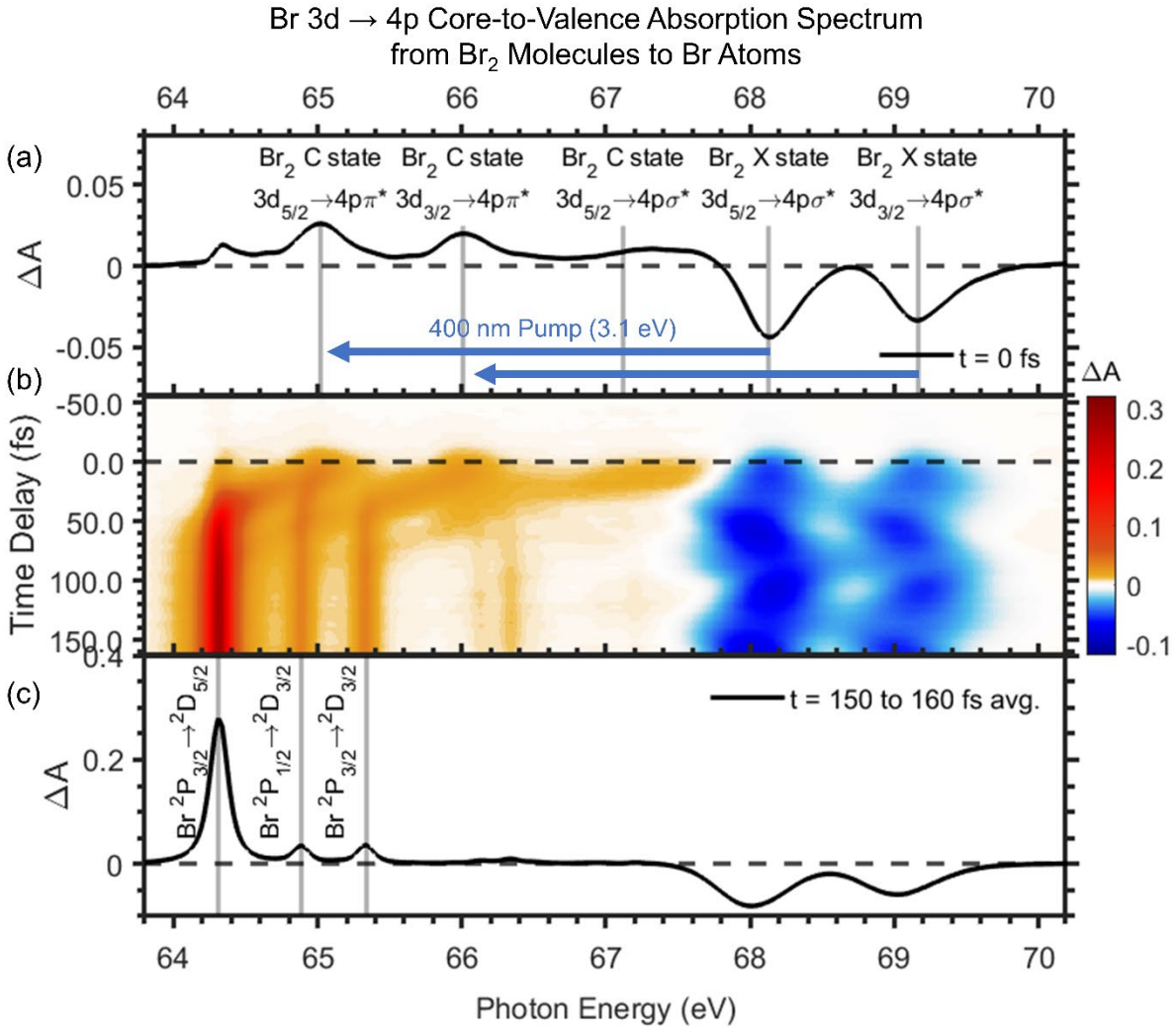

Figure 3.4. Measured time-resolved XUV core-to-valence absorption spectrum during the dissociation of the Br_2 C $^1\Pi_u$ 1_u state. (a) The differential absorption spectrum at time zero ΔA(t = 0). The negative signals around 67.5-69.5 eV are the ground state bleaching of the $3d_{5/2,3/2} \rightarrow 4p\sigma^*$ doublet of Br_2 molecules. (b) Time-resolved differential absorption spectrum ΔA(t) of the dissociating Br_2 molecule and resulting Br atoms, as a function of the time delay between the 400 nm pump and XUV probe pulses. (c) Time average from 150 to 160 fs of the differential absorption signals ΔA(t) in (b).

3.4.1 Ground State Bleaching: Decrease of Br_2 Molecules in The Electronic Ground State (X)

The spectral region for core-to-valence absorptions is expanded in Figure 3.4. Once a fraction of the Br_2 molecules are excited by the pump pulse, the XUV absorptions of Br_2 molecules in the electronic ground state decreases, shown as the negative $\Delta A(t)$ signals (so-called ground state bleaching[87]) in Figure 3.4(b). The decrease of the $3d_{5/2,3/2} \rightarrow 4p\sigma^*$ absorption doublet leads to the broad negative signals around 67.5-69.5 eV, which are also seen in the snapshot at time zero $\Delta A(t = 0)$ in Figure 3.4(a) and the time average of $\Delta A(t)$ from 150 to 160 fs in Figure 3.4(c). Additionally, the oscillation of ground state bleaching signals encode the dynamics of the coherent vibrational wavepacket[25,40,42,43,5] in the electronic ground state of Br_2 molecules (Appendix).

3.4.2 Excited State Absorption: Br_2 Molecules Pumped to the Electronic Excited State ($C\ ^1\Pi_u\ 1_u$)

As the Br_2 molecules are pumped to the excited state ($C\ ^1\Pi_u\ 1_u$), new XUV absorptions from the C state appear as positive $\Delta A(t)$ signals in Figure 3.4. In particular, a new absorption doublet arises at $t = 0$ due to the $3d_{5/2,3/2} \rightarrow 4p\pi^*$ absorption at 65.02 and 66.01 eV (a). This new absorption doublet of the C state Br_2 molecule is about 3 eV below the original $3d_{5/2,3/2} \rightarrow 4p\sigma^*$ absorption doublet (68.12 and 69.16 eV) of ground state Br_2 molecules. Physically, this shift corresponds to the energy gap between the excited C and ground X states, equivalent to the 3.1 eV photon energy of the 400 nm pump pulse. In addition, the $3d_{5/2} \rightarrow 4p\sigma^*$ absorption from the C state occurs around 67 eV, about 2 eV higher than the $3d_{5/2} \rightarrow 4p\pi^*$ absorption at 65.02 eV. This difference agrees with the 2.1 eV gap between orbital energy of Br_2 $4p\pi^*$ and $4p\sigma^*$ orbitals.

3.4.3 From Molecules to Atoms: Mapping the Motion of the Nuclear Wavepacket on the C State Potential Energy Curve (PEC) By Core-to-Valence Absorptions

After time zero, the C state Br_2 molecule dissociates into two ground state Br atoms

$$Br_2\ (C\ ^1\Pi_u\ 1_u) \rightarrow Br\ (^2P_{3/2}) + Br\ (^2P_{3/2})$$

As a result, the molecular $3d_{3/2,5/2} \rightarrow 4p\pi^*$ absorptions shift toward lower photon energy in Figure 3.4(b), and the absorptions gradually converge to the atomic $3d\ ^2P_{3/2} \rightarrow 4p\ ^2D_{5/2,3/2}$ transitions at 64.31 and 65.34 eV, respectively. The atomic absorption peaks are clearly identified with the time average of $\Delta A(t)$ from 150 to 160 fs in Figure 3.4(c) and Table 3.4. Such a down shift of the XUV absorption energy equals the decreasing energy gap between the C state and the $(3d)^{-1}4p$ core-to-valence excited state (white dash-dot

line, Figure 3.5(b)), as the nuclear wavepacket descends along the C state PEC (Figure 3.5(a)). Hence, the motion of the nuclear wavepacket on the PEC is intuitively visualized in the time-resolved XUV absorption spectrum (Figure 3.5(b)).[38]

In addition to the atomic 3d $^2P_{3/2} \rightarrow$ 4p $^2D_{5/2, 3/2}$ absorptions, a weaker atomic 3d $^2P_{1/2} \rightarrow$ 4p $^2D_{3/2}$ absorption is also observed at 64.89 eV in Figure 3.4(c). This absorption from the atomic $^2P_{1/2}$ excited state is not a dissociation product of the C state but other valence excited states. The presented simulations suggest that a possible state is the Z ($J = 2$) state (Appendix).

Table 3.4. Br core-to-valence 3d → 4p absorptions of dissociated Br atoms.

Atomic Transition	E (eV) This work	E (eV) Ref. [83]	E (eV) Ref. [81]	E (eV) Ref. [25]	E (eV) Ref. [68]
$^2P_{3/2} \rightarrow$ 4p $^2D_{5/2}$	64.31	64.38	64.38	64.4	64.54
$^2P_{1/2} \rightarrow$ 4p $^2D_{3/2}$	64.89	64.97	64.97	65.1	65.13
$^2P_{3/2} \rightarrow$ 4p $^2D_{3/2}$	65.34	65.43	65.43	65.4	65.58

3.4.4 Product Absorption: Buildup Signal of Dissociated Br Atoms and its Fitted Rise Time

The lineout in time for the atomic 3d $^2P_{3/2} \rightarrow$ 4p $^2D_{5/2, 3/2}$ absorptions at 64.31 and 65.34 eV is plotted in Figure 3.5(d, c). Qualitatively, as the Br_2 molecule dissociates, the atomic absorption will increase and converge to a plateau. Quantitatively, to determine the rise time, the atomic differential absorption signal $\Delta A(\mathrm{Br}; t)$ is fitted to a sigmoid function[9,71,72,74,78,79] as

$$\Delta A(\mathrm{Br}; t) = a\,\Phi(t - t_{\mathrm{rise}}) \tag{1}$$

where a is the amplitude, $\Phi(t)$ is the cumulative distribution function (CDF) of the pump pulse shape $f(t)$

$$\Phi(t) = \int_{-\infty}^{t} f(t')dt' \tag{2}$$

and t_{rise} is the time constant for a shift of the CDF function in time, called the apparent rise time. For the atomic 3d $^2P_{3/2} \rightarrow$ 4p $^2D_{5/2, 3/2}$ transitions (64.31 and 65.34 eV, Figure 3.5(d, c)), the fitted values of t_{rise} are 38 ± 1 and 20 ± 5 fs (Here the best estimate ± uncertainty is reported as the mean ± one standard deviation[88] of fitted values for each of 93 measurements.).

The physical meaning of this fit function has been elaborated in Zewail's landmark work

(Section II.B and Appendix therein)[9] and is briefly explained here. This fit function implies that

(1) The absorption of pump pulse from the ground to the C state is assumed instantaneous.[8,9,89] That is, the response function of the molecules or atoms is assumed as a step function (Equation A1 in Ref. [9] and Figure 6(a) in Ref. [7]).

(2) The atomic XUV absorption signals are proportional to the populations pumped to the C state and emerge later with a shift in time by t_{rise} as the molecules in the C state gradually dissociate. [71,72,74,78,79] The shift in time by t_{rise} empirically describes the time scale of the buildup of dissociated atomic signals. It is an apparent rise time because it corresponds to the total measured signal at that photon energy, but not necessarily a single transition if there are degeneracies.

(3) In this work, the pump pulse shape $f(t)$ is the temporal intensity envelope measured from SD-FROG (Figure 3.13(d)), so the realistic effect of finite pump pulse duration and satellite pulses are explicitly considered. In the literature, an ideal Gaussian pulse shape is often used, where the Gaussian CDF equals an error function.[71,72,74,78,79]

(4) If a more sophisticated kinetics modeling is needed, a system of rate equations can be used.[9]

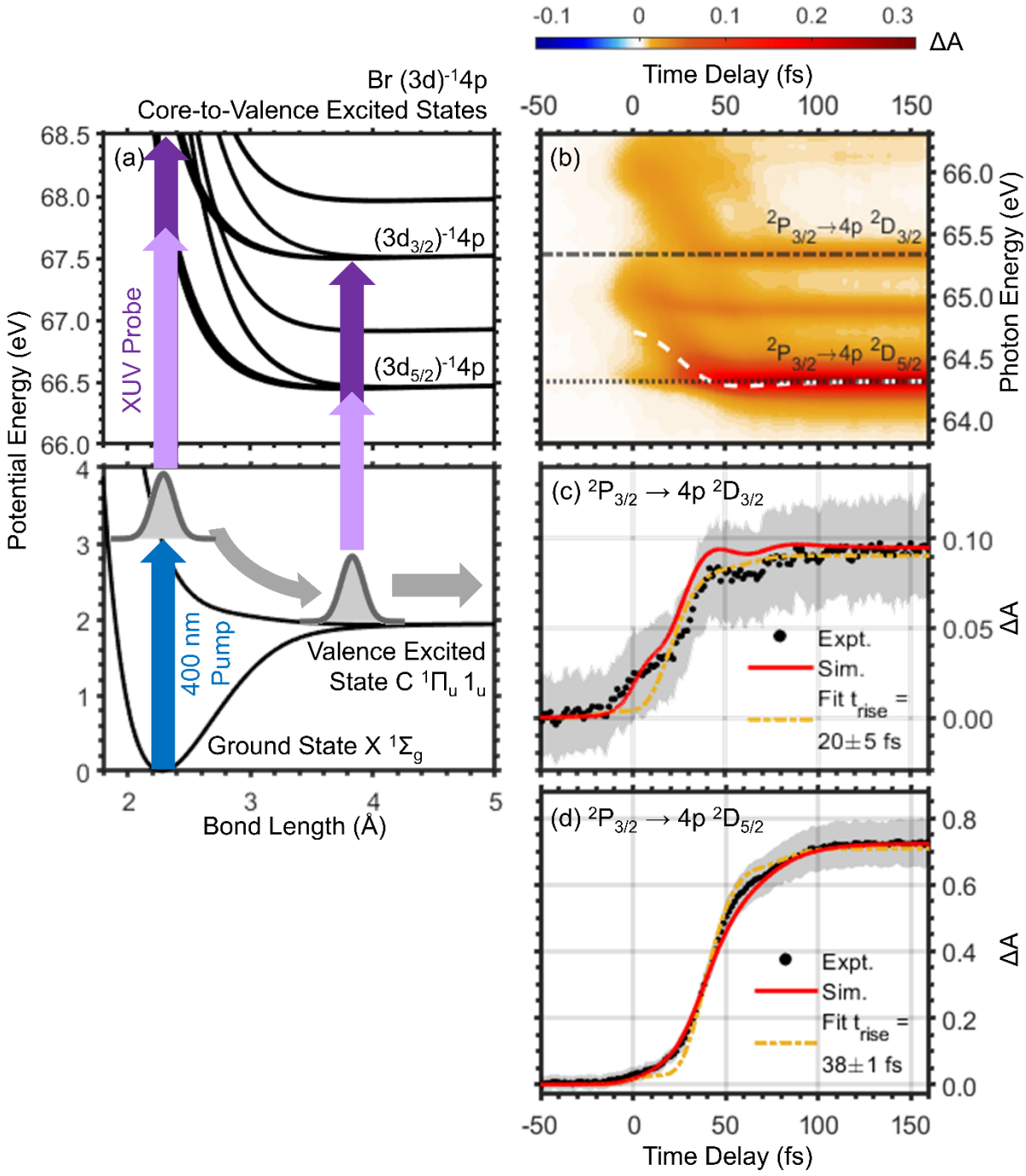

Figure 3.5. Launch and detection of the nuclear wavepacket and dissociation in the valence excited state C. (a) Potential energy curves. (b) Measured time-resolved XUV differential absorption spectrum records the motion of wavepacket on the PEC of C state and the rise of Br atomic absorptions. White dashed line: calculated energy gap between the C state and the Br $(3d_{5/2})^{-1}4p$ core-to-valence excited state. (d, c) Lineout in time of (b) at 64.31 and 65.34 eV for atomic Br $3d\ ^2P_{3/2} \rightarrow 4p\ ^2D_{5/2,3/2}$ absorptions. Black dot and gray shade: the best estimate and the uncertainty of the measured ΔA(t) values (mean and one standard deviation[88] of 93 measurements of ΔA(t) signals). Red solid line: corresponding lineout of

theoretically computed (GAMESS) and simulated time-resolved XUV absorption cross section from C state. Orange dash-dotted line: Fit by a Sigmoid function (Equation 1).

3.4.5 Potential Causes for the Different Rise Times: Comparison between Experiment, Simulation and Theory

3.4.5.1 Comparison Between Experimental and Simulated Time-Resolved XUV Absorption Spectrum and the Underlying Theory

To understand the cause of the two different rise times, the experimental time-resolved absorption spectrum to simulation and the underlying theory is compared. The experimental time-resolved differential absorption spectrum (Figure 3.6(a)) is compared to the simulated time-resolved total absorption cross section of the C state to all core-to-valence excited states (Figure 3.6(b)). The photon energies of 64.31 and 65.34 eV are marked with the black dotted and dash-dotted lines for atomic $^2P_{3/2}$ → 4p $^2D_{5/2}$ and $^2D_{3/2}$ absorptions, and lineouts in time are in Figure 3.5(d and c), respectively. For the lineout in time for each absorption in Figure 3.5(d or c), the measured (black dots) and simulated (red solid line) ΔA signals generally match. As a result, the simulations can capture the main features of the experiments. Next, I will analyze the components of the simulations and identify the potential cause of the different rise times.

The simulations are based on a quasi-classical theory for transient absorption spectroscopy (Appendix).[86] According to the theory, the measured time-resolved *total* absorption cross section $\sigma_{\mathrm{C}}^{\mathrm{total}}(\omega,t)$ (Figure 3.6(b)) at photon energy $\hbar\omega$ from the initial state (here the C state) to all final states ($3d^{-1}4p$ core-to-valence excited states) has two components: (1) the bond-length (R) dependent *total* absorption strength of the C state $\sigma_{\mathrm{C}}^{\mathrm{total}}(\omega,R)$ (Figure 3.6(c)) and (2) the wavepacket trajectory on C state PEC $|\Psi_{\mathrm{C}}(R,t)|^2$ (Figure 3.6(d)) as

$$\sigma_{\mathrm{C}}^{\mathrm{total}}(\omega,t)=\frac{4\pi\omega}{c}\int\sigma_{\mathrm{C}}^{\mathrm{total}}(\omega,R)|\Psi_{\mathrm{C}}(R,t)|^2dR \tag{3}$$

As a result, the measured time-resolved *total* absorption cross section $\sigma_{\mathrm{C}}^{\mathrm{total}}(\omega,t)$ shows not only how the wavepacket moves in time t, but also how the bond-length dependent *total* absorption strength $\sigma_{\mathrm{C}}^{\mathrm{total}}(\omega,R)$ changes with increasing bond length R. The wavepacket trajectory will be discussed later in Section 3.4.6.

3.4.5.2 The Difference between the Two Atomic Absorptions ($^2P_{3/2} \rightarrow$ 4p $^2D_{5/2}$ and $^2D_{3/2}$)

First, the simulated bond-length dependent *total* absorption strength of the C state $\sigma_{\mathrm{C}}^{\mathrm{total}}(\omega, R)$ in Figure 3.6(c) is considered. For the corresponding lineouts in Figure 3.6(e), the lineout of $\sigma_{\mathrm{C}}^{\mathrm{total}}(\omega, R)$ at 65.34 eV (3d $^2P_{3/2} \rightarrow$ 4p $^2D_{3/2}$) (black dash-dotted line) converges to a plateau at a shorter bond length R than that at 64.31 eV (3d $^2P_{3/2} \rightarrow$ 4p $^2D_{5/2}$) (black dotted line). This agrees with the above result that the rise time of 3d $^2P_{3/2} \rightarrow$ 4p $^2D_{3/2}$ absorption (20 ± 5 fs) is faster than that of 3d $^2P_{3/2} \rightarrow$ 4p $^2D_{5/2}$ absorption (38 ± 1 fs) (Figure 3.5).

3.4.5.3 Subtlety in the Atomic Absorption ($^2P_{3/2} \rightarrow$ 4p $^2D_{5/2}$): Merger of Two Branches of Molecular Absorptions (3d $\rightarrow$ 4pπ^* and 4pσ^*)

Furthermore, at 64.31 eV (atomic 3d $^2P_{3/2} \rightarrow$ 4p $^2D_{5/2}$ absorption), the lineout of $\sigma_{\mathrm{C}}^{\mathrm{total}}(\omega, R)$ shows a change in slope around 3 Å (Figure 3.6(e)). According to the full $\sigma_{\mathrm{C}}^{\mathrm{total}}(\omega, R)$ (Figure 3.6(c)), this atomic 3d $^2P_{3/2} \rightarrow$ 4p $^2D_{5/2}$ absorption at 64.31 eV originates from two branches of molecular absorptions from the C state (3d $\rightarrow$ 4pπ^* and 4pσ^*), which start separately around 64.9 and 67.1 eV at the equilibrium bond length R_{eq} and merge together around 3 Å. (Their energy difference at R_{eq} matches the 2.1 eV gap[90] between the orbital energy of 4pπ^* and 4pσ^* at R_{eq}.) As a result, for the lineout at 64.31 eV (Figure 3.6(e)), the molecular 3d $\rightarrow$ 4pπ^* branch is the main contribution before 3 Å. After 3 Å, the other molecular 3d $\rightarrow$ 4pσ^* branch blends in. Such a slope change is also observed in the lineout of the measured spectrum at 64.31 eV (Figure 3.5(d)), of which the slope changes around 50 fs. This phenomenon reveals the subtlety in interpreting the absorption spectrum due to spectral overlap. If multiple molecular absorptions converge to the same atomic absorptions, a single lineout at the photon energy for that atomic absorption actually contains the contributions from different molecular absorptions, complicating the observed timescale.

3.4.5.4 Summary: Two Factors Affecting the Lineout in Photon Energy of Measured Signals

In fact, the bond-length dependent *total* absorption strength of C state $\sigma_{\mathrm{C}}^{\mathrm{total}}(\omega, R)$ (Figure 3.6(c)) is the sum of all absorptions from the C state to each core-to-valence excited state (indexed by α) $\sigma_{\mathrm{C}\rightarrow\alpha}(\omega, R)$ as

$$\begin{aligned} \sigma_{\mathrm{C}}^{\mathrm{total}}(\omega, R) &= \sum_{\alpha} \sigma_{\mathrm{C}\rightarrow\alpha}(\omega, R) \\ \sigma_{\mathrm{C}\rightarrow\alpha}(\omega, R) &= |\mu_{\mathrm{C}\rightarrow\alpha}(R)|^2 g_{\mathrm{C}\rightarrow\alpha}(R, \omega). \end{aligned} \tag{4}$$

where $\mu_{\mathrm{C}\rightarrow\alpha}(\omega, R)$ is the transition dipole moment (TDM) from the C state to the α-th core-to-valence

excited state and $g_{C\to\alpha}(\omega, R)$ is a Lorentzian lineshape function. To summarize, two factors cause the rise times to differ for the lineouts of measured signals at two photon energies. One is how each absorption and its $\mu_{C\to\alpha}(\omega, R)$ value change differently as the bond length increases. The other is the overlap of multiple degenerate absorptions at one XUV photon energy. For instance, when several molecular absorptions merge to the same atomic absorption.

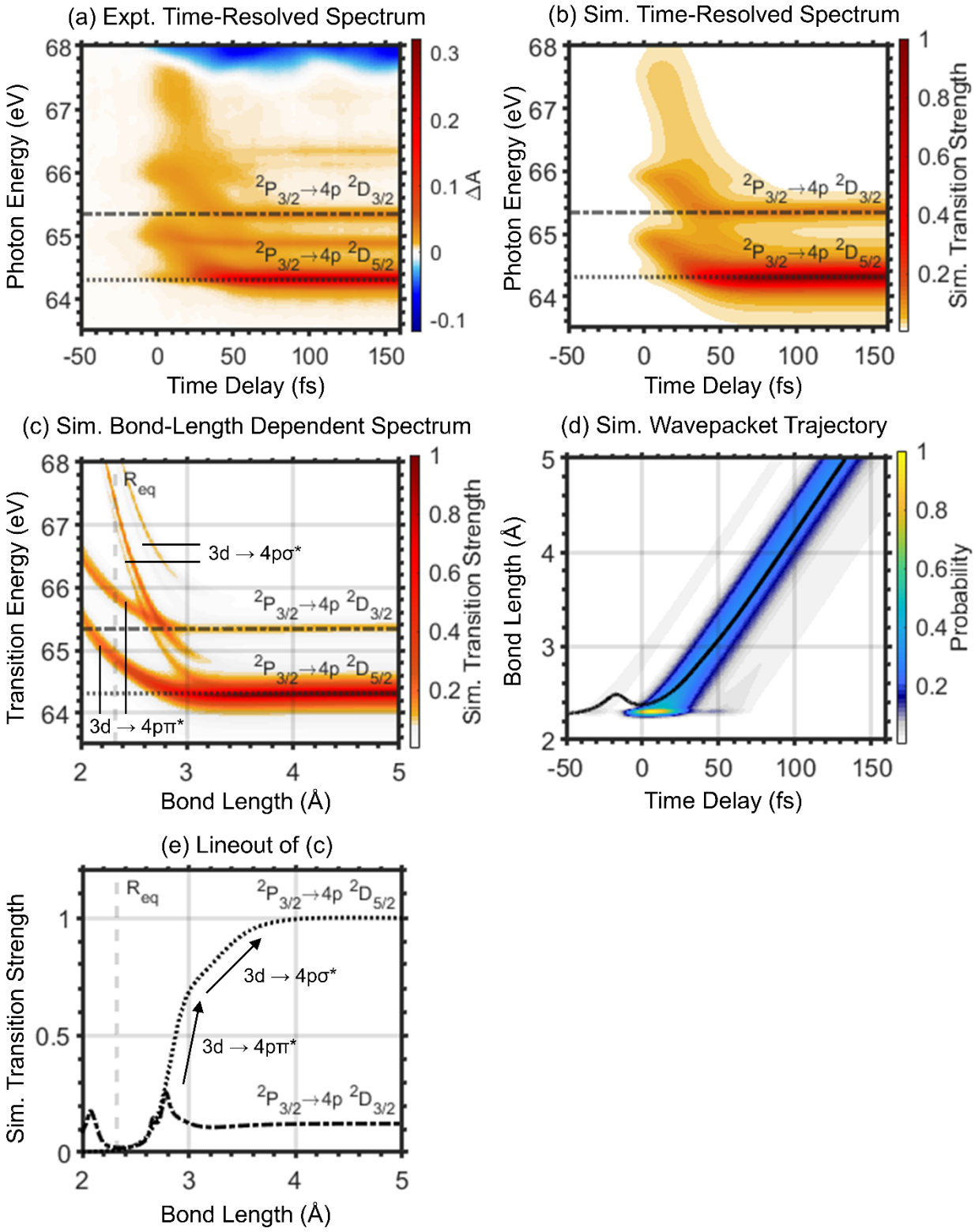
(a) Expt. Time-Resolved Spectrum
Photon Energy (eV)
Time Delay (fs)
ΔA
$^2P_{3/2}\rightarrow 4p\ ^2D_{3/2}$
$^2P_{3/2}\rightarrow 4p\ ^2D_{5/2}$
(b) Sim. Time-Resolved Spectrum
Photon Energy (eV)
Time Delay (fs)
Sim. Transition Strength
$^2P_{3/2}\rightarrow 4p\ ^2D_{3/2}$
$^2P_{3/2}\rightarrow 4p\ ^2D_{5/2}$
(c) Sim. Bond-Length Dependent Spectrum
Transition Energy (eV)
Bond Length (Å)
Sim. Transition Strength
R_{eq}
3d → 4pσ*
3d → 4pπ*
$^2P_{3/2}\rightarrow 4p\ ^2D_{3/2}$
$^2P_{3/2}\rightarrow 4p\ ^2D_{5/2}$
(d) Sim. Wavepacket Trajectory
Bond Length (Å)
Time Delay (fs)
Probability
(e) Lineout of (c)
Sim. Transition Strength
Bond Length (Å)
R_{eq}
3d → 4pσ*
3d → 4pπ*
$^2P_{3/2}\rightarrow 4p\ ^2D_{5/2}$
$^2P_{3/2}\rightarrow 4p\ ^2D_{3/2}$

Figure 3.6. Comparison between experimental and simulated time-resolved XUV core-to-valence absorption spectrum and their components. The dissociated atoms are probed by the atomic 3d $^2P_{3/2} \rightarrow$ 4p $^2D_{5/2}$ and $^2D_{3/2}$ absorptions at 64.31 and 65.34 eV (black dotted line and black dash-dotted line). (a) Experimental time-resolved differential absorption spectrum. (b) Simulated time-resolved total absorption cross section $\sigma_{\mathrm{C}}^{\mathrm{total}}(\omega, t)$ of C state. It is the integral over bond length of (c) simulated bond-length dependent total XUV absorption cross section of C state $\sigma_{\mathrm{C}}^{\mathrm{total}}(\omega, R)$ and (d) simulated wavepacket trajectory on C state PEC $|\Psi_{\mathrm{C}}(R, t)|^2$. (e) Lineout of (c).

3.4.6 Bond Length vs Time: General Agreement across the Literature

The trajectory of the nuclear wavepacket on the PEC of the C state is calculated by numerically solving the nuclear TDSE (Figure 3.7(a)), where the temporal intensity envelope of the pump pulse measured by SD-FROG is used (Figure 3.7(b) and Figure 3.13). The position expectation value of the wavepacket trajectory links the bond length and the time during the dissociation. The agreement with the literature[71,72,74,75,77] (Figure 3.7 and Table 3.5) confirms the validity of the presented nuclear TDSE simulations. More importantly, even though the measured "dissociation times" in the literature could be different by an order of magnitude, how the bond length increases in time is overall consistent across different studies. Reported simulations of the nuclear motion (either classical or quantum wavepacket)[71,72,74,75,77] and this work generally agree that the bond length of Br_2 is double R_{eq} (2.28105 Å)[91] or around 100 to 120 fs.

3.4.7 When does a chemical bond break?

According to the IUPAC Compendium of Chemical Terminology[92] (the Gold Book), dissociation is defined as "The separation of a molecular entity into two or more molecular entities." Here for Br_2, the separation for a diatomic molecule into two atoms can be quantified by the bond length. With the consensus on how bond length increases in time among the literature[71,72,74,75,77] as discussed above, the next question is: At which bond length should the bonding be considered vanished?

To answer this question, various detection methods and criteria have been used (Table 3.1), leading to different "dissociation times" for the Br_2 C $^1\Pi_u$ 1_u state. Even with the same experimental technique, the timescale may differ depending on the specific transitions or how the signal is selected and interpreted. There have been extensive discussions[73–75,77,79] on how the timescales from different experimental techniques may be reconciled or understood. It is important to recognize what and how a phenomenon is observed when one interprets its meaning and connects its corresponding timescale to dissociation.

For future studies, ultrafast electron diffraction (UED) may be used to measure how the bond length changes in time during the dissociation and compare that with existing simulations in the literature. As the temporal resolution of UED (about a hundred fs)[93,94] may be close (in order of magnitude) to the time scale of bond-length separation (double R_{eq} around 100 to 120 fs), the temporal smearing of the observation will need to be tested and considered.

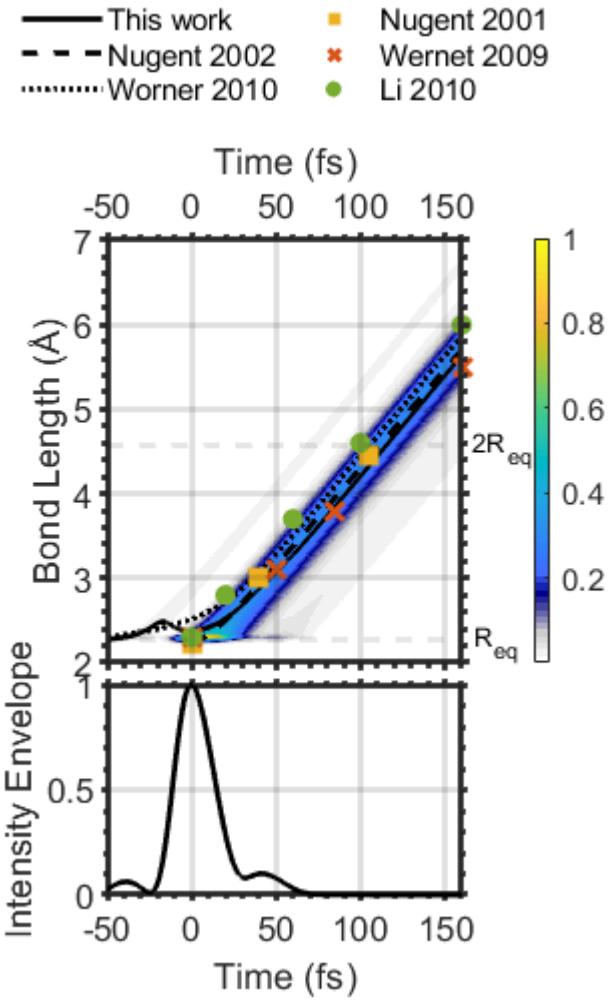

Figure 3.7. (a) Calculated nuclear wavepacket trajectory and its position expectation value (black solid line) on the PEC of excited state C from numerically solving the nuclear TDSE and comparison with the literature. Gray dashed lines: one and double equilibrium bond length R_{eq} = 2.28105 Å.[91] Black dashed line: Adapted with permission from Fig. 5(b) in Ref. [72]. Copyright 2002 AIP Publishing. Black dotted line: Adapted with permission from Fig. S2 in Ref. [75]. Copyright 2010 Springer Nature. Yellow square: Ref. [71]. Red cross: Ref. [74]. Green circle: Ref. [77]. (b) Pump pulse shape (the temporal intensity envelope measured by SD-FROG) used in the TDSE. The effect of small pre- and post-pulses are seen as the additional weaker trajectories before and after time zero.

Table 3.5. Calculated bond length (R) as a function of time (t) for dissociation of Br_2 molecules on the C state PEC.

Reference	t (fs)	R (Å)	R/R_{eq}	R (Å) This work
This work	0	2.28 (R_{eq})	1.00	
	38 ± 1	2.91 ± 0.02	1.25	
	118.2	4.64	2.00	
	166.8	5.80	2.50	
Nugent-Glandorf et al. 2001[71]	0	2.23 (R_{eq})	1.00	2.32
	40	3.00	1.35	2.87
	105	4.46	2.00	4.32
Wernet et al. 2009[74]	0	2.3 (R_{eq})	1.0	2.32
	50 ± 15	3.1 ± 0.3	1.3	3.07 ± 0.20
	85 ± 15	3.8 ± 0.3	1.6	3.85 ± 0.24
	160	5.5	2.4	5.64
Li et al. 2010[77]	0	2.3 (R_{eq})	1.0	2.32
	20	2.8	1.2	2.37
	60	3.7	1.6	2.52
	100	4.6	2.0	4.21
	160	6.0	2.6	5.64

3.5 During Dissociation: Changes in Time-Resolved Br Core-to-Rydberg Absorption Spectrum

3.5.1 Challenges to Interpret the Core-to-Rydberg Absorption Spectrum

So far, the core-to-valence absorptions around 63-70 eV have been analyzed. The core-to-Rydberg absorptions (73-80 eV) are more challenging to interpret, because several different features overlap in the near spectral region. The most prominent one is the overlap of the ground state bleaching of Br_2 molecular absorptions and the emerging Br atomic absorptions as explained below.

3.5.2 Ground State Bleaching: Decrease of Br_2 Molecules in the Electronic Ground State (X)

The region of core-to-Rydberg absorptions (73.5-80 eV) is expanded in Figure 3.8. The decreases in molecular Br_2 $3d_{\delta 5/2} \rightarrow 5p$, $3d_{\pi 3/2} \rightarrow 5p$, and $3d_{\delta 3/2} \rightarrow 5p$ absorptions result in three noticeable negative $\Delta A(t)$ signals around 74.91, 75.09, and 76.02 eV, respectively (Peaks 2, 3 and 7 in Figure 3.8(a) and Table 3.3).

The lineouts in time for these three transitions are plotted in Figure 3.9. Ground state bleaching in core-to-Rydberg absorptions here shows several differences to the core-to-valence ones. First is a strong negative suppression signal around time zero. This signal resembles the shape of the pump pulse and may be a pump-induced effect on the XUV absorption to the core-to-Rydberg excited states. A related phenomenon was reported for the iodine $4d \rightarrow 6p$ core-to-Rydberg absorptions in ICl.[95] Second, no noticeable periodic temporal oscillations are observed in the core-to-Rydberg absorptions.

In addition to these three transitions, the bleaching in other core-to-Rydberg absorptions is also partially observed as the negative $\Delta A(t)$ signals in Figure 3.8(b). However, they are obscured by the overlap of atomic Br core-to-Rydberg absorptions in the same spectral region, as identified in the next section.

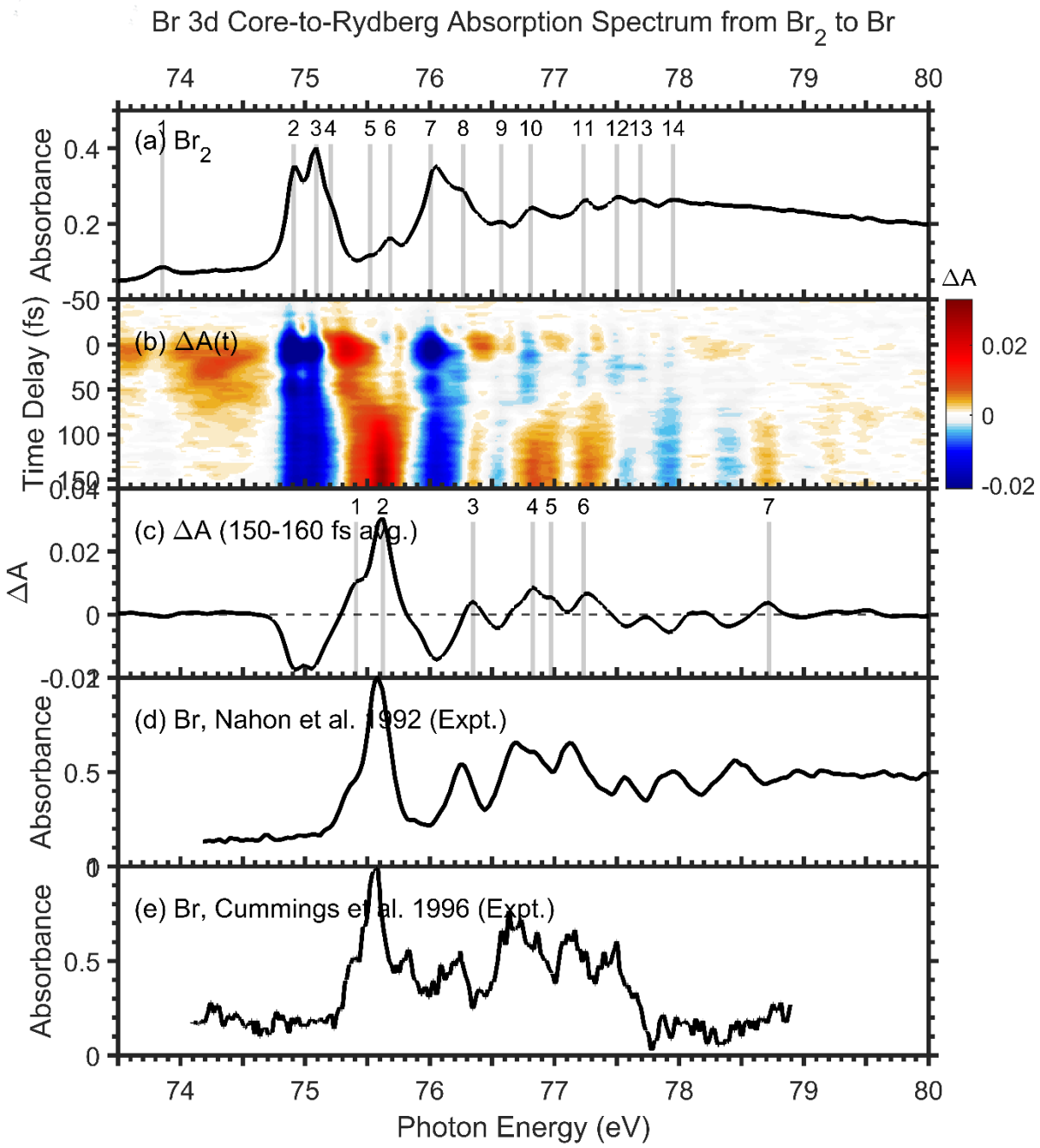

Figure 3.8. Static and time-resolved Br 3d Core-to-Rydberg XUV absorption spectrum of Br_2 molecules and Br atoms. (a) Static absorption spectrum of the Br_2 molecules before dissociation, as assigned earlier in Figure 3.2(b) and Table 3.3. (b) Time-resolved differential absorption spectrum ΔA(t) of the dissociating Br_2 molecule and resulting Br atoms, as a function of the time delay between the visible pump and XUV probe pulses. (c) Time average from 150 to 160 fs of the differential absorption signals ΔA(t) in Figure 3.8(b). New absorptions from dissociated Br atoms lead to positive ΔA (assigned in Table 3.6), while decreased absorptions from original Br_2 molecules lead to negative ΔA. (d) Measured static

absorption spectrum of Br atoms by photoelectron spectroscopy (average photon-energy resolution 0.18 eV). Adapted with permission from Ref. [82]. Copyright 1992 American Physical Society. (e) Measured static absorption spectrum of Br atoms by absorption spectroscopy (measurement accuracy ±0.03 eV). Adapted with permission from Ref. [83]. Copyright 1996 American Physical Society.

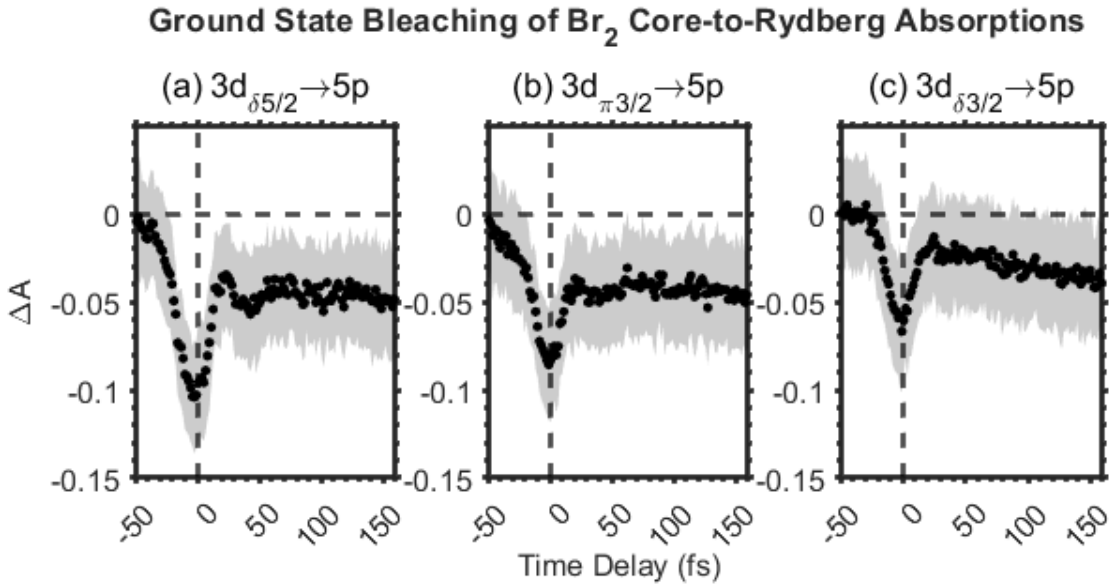

Figure 3.9. Differential absorption ΔA(t) signal as a function of time delay for selected Br_2 core-to-Rydberg absorptions. (a, b, c) Peaks 2, 3 and 7 in Figure 3.8(a) and Table 3.3. Black dot and gray shade: best estimate (mean) and uncertainty (one standard deviation)[88] of 93 measurements. In addition to the ground state bleaching, a strong negative suppression signal is seen around time zero, potentially due to pump-induced effects.[95]

3.5.3 Product Absorption: Identification of Dissociated Br Atoms by Core-To-Rydberg Absorption Spectrum at Long Time Delay

New absorptions from dissociated Br atoms lead to positive ΔA(t) signals in Figure 3.8(b, c). The positive ΔA peaks in Figure 3.8(c) are compared to the static absorption spectra of Br atoms from the literature[82,83] in Figure 3.8(d, e). Generally, the overall shapes of the spectra agree with each other, and several noticeable peaks in Figure 3.8(c) are identified and assigned (Table 3.6). In addition, numerous other atomic Br core-to-Rydberg absorptions exist in this spectral region, and previous researchers pointed out the complexity of such atomic halogen core-to-Rydberg absorptions.[82] Readers are referred to the specific literature for detailed assignments.[82,83,96]

3.5.4 Product Absorption: Time Evolution of the Atomic Br Core-to-Rydberg Absorptions

The lineout in time for the identified positive ΔA peaks in Figure 3.8(c) are plotted in Figure 3.10. Ideally, the signal from dissociated Br atoms should rise around time zero and converge to a positive plateau at long time delay, similar to the atomic Br core-to-valence signals (Figure 3.5(c, d)). However, multiple additional factors complicate the analysis.

First is the overlap of various atomic Br and molecular Br_2 core-to-Rydberg absorptions (Figure 3.8). If the ground state bleaching of molecular absorptions is stronger than emerging atomic absorptions, the measured total ΔA signal at that photon energy may be dragged down and appear as a negative signal around time zero (Figure 3.10(d, e, f)). Such an overlap issue was not significant for core-to-valence absorptions, because major atomic (64.0-65.5 eV) and molecular (67.5-69.5 eV) core-to-valence absorptions are sufficiently separated in photon energy (Figure 3.4).

Second is the need for a longer time span. In principle, at sufficiently long time delay, the molecules will fully dissociate into isolated atoms, and the atomic ΔA(t) signals will totally converge to a positive plateau. Such convergence is observed for the atomic Br core-to-valence absorptions (Figure 3.5(c, d)). In contrast, for the atomic core-to-Rydberg absorptions (Figure 3.10), the signals seem to continue rising at the largest time delay (160 fs). As a result, a longer time span will be necessary to see the full growth of the signals.

Third, the signal-to-noise ratio (S/N)[97,98] of core-to-Rydberg absorptions (Figure 3.10) is lower than the core-to-valence ones (Figure 3.5(c, d)), because the XUV spectrum (Figure 3.11) is weaker beyond 72 eV due to the cutoff of the Al filter. In this work, one Al filter blocks the driving field before the sample cell and one Zr filter blocks the pump before the grating and XUV camera. It may be more favorable to use two Zr filters to avoid the loss of XUV intensity beyond the Al cutoff (> 72 eV).

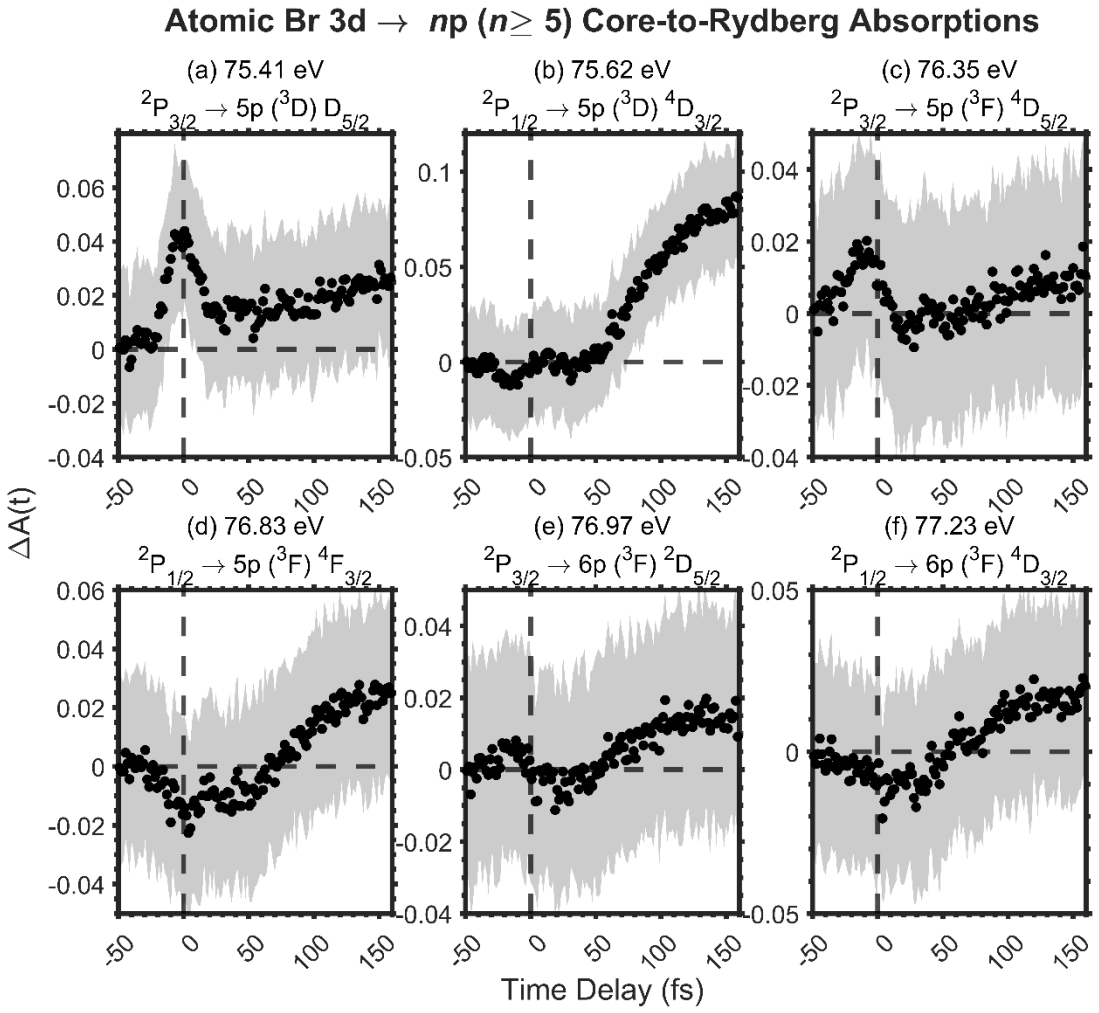

Figure 3.10. Differential absorption ΔA(t) signal as a function of time delay for selected atomic Br core-to-Rydberg absorptions in Figure 3.8(c) and Table 3.6. Black dot and gray shade: best estimate (mean) and uncertainty (one standard deviation)[88] of 93 measurements.

Table 3.6. Atomic Br core-to-Rydberg 3d → *n*p (*n* ≥ 5) absorptions (Figure 3.8), assigned according to Ref. [83].

Peak	Atomic Transition[83]	E (eV) (Theory) Ref. [83]	E (eV)[a, b] Ref. [82,83] (Figure 3.8(d))	E (eV)[c] Ref. [83] (Figure 3.8(e))	E (eV)[d] This work (Figure 3.8(c))
1	$^2P_{3/2} \rightarrow 5p\ (^3D)\ ^2D_{5/2}$	75.42	75.35	75.39	75.41
2	$^2P_{1/2} \rightarrow 5p\ (^3D)\ ^4D_{3/2}$	75.63	75.60	75.56	75.62
	$^2P_{3/2} \rightarrow 5p\ (^3F)\ ^2D_{5/2}$	75.66			
3	$^2P_{3/2} \rightarrow 5p\ (^3F)\ ^4D_{5/2}$	76.27	76.30	76.22	76.35
	$^2P_{3/2} \rightarrow 5p\ (^3F)\ ^4F_{5/2}$	76.35			
4	$^2P_{3/2} \rightarrow 5p\ (^3P)\ ^2D_{5/2}$	76.67			
	$^2P_{1/2} \rightarrow 5p\ (^3F)\ ^4F_{3/2}$	76.70	76.70	76.70	76.83
	$^2P_{3/2} \rightarrow 6p\ (^3D)\ ^2P_{3/2}$	76.72			
	$^2P_{3/2} \rightarrow 5p\ (^3P)\ ^2S_{1/2}$	76.73			
	$^2P_{1/2} \rightarrow 5p\ (^3P)\ ^4D_{3/2}$	76.76			
5	$^2P_{3/2} \rightarrow 6p\ (^3F)\ ^2D_{5/2}$	76.93	76.85	76.85	76.97
	$^2P_{3/2} \rightarrow 5p\ (^1F)\ ^2D_{5/2}$	77.06			
6	$^2P_{1/2} \rightarrow 6p\ (^3F)\ ^4D_{3/2}$	77.20	77.15	77.16	77.23
7	$^2P_{1/2} \rightarrow 7p\ (^3F)\ ^4F_{3/2}$	78.49	78.40		78.72

[a] Measured spectrum in Ref. [82] with numeric values reported in Ref. [83]

[b] Absorption spectroscopy[82] (measurement accuracy ±0.03 eV)

[c] Photoelectron spectroscopy[83] (average photon-energy resolution 0.18 eV)

[d] XUV absorption spectroscopy

3.6 Conclusions

In this work, the buildup of atomic Br 3d core level absorptions is used to estimate the progress of dissociation. Notably, the measured rise time depends on the probed final state: 38 ± 1 and 20 ± 5 fs for core-to-valence absorptions (Br 3d $^2P_{3/2} \rightarrow 4p\ ^2D_{5/2}$ and $^2D_{3/2}$ at 64.31 and 65.34 eV). On the other hand, the rise times are not determined for core-to-Rydberg absorptions due to spectral overlaps with ground-state bleaching.

With the aid of simulations, the presented results suggest that the measured probing signals contain not only the wavepacket dynamics but also how each probing transition changes differently with bond length. These potential probe-dependent effects should be considered when interpreting measured signals and their timescales. This may partially explain why the reported "dissociation time" are so different from various experimental probing methods in the literature[71–78] (Table 3.1).

In addition, this work maps out thoroughly the evolution of the Br 3d core-to-valence and core-to-Rydberg absorptions from molecular to atomic limits in time. The presented time-resolved spectrum bridges the static spectra reported separately for Br_2 molecules and Br atoms across the scattered literature[25,68,80–84] (Table 3.3).

3.7 Appendix

3.7.1 Experimental Method: Time-Resolved XUV Absorption Spectroscopy

3.7.1.1 Broadband XUV Probe Pulse

The experiments are performed using the output of a Ti:Sapphire amplified laser (Coherent Astrella), producing pulses at 1 kHz repetition rate centered at approximately 800 nm, with a 35 fs full-width half-maximum (FWHM) duration and 7 mJ pulse energy. The output is split by a 30/70 beam-splitter, with 2.1 mJ being used to generate the XUV probe, and a portion of the remaining 4.9 mJ being used to generate the visible pump. In the probe arm, the near-infrared (NIR) pulses are spectrally broadened through self-phase modulation in a neon gas-filled (2.4 bar) stretched hollow-core fiber (1.5 m long, 400 μm inner diameter), resulting in octave spanning spectra supporting a few-cycle duration. These pulses are temporally compressed to about 4 fs duration using a set of broadband dispersion compensating mirrors in combination with a 2 mm-thick ADP plate and fused-silica wedges to fine tune the second and third order dispersion. The XUV pulses are generated through the process of high-order harmonic generation, obtained by tightly focusing (f = 0.6 m) the few-cycle NIR pulses near the opening of a ceramic gas cell (2 mm path length) backed by 80 Torr of neon gas. The XUV beam is spectrally isolated from the NIR driving field by a 100 nm thick Al filter, and the focus is reimaged through grazing-incidence reflection from a gold-coated toroidal mirror onto the sample gas-cell (stainless-steel). After the

sample cell, the XUV beam is transmitted through a 200 nm Zr filter and recorded by a spectrograph (Figure 3.11).

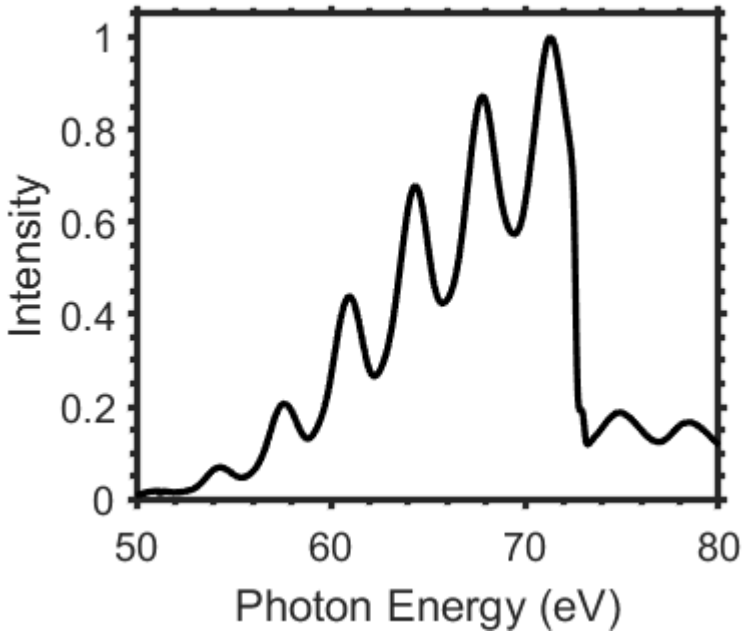

Figure 3.11. Spectrum of the broadband XUV probe pulses after a 0.1 μm Al filter and a 0.2 μm Zr filter.

3.7.1.2 Femtosecond 400 nm Pump Pulse

In the pump arm, 70% of the Astrella output (35 fs) is used to generate visible pulses centered at 400 nm by frequency doubling the 800 nm light in a beta barium-borate (BBO) crystal. After isolation from the fundamental field, the visible pulses are free-space focused inside a neon-filled (1.7 bar) tube (1.37 m long, KF 25 and KF 40 flange in diameter) to gently broaden the spectrum[99] (Figure 3.12). The output is then compressed by 8 chirped mirrors (Ultrafast Innovations CM82) (total 14 reflections by double reflections on the 1st to 6th mirrors and single reflection on 7th and 8th mirrors). The pulse duration of the main pulse is fitted to be 26±1 fs from a Self-Diffraction Frequency Resolved Optical Gating (SD-FROG) measurement (Figure 3.13).

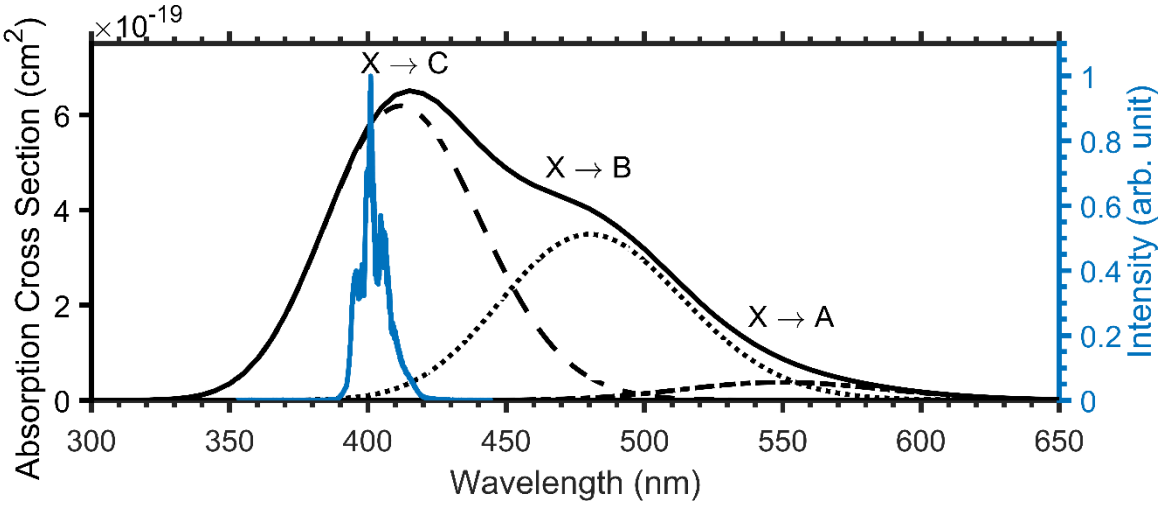

Figure 3.12. Spectrum of 400 nm pump pulse in this work (blue solid line) and visible absorption spectrum of Br_2 from the literature.[100,101] Black solid line: total absorption cross section. Black dash-dot, dotted, and dashed lines: X ($^1\Sigma_g^+$) → A ($^3\Pi_u$ 1_u), B ($^3\Pi_u$ 0_u^+), and C ($^1\Pi_u$ 1_u) absorptions, respectively. The individual absorptions are deconvoluted according to Equation 11 in Ref. [100].

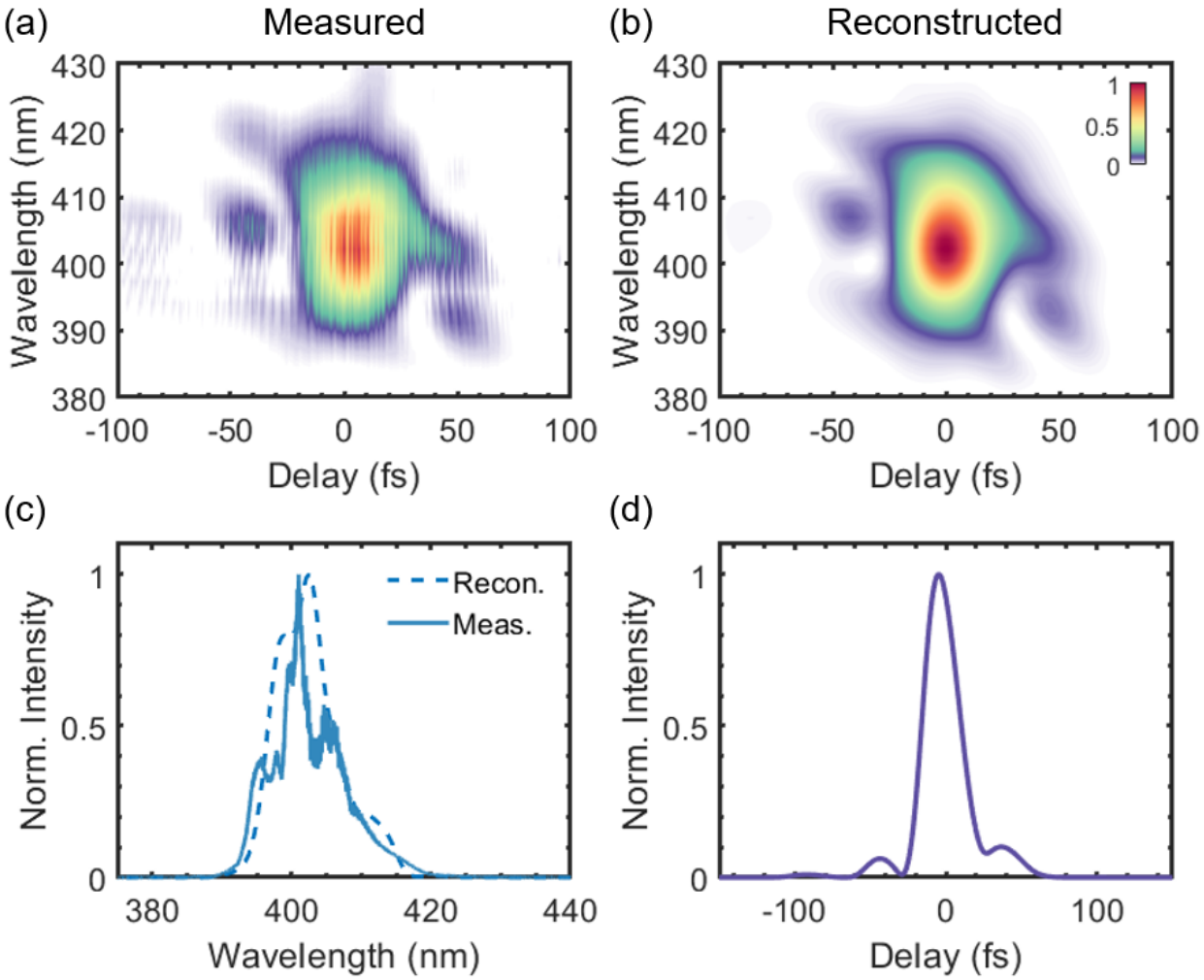

Figure 3.13. Self-Diffraction Frequency Resolved Optical Gating (SD-FROG) measurement of 400 nm pump pulse. (a) Measured and (b) reconstructed spectrogram. (c) Measured (solid line) and reconstructed (dash line) spectrum. The central wavelength is around 400 nm. (d) Reconstructed temporal intensity envelope. The pulse duration is 26±1 fs FWHM from fitting the main pulse to a Gaussian function.

3.7.1.3 Time-Resolved XUV Absorption Spectroscopy

The 400 nm pump beam is recombined with the XUV beam at the sample cell using a noncolinear geometry, where the 400 nm beam is focused to approximately 109 μm in diameter and crossed with the XUV beam. In all measurements, the 400 nm pump and XUV probe have horizontal and vertical polarizations, respectively. After the sample cell, the visible beam is removed by a 0.1 μm thick Zr filter and the transmitted XUV beam is collected using a home-built XUV spectrograph (a concave grating and a XUV CCD camera). The pump pulse is estimated to have 17 to 18 μJ in pulse energy, 109 μm in diameter[5] and 13.5×10^{12} W/cm^2 of peak intensity at the interaction region with Br_2.

At the sample cell, the 400 nm pump and XUV probe pulses interact with molecular bromine vapor (Sigma Aldrich), which is delivered from a liquid reservoir held at room temperature (298 K). The time-resolved XUV differential absorption spectra $\Delta A(E_{XUV}, \tau)$ are calculated from the XUV spectrum of Br_2 with ($I_{XUV+pump}$) and without (I_{XUV}) the 400 nm pump pulses as

$$\Delta A(E_{\mathrm{XUV}}, \tau) \equiv -\log_{10} \frac{I_{\mathrm{XUV+pump}}(E_{\mathrm{XUV}}, \tau)}{I_{\mathrm{XUV}}(E_{\mathrm{XUV}}, \tau)} \tag{5}$$

where positive time delay τ means the pump pulse arrives before the probe pulse. In addition, the static XUV absorbance of Br_2 (without pump pulse) is calculated from the XUV spectrum with (I_{XUV}) and without ($I^{(0)}_{\mathrm{XUV}}$) Br_2 molecules in the sample cell as

$$\Delta A(E_{\mathrm{XUV}}) \equiv -\log_{10} \frac{I_{\mathrm{XUV}}(E_{\mathrm{XUV}})}{I^{(0)}_{\mathrm{XUV}}(E_{\mathrm{XUV}})} \tag{6}$$

The dataset comprises 93 scans collected using a 300 ms integration time and 1.5 fs delay step from -50 fs to +160 fs. Edge pixel referencing[102] is implemented to suppress source noise introduced by variations in the high-harmonic spectrum.

3.7.1.4 Temporal and Spectral Resolution

The temporal resolution (instrument response function) is estimated as 26 ± 3 fs, which is the FWHM of the Gaussian from fitting the lineout of time-resolved absorption (cross-correlation of 400 nm pump and XUV probe pulses) of the He 2s2p state to an exponentially modified Gaussian (Figure 3.14). This agrees with the 26 ± 1 fs FWHM pulse duration from SD-FROG measurement (Figure 3.13). The spectral resolution is estimated as 32 ± 14 meV, which is the FWHM of the Gaussian from fitting the static He 2s2p absorption lineshape[65] (60.144 ± 0.001 eV) to a Fano-Gaussian lineshape (Figure 3.15).[103]

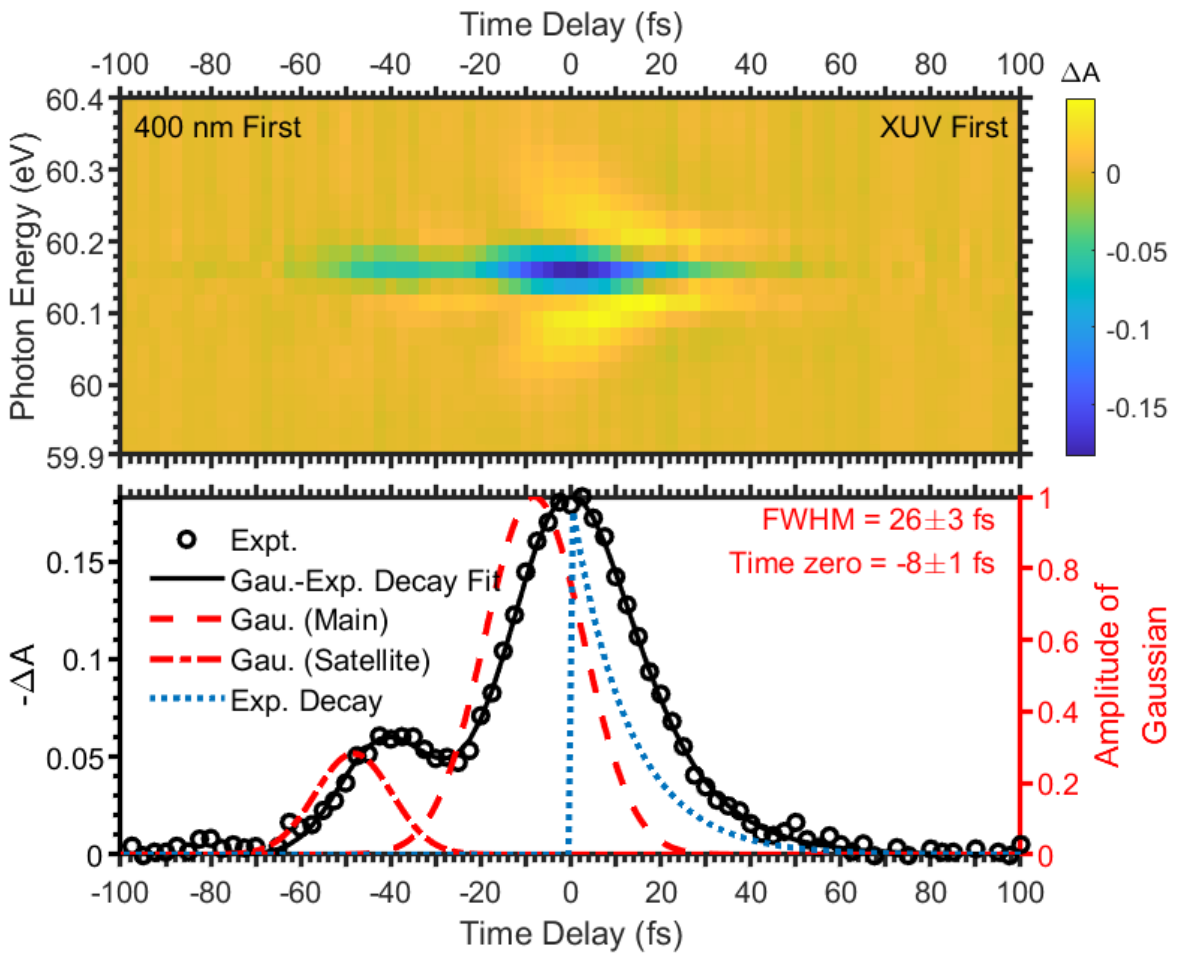

Figure 3.14. The cross-correlation measurement of 400 nm pump and XUV probe pulses in He 2s2p state. (a) Time-resolved XUV differential absorption (ΔA) spectrum of He 2s2p state at 60.16 eV (60.147 eV in the literature[65]). (b) Circles: Time trace extracted by singular value decomposition (SVD) of (a). Red solid line: Fit by an exponentially modified Gaussian function. The FWHM of the fitted Gaussian of the main pulse is 26 ± 3 fs, which is taken as the temporal resolution (instrument response function) for this work.

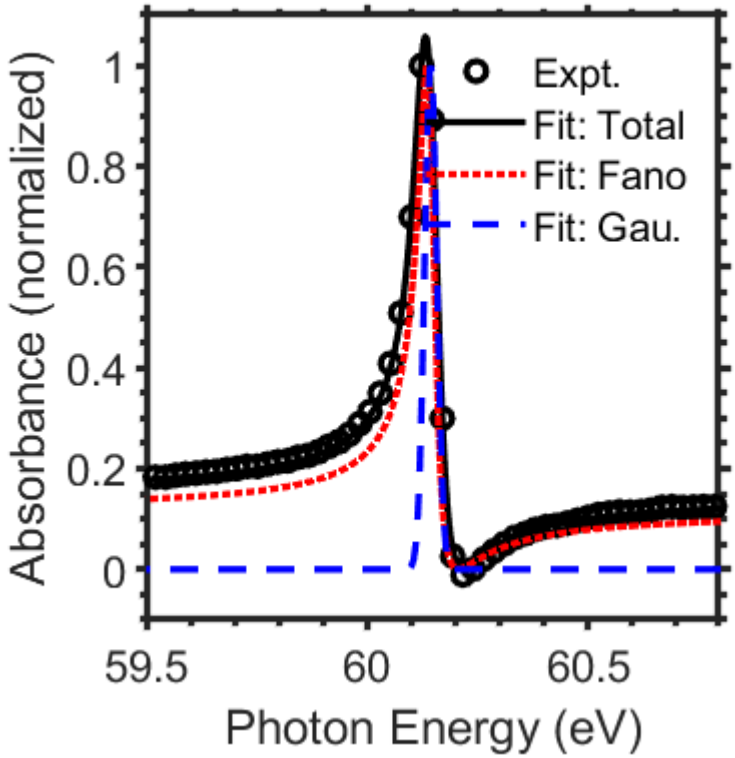

Figure 3.15. The measured and fitted absorption lineshape of He 2s2p state. Black circles: measured data. Black line: total fit of Fano-Gaussian lineshape function. Red dotted line: fitted Fano lineshape function. The fitted center E_r is 60.144 ± 0.001 meV, width Γ is 45 ± 11 meV. Blue dashed line: fitted Gaussian function. The fitted FWHM is 32 ± 14 meV, which is taken as the spectral resolution of the XUV spectrograph around this photon energy region.

3.7.2 Computational Method

3.7.2.1 Electronic Structure Calculations

The electronic structure of Br_2 is calculated using Spin-Orbit General Multi-Configurational Quasi-Degenerate Perturbation Theory (SO-GMC-QDPT)[104–107] in a developer version of GAMESS US.[85,108] A model core potential with basis sets of triple-zeta quality (MCP-TZP)[109–111] was used to replace the $1s^2 2s^2 2p^6 3s^2 3p^6$ electrons, and the remaining $3d^{10} 4s^2 4p^5$ electrons are explicitly considered. A Hartree-Fock calculation is performed to obtain the molecular orbitals used for multiconfigurational self-consistent field (MCSCF) calculations. Two active spaces are set up using the Occupation-Restricted-Multiple-Active-Space (ORMAS) scheme.[112] The valence active space has ten electrons in six Br 4p orbitals and is a complete active space where all possible excitations are allowed, resulting in 66 4p valence states. The core active space has twenty electrons in ten Br 3d orbitals. Only single excitations are allowed from the 3d core-active space to the 4p valence-active space, leading to a total of 240 3d-to-4p core-to-

valence singly excited states. In the MCSCF calculations, all (66) 4p valence states, and the lower half (120) of the core-excited states with relevant energy are included.

Potential energy curves (PEC) and transition dipole moments (TDM) were calculated for bond lengths of 1.80 to 5.00 Å using a 0.01 Å spacing and were extrapolated to longer bond lengths when needed. The calculated equilibrium bond length R_{eq} is 2.28 Å. To reproduce the experimental energy of the 3d-to-4p transition,[68] the PECs of core-excited states were shifted upwards by 0.341 eV. To reproduce the splitting between 3d-to-4p $^2D_{5/2}$ and $^2D_{3/2}$ core-excited states, the effective one-electron spin-orbit-coupling integrals for ten Br 3d orbitals were scaled down 33.5%. To reproduce the spin-orbit splitting between $^2P_{3/2}$ and $^2P_{1/2}$ valence states,[113] an effective nuclear charge of Z_{eff} = 41.40 was used. Table 3.7 shows the vertical excitation energies from the electronic ground state at R_{eq} to several low-lying valence electronic excited states of Br_2.

Table 3.7. Excitation energies from the electronic ground state ($^1\Sigma_g^+$) at the equilibrium bond length to several low-lying valence excited states of Br_2.

State Classification[91,114]			Dissociation Products	E (eV)[115] (Theory)[a]	E (eV) (Theory)[b]	E (eV)[100] (Expt.)[c]	λ (nm)[100] (Expt.)
Alpha-betical	Hund's case (a)	Hund's case (c)					
X	$^1\Sigma_g^+$	0_g^+	$^2P_{3/2} + {}^2P_{3/2}$	0.00	0.00	0.00	0.00
A	$^3\Pi_u$	1_u	$^2P_{3/2} + {}^2P_{3/2}$	2.45	2.35	2.26	549.3
B	$^3\Pi_u$	0_u^+	$^2P_{3/2} + {}^2P_{1/2}$	2.66	2.55	2.58	480.2
C	$^1\Pi_u$	1_u	$^2P_{3/2} + {}^2P_{3/2}$	3.16	3.04	3.01	411.9

[a] Method: MR-CISD+Q

[b] Method: SO-GMC-QDPT. This work.

[c] Converted from measured wavelength λ (nm).

3.7.2.2 Simulation: Nuclear Wavepacket Dynamics

To simulate the motion of the nuclear wavepacket, the nuclear time-dependent Schrodinger equation (TDSE) in atomic units is numerically solved as

$$i\frac{\partial}{\partial t}\Psi(R,t) = H(R,t)\Psi(R,t) \tag{7}$$

The Hamiltonian explicitly includes the interaction of the pump laser pulse and the molecule as

$$H(R,t) = -\frac{1}{2M}\frac{\partial^2}{\partial R^2} + V(R) - \boldsymbol{\mu}(R)\cdot\boldsymbol{E}_{\text{pump}}(t) \tag{8}$$

where M is the reduced mass of the Br_2 molecule, V are the valence electronic state potentials, E_{pump} is the electric field of the pump laser pulse, and μ is the transition dipole moment between selected valence electronic states. The V and μ are obtained from the output of the MCSCF calculations. The pulse shape used in the simulations are the temporal intensity envelope from SD-FROG measurements with 26±1 fs FWHM duration of the main pulse, 400 nm central wavelength, and 13.5×10^{12} W/cm^2 peak intensity.

The TDSE was written using a sinc-function Discrete Variable Representation (sinc-DVR),[116] with bond length ranging from 1.80 to 10.00 Å at 0.01 Å spacing. The short-iterative Arnoldi method[117,118] was used to propagate the wavefunction, from -50 to 160 fs with 50 as (0.050 fs) time steps. The initial wave function is the vibrational ground state of the electronic ground state X ($^1\Sigma_g^+$). Transition pathways include the one-photon excitations from X ($^1\Sigma_g^+$) to C ($^1\Pi_u$ 1_u), from X ($^1\Sigma_g^+$) to B ($^3\Pi_u$ 0_u^+), and from C ($^1\Pi_u$ 1_u) to Z (J = 2) state.

3.7.2.3 Simulation: Time-Resolved XUV Absorption Spectrum

The theory framework for the transient absorption by Lee et al.[86] is used. According to Equation 5 in Ref. [86], the time-resolved (transient) absorption cross section $\sigma_{i\to\alpha}(\omega,t)$ from the *i*-th valence electronic state to the α-th core-to-valence excited electronic state is approximated as the integral over bond length (R) of two components: (1) the bond-length dependent absorption strength from the *i*-th to α-th state $\sigma_{i\to\alpha}(\omega,R)$ and (2) the wavepacket trajectory $|\Psi_i(R,t)|^2$ on the potential energy curve (PEC) of the *i*-th state

$$\sigma_{i\to\alpha}(\omega,t) \equiv \frac{4\pi\omega}{c}\int \sigma_{i\to\alpha}(\omega,R)|\Psi_i(R,t)|^2 dR \tag{9}$$

$$\sigma_{i\to\alpha}(\omega,R) \equiv |\mu_{i\to\alpha}(R)|^2 g_{i\to\alpha}(R,\omega) \tag{10}$$

where ω is the angular frequency of the light, $\mu_{i\to\alpha}(\omega,R)$ is the transition dipole moment between states *i* and α at bond length R, and $g_{i\to\alpha}(\omega,R)$ is a Lorentzian lineshape function defined as

$$g_{i\to\alpha}(R,\omega) = \frac{\Gamma}{\Gamma^2 + [V_\alpha(R) - V_i(R) - \hbar\omega]^2} \tag{11}$$

where Γ is a width parameter (100 meV[68]), and $V_i(R)$ and $V_\alpha(R)$ represent the energy of the *i*-th valence electronic state and the α-th core-to-valence excited state at bond length R, respectively.

The time-resolved *total* absorption cross section $\sigma_i^{\text{total}}(\omega,t)$ from the *i*-th valence electronic state is an incoherent sum over all absorptions $\sigma_{i\to\alpha}(\omega,t)$ to each core-to-valence excited electronic state (α) as

$$\begin{aligned}
\sigma_i^{\text{total}}(\omega,t) &= \sum_\alpha \sigma_{i\to\alpha}(\omega,t) \\
&= \sum_\alpha \frac{4\pi\omega}{c}\int \sigma_{i\to\alpha}(\omega,R)|\Psi_i(R,t)|^2 dR \\
&= \frac{4\pi\omega}{c}\int \Big\{\sum_\alpha \sigma_{i\to\alpha}(\omega,R)\Big\}|\Psi_i(R,t)|^2 dR \\
&= \frac{4\pi\omega}{c}\int \sigma_i^{\text{total}}(\omega,R)|\Psi_i(R,t)|^2 dR
\end{aligned} \tag{12}$$

where $\sigma_i^{\text{total}}(\omega,R)$ is the bond-length dependent *total* absorption strength from the *i*-th state.

3.7.3 Potential Pathway for Dissociation Product Br ($^2P_{3/2}$) + Br* ($^2P_{1/2}$)

The C state molecule dissociates into two ground state ($^2P_{3/2}$) atoms

$$Br_2\ (^1\Pi_u\ 1_u\ C) \rightarrow Br\ (^2P_{3/2}) + Br\ (^2P_{3/2}),$$

which are probed by atomic 3d $^2P_{3/2} \rightarrow$ 4p $^2D_{5/2}$ and $^2D_{3/2}$ transitions at 64.31 and 65.34 eV, respectively. However, a weaker atomic 3d $^2P_{1/2} \rightarrow$ 4p $^2D_{3/2}$ absorption (64.89 eV) is also observed in Figure 3.16(b). This transition from the atomic $^2P_{1/2}$ excited state is not the dissociation product of the C state but other valence excited states. As a result, it is needed to consider valence excited states of which dissociation products are Br ($^2P_{3/2}$) + Br* ($^2P_{1/2}$). One possibility is the B ($^3\Pi_u\ 0_u^+$) state, but it is considered less likely for reasons as follows. First, at the equilibrium bond length, the absorption to the B ($^3\Pi_u\ 0_u^+$) state from the ground state peaks at 480 nm, which is far from the 400 nm center wavelength of the pump pulse (Figure 3.12). Second, if the B state is populated, the 3d → 4p absorptions from the B state will start at 65.59 and 66.51 eV at time zero, as in the simulated absorption spectrum (Figure 3.17(f)).

Instead, it is suggested that the dissociation product Br ($^2P_{3/2}$) + Br* ($^2P_{1/2}$) comes from another valence excited state, tentatively attributed to the Z (J = 2) state. According to electronic structure calculations, the Z (2) state is 2.89 eV above the C state at equilibrium bond length, which is closest to the pump pulse bandwidth. As a result, one-photon absorption of the pump pulse from C state may populate the Z (2) state (Figure 3.16(a)). A similar phenomenon has been observed in visible excitation of iodine molecule.[38]

It turns out that the experimental time-resolved absorption spectrum (Figure 3.16(b, c) and Figure 3.17(a)) agrees the best with simulations from 90% of the C state plus 10% of the Z state in Figure 3.17(b). The scaling matches the observed branching ratio Br ($^2P_{3/2}$):Br* ($^2P_{1/2}$) at long time delays. The simulated spectra from C, Z and B states are individually normalized in Figure 3.17(d, e, f). The agreement between experimental and simulated spectra suggests that the dissociation product Br ($^2P_{3/2}$) + Br* ($^2P_{1/2}$) originates more likely from the Z (2) state than the B ($^3\Pi_u\ 0_u^+$) state.

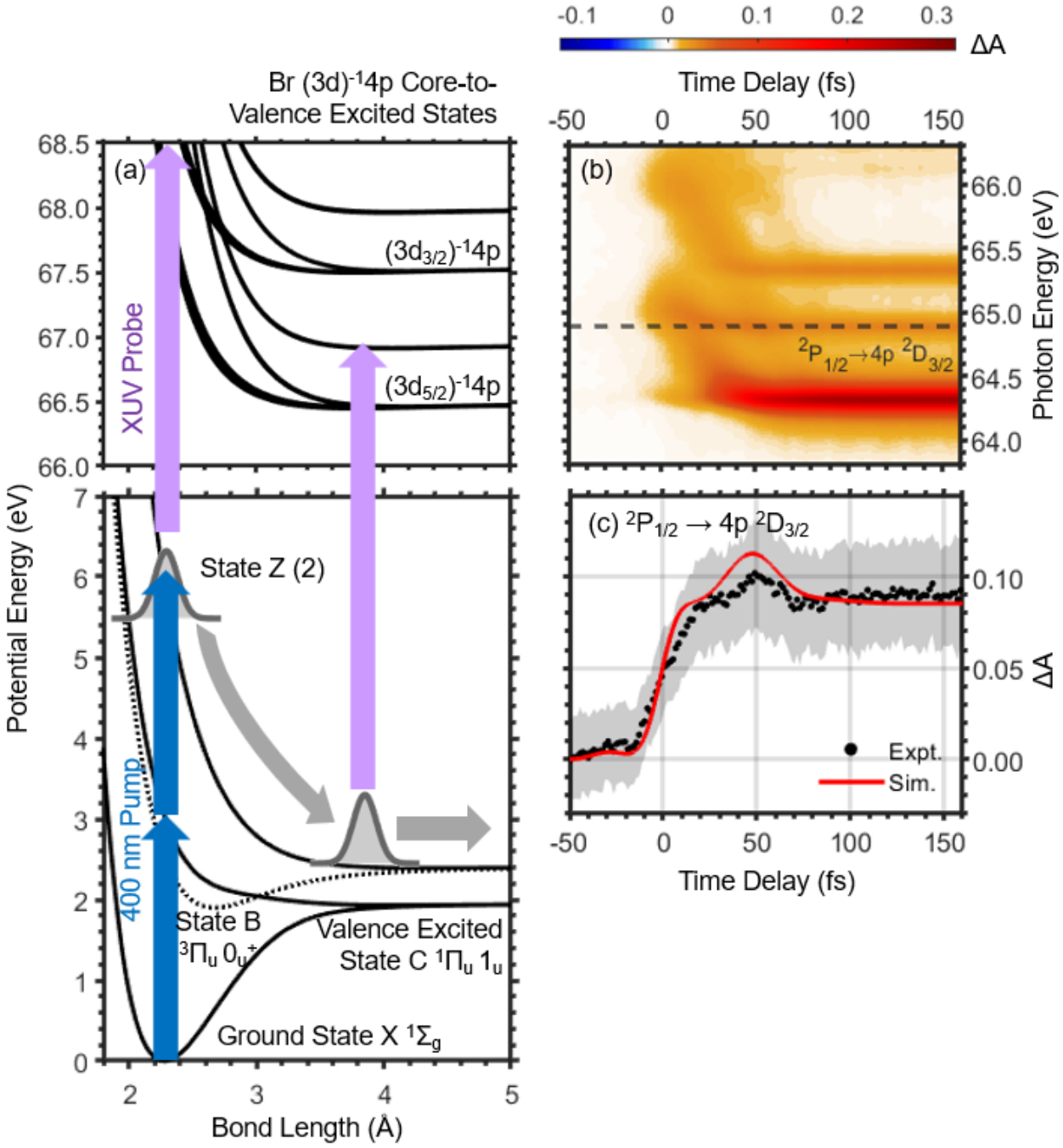

Figure 3.16. (a) Cascade one-photon absorptions of pump pulses from the ground state to the C state, then to the Z state. (b) Experimental time-resolved XUV absorption spectrum. (c) Lineout in time from (b) at 64.89 eV for atomic Br 3d ($^2P_{1/2}$) → 4p ($^2D_{3/2}$) absorption. Black dot and gray shade: the best estimate and the uncertainty of the measured value (mean and standard deviation of 93 measurements of time-resolved spectrum). Red solid line: corresponding lineout of simulated time-resolved spectrum from 90% of C state plus 10% of Z state.

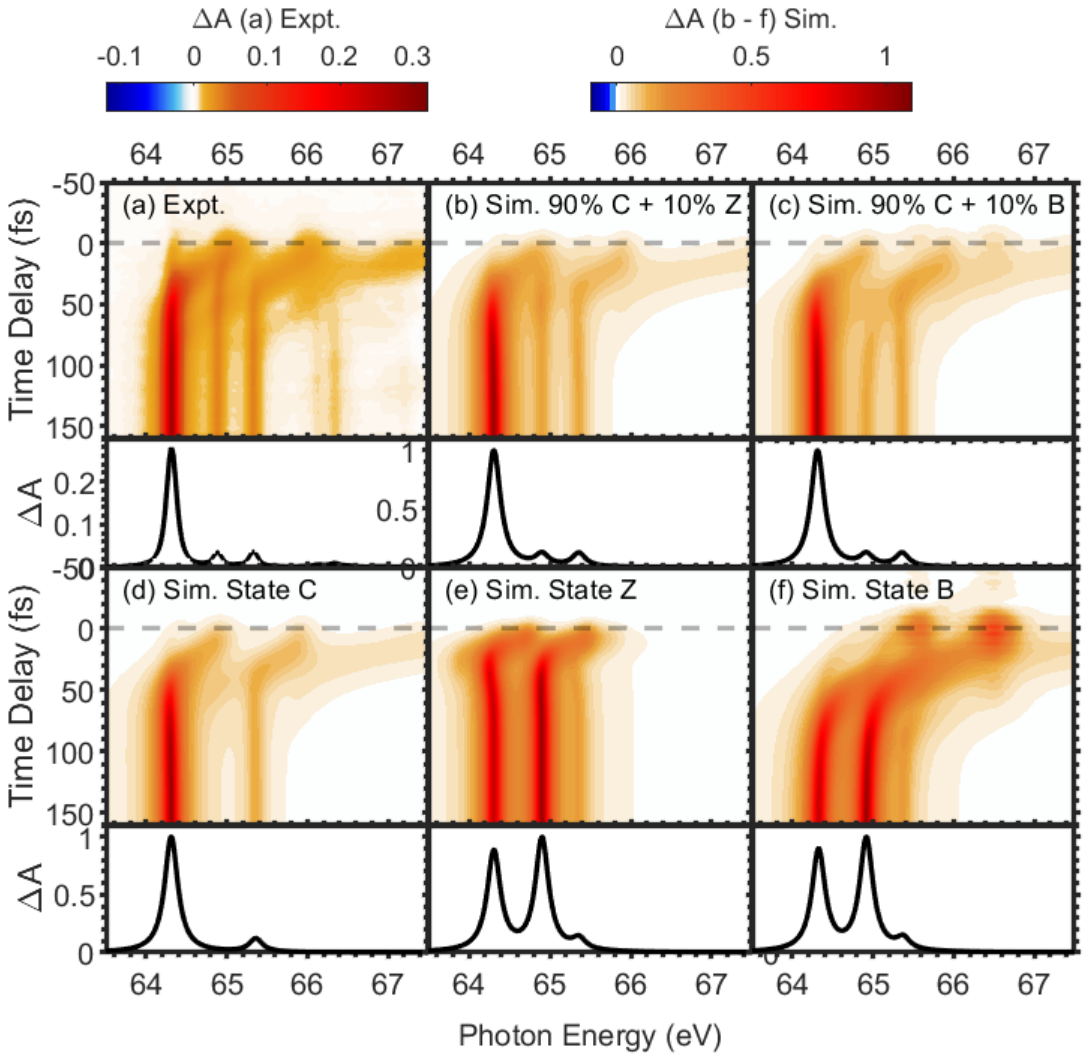

Figure 3.17. (a) Experimental and (b-f) simulated time-resolved XUV absorption spectrum. The lineout at long time delays indicates the branching ratio Br ($^2P_{3/2}$):Br* ($^2P_{1/2}$). The simulated spectrum from 90% of C state plus 10% of Z state (b) best agrees with the experiment (a).

3.7.4 Ground State Bleaching: Coherent Vibrational Dynamics in the Electronic Ground State

The ground state bleaching signal of the $3d_{5/2,3/2} \rightarrow 4p\sigma^*$ doublet oscillates in time around the equilibrium absorption energy E_{eq} 68.10 and 69.13 eV, respectively (Figure 3.18(b)). These signals encode the dynamics of the coherent vibrational wavepacket in the electronic ground state of Br_2 molecules,[25] which is elaborated in Figure 3.18 with relevant potential energy curves. The coherent vibrational wavepacket in the electronic ground state is launched by the 400 nm pump pulse via resonant impulsive stimulated Raman scattering (ISRS).[40,42,43,5] Then, the motion of the vibrational wavepacket is recorded in the time-

resolved absorption spectrum of XUV probe pulses (Figure 3.18(b)). The valley (minimum) of the differential absorption signal $\Delta A(E, t)$ oscillates around the equilibrium absorption energy E_{eq} with the vibrational period (Figure 3.18(b)).

On the other hand, since $\Delta A(E, t)$ signal crosses the E_{eq} two times per cycle, its lineout in time at E_{eq}, $\Delta A(E = E_{eq}, t)$, oscillates at *half* of the vibrational period (Figure 3.18(d, c)). Qualitatively, the lineout $\Delta A(E = E_{eq}, t)$ has two components. One is a decay due to the ground state bleaching. The other is a modulation with oscillation due to the vibration. Quantitatively, the signals are fitted to

$$\begin{aligned} \Delta A(E = E_{\mathrm{eq}}, t) &= \Phi(t) \times \left\{ D_1 + D_2 \sin^2 \left(\frac{2\pi t}{T_{\mathrm{vib}}} + \phi \right) \right\} \\ &= \Phi(t) \times \left\{ \left(D_1 + \frac{D_2}{2} \right) - \frac{D_2}{2} \cos \left(\frac{2\pi t}{T_{\mathrm{vib}}/2} + \phi \right) \right\} \end{aligned} \tag{13}$$

by the identity $\sin^2 \theta = (1 - \cos 2\theta)/2$ and the apparent period of this lineout is *half* of the vibrational period. Here $D_1 < 0$ and $D_2 < 0$ are the fitting parameters, $\Phi(t)$ is the cumulative distribution function of the pump pulse shape $f(t)$ (measured temporal intensity envelope from SD-FROG in Figure 3.13(d)), defined as

$$\Phi(t) = \int_{-\infty}^{t} f(t')dt' \tag{14}$$

and T_{vib} and ϕ are the period and phase of the sine function. The fitted period T_{vib} is 107 ± 5 and 105 ± 7 fs for the $3d_{5/2,3/2} \rightarrow 4p\sigma^*$ transitions, respectively, and agrees with the 102 fs (325.321 cm^{-1})[91] fundamental vibrational period of Br_2. Here the best estimate ± uncertainty of the measured values is reported as the mean ± one standard deviation[88] of fitted values to each of the 93 measurements.

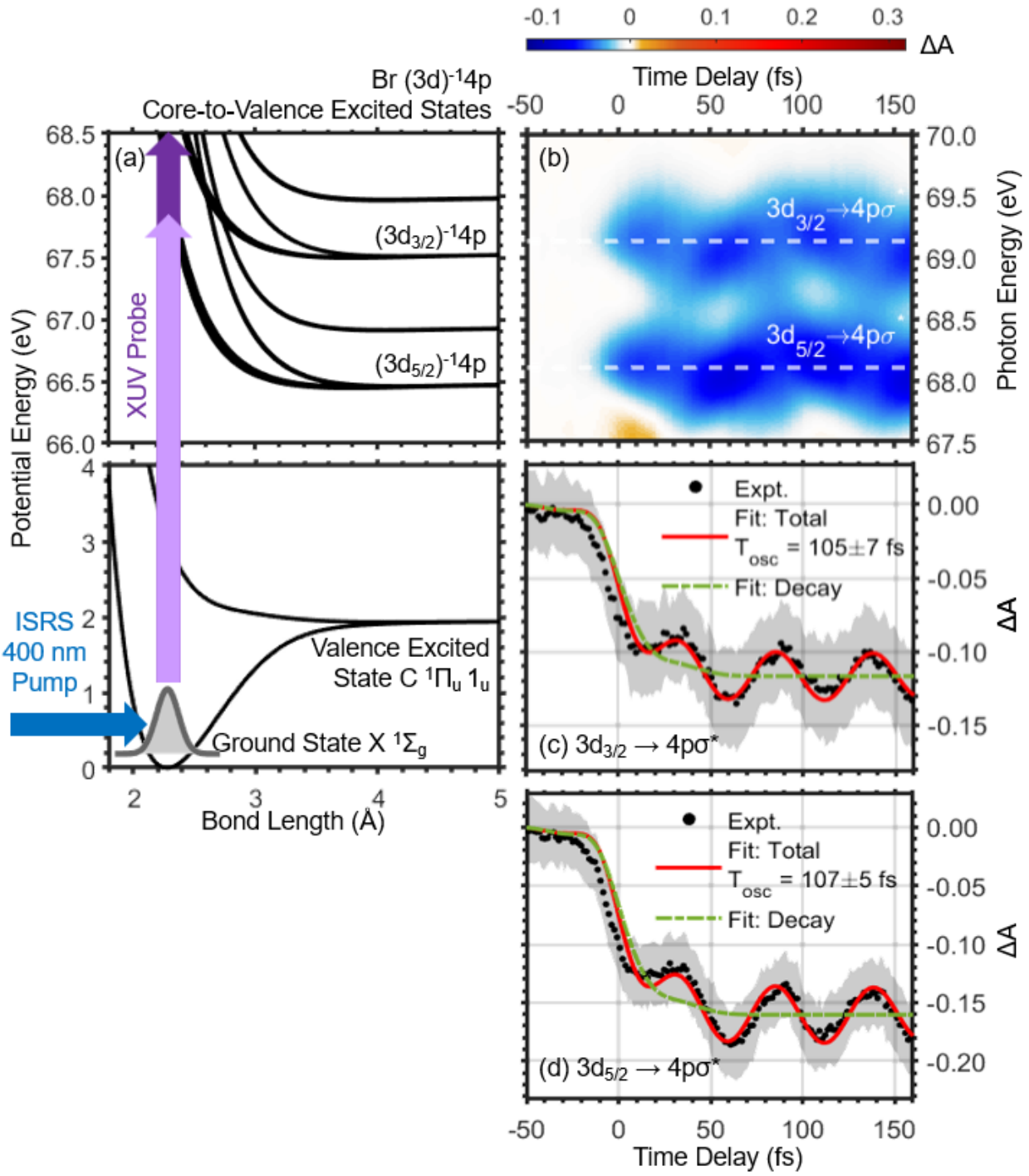

Figure 3.18. Coherent vibrational dynamics in the ground state of Br_2 molecule. (a) Potential energy curves of the relevant electronic states. (b) Time-resolved XUV differential absorption spectrum records the vibration and the ground state bleaching. (d, c) Lineout in time at the equilibrium absorption energy (E_{eq}) 68.10 eV and 69.13 eV for the $3d_{5/2,3/2} \rightarrow 4p\sigma^*$ absorption of Br_2 molecules. Black open circle and gray shade: the best estimate and uncertainty of measured ΔA values (mean and one standard deviation[88] of the 93 measurements). Red solid line: total fit by Equation 13. Green dash-dot line: decay part of the

fit as $\Phi(t) \times (D_1 + D_2/2)$. The apparent period of the lineout at E_{eq} is *half* of the vibrational period, as explained with the fit formula.

3.7.5 The Relative Polarization of 400 nm Pump and XUV Probe Pulses and its Potential Implications

In the presented experiments, the 400 nm pump and XUV probe have horizontal and vertical polarizations, respectively. That is, their relative polarization is perpendicular. Besides, the gas-phase bromines are initially oriented to random directions. The 400 nm pump pulse will selectively access the perpendicular transition of the molecule, corresponding to the $X\ ^1\Sigma_g^+ \rightarrow C\ ^1\Pi_u\ 1_u$ transition. Meanwhile, the XUV probe pulse can access both the parallel and perpendicular transitions from the $C\ ^1\Pi_u\ 1_u$ state to various core excited states, as the Br-3d core orbital retains atom-like isotropic nature and all Ω states exist in its degeneracy manifold. As a result, the XUV pump-probe signals can return robust results for the dissociation times, either parallel or perpendicular-polarized configuration is used. The precise influence, however, has not been investigated in this study. In addition, polarization dependence within the fine structures of the 3d → *n*s, *n*p core-to-Rydberg series might exhibit different XUV absorption strengths. This has been well documented in the literature with rare-gas atoms.[119]

4 Conclusions and Prospect

In this dissertation, I investigated ultrafast nuclear dynamics in several molecules via Extreme Ultraviolet (XUV)-Attosecond Transient Absorption Spectroscopy (ATAS). The studies encompass two representative systems, the coherent vibrational dynamics of CBr4 in the electronic ground state. The dissociation dynamics of Br_2 in the electronic excited C state.

For the coherent vibrations in CBr_4 with the knowledge of calculated potential energy curve, XUV-ATAS is capable of resolving tiny bond length displacements on the order of 10^{-4} Å with 26 fs temporal resolution. Such spatial and temporal resolution is remarkable. For instance, one common technique to study nuclear or structural dynamics is ultrafast electron diffraction (UED). For the state-of-the-art MeV-Ultrafast Electron Diffraction (MeV-UED) at SLAC, its spatial resolution is 0.63 Å and temporal resolution is about 150 fs. Compared to MeV-UED, XUV-ATAS has a spatial resolution about 1000 times better and a temporal resolution 5 times better.

For the dissociation in Br_2, the measured rise time is different for the probed final state: 38 ± 1 and 20 ± 5 fs for Br 3d $^2P_{3/2} \rightarrow$ 4p $^2D_{5/2}$ and $^2D_{3/2}$ at 64.31 and 65.34 eV, respectively. Together with nuclear TDSE simulations, the results show that the measured probe signals accurately contain the dissociative wavepacket dynamics but also reveal how the different probe transitions change toward dissociation with bond length. This work points out the probe-transition-dependent effects that need to be considered when interpreting measured signals and their timescales. Furthermore, in the literature, the static Br 3d core-to-valence and core-to-Rydberg spectra were reported separately for Br_2 molecules or Br atoms. These individual measurements were bridged together in the presented broadband time-resolved spectra, showing a full evolution from molecules to atoms. This unification shows the unique strength of time-resolved absorption spectroscopy with broadband XUV light.

While attosecond optics originates from atomic physics, this dissertation successfully demonstrates the great capability of XUV-ATAS to investigate molecules, with extraordinary spatial and temporal resolution. Furthermore, one unique strength of core-level absorption with XUV light is its ability to distinguish different elements via their characteristic absorption edges. Such element specificity is backed by the abundant literature of the X-ray spectroscopy. The results have shown this for small or simple systems with few types of elements. Furthermore, this capability will be even more powerful when the system is more complicated and more elements are involved. This will be a bright opportunity for ATAS.

In prospect, the charge-transfer curve-crossing in alkali halides like NaI will be an excellent example for this.[120] First, both the Na-2p (~30 eV) and I-5p (~50 eV) absorption edges can be observed at the same time, with the broadband XUV pulse. Second, the change in oxidation state can be clearly identified with the blueshift of Na-2p (~30 eV) to Na^+-2p (~33 eV), and the alternation of the appearance of the I-5p (~50 eV) and the disappearance of I^--5p signals. Third, the change in electronic state thru the crossing point will be resolved with fine temporal resolution. In the future, this study will be a great advancement and reveal a panoramic picture on curve-crossing charge-transfer in alkali halides.

References

(1) Weiner, A. M. *Ultrafast Optics*, 1st ed.; Wiley, 2009. https://doi.org/10.1002/9780470473467.

(2) Dantus, M.; Rosker, M. J.; Zewail, A. H. Real-Time Femtosecond Probing of "'Transition States"' in Chemical Reactions. *J. Chem. Phys.* **1987**, *87* (4), 2395–2397. https://doi.org/10.1063/1.453122.

(3) Polli, D.; Altoè, P.; Weingart, O.; Spillane, K. M.; Manzoni, C.; Brida, D.; Tomasello, G.; Orlandi, G.; Kukura, P.; Mathies, R. A.; Garavelli, M.; Cerullo, G. Conical Intersection Dynamics of the Primary Photoisomerization Event in Vision. *Nature* **2010**, *467* (7314), 440–443. https://doi.org/10.1038/nature09346.

(4) Ridente, E.; Hait, D.; Haugen, E. A.; Ross, A. D.; Neumark, D. M.; Head-Gordon, M.; Leone, S. R. Femtosecond Symmetry Breaking and Coherent Relaxation of Methane Cations via X-Ray Spectroscopy. *Science* **2023**, *380* (6646), 713–717. https://doi.org/10.1126/science.adg4421.

(5) Ou, J.-H.; Hait, D.; Rupprecht, P.; Beetar, J. E.; Martínez, T. J.; Leone, S. R. Attosecond Probing of Coherent Vibrational Dynamics in CBr_4. *J. Phys. Chem. A* **2024**, *128* (42), 9208–9217. https://doi.org/10.1021/acs.jpca.4c05210.

(6) Beetar, J. E.; Ou, J.-H.; Kobayashi, Y.; Leone, S. R. Different Rise Times of Atomic Br $M_{4,5}$ $3d_{3/2,5/2}$ Core Level Absorptions during Br_2 C $^1\Pi_u$ 1_u State Dissociation via Extreme Ultraviolet Transient Absorption Spectroscopy. *J. Phys. Chem. A* **2025**, acs.jpca.5c06776. https://doi.org/10.1021/acs.jpca.5c06776.

(7) Dantus, M.; Rosker, M. J.; Zewail, A. H. Femtosecond Real-Time Probing of Reactions. II. The Dissociation Reaction of ICN. *J. Chem. Phys.* **1988**, *89* (10), 6128–6140. https://doi.org/10.1063/1.455428.

(8) Zewail, A. H. Femtochemistry: Atomic-Scale Dynamics of the Chemical Bond. *J. Phys. Chem. A* **2000**, *104* (24), 5660–5694. https://doi.org/10.1021/jp001460h.

(9) Rosker, M. J.; Dantus, M.; Zewail, A. H. Femtosecond Real-Time Probing of Reactions. I. The Technique. *J. Chem. Phys.* **1988**, *89* (10), 6113–6127. https://doi.org/10.1063/1.455427.

(10) Hentschel, M.; Kienberger, R.; Spielmann, Ch.; Reider, G. A.; Milosevic, N.; Brabec, T.; Corkum, P.; Heinzmann, U.; Drescher, M.; Krausz, F. Attosecond Metrology. *Nature* **2001**, *414* (6863), 509–513. https://doi.org/10.1038/35107000.

(11) Paul, P. M.; Toma, E. S.; Breger, P.; Mullot, G.; Augé, F.; Balcou, Ph.; Muller, H. G.; Agostini, P. Observation of a Train of Attosecond Pulses from High Harmonic Generation. *Science* **2001**, *292* (5522), 1689–1692. https://doi.org/10.1126/science.1059413.

(12) Attwood, D.; Sakdinawat, A. *X-Rays and Extreme Ultraviolet Radiation: Principles and Applications*, 2nd ed.; Cambridge University Press, 2016. https://doi.org/10.1017/CBO9781107477629.

(13) Bressler, C.; Chergui, M. Ultrafast X-Ray Absorption Spectroscopy. *Chem Rev* **2004**, *104* (4), 1781–1812. https://doi.org/10.1021/cr0206667.

(14) Goulielmakis, E.; Loh, Z.-H.; Wirth, A.; Santra, R.; Rohringer, N.; Yakovlev, V. S.; Zherebtsov, S.; Pfeifer, T.; Azzeer, A. M.; Kling, M. F.; Leone, S. R.; Krausz, F. Real-Time Observation of

Valence Electron Motion. *Nature* **2010**, *466* (7307), 739–743. https://doi.org/10.1038/nature09212.

(15) Loh, Z.-H.; Leone, S. R. Capturing Ultrafast Quantum Dynamics with Femtosecond and Attosecond X-Ray Core-Level Absorption Spectroscopy. *J. Phys. Chem. Lett.* **2013**, *4* (2), 292–302. https://doi.org/10.1021/jz301910n.

(16) Leone, S. R.; McCurdy, C. W.; Burgdörfer, J.; Cederbaum, L. S.; Chang, Z.; Dudovich, N.; Feist, J.; Greene, C. H.; Ivanov, M.; Kienberger, R.; Keller, U.; Kling, M. F.; Loh, Z.-H.; Pfeifer, T.; Pfeiffer, A. N.; Santra, R.; Schafer, K.; Stolow, A.; Thumm, U.; Vrakking, M. J. J. What Will It Take to Observe Processes in "Real Time"? *Nat. Photonics* **2014**, *8* (3), 162–166. https://doi.org/10.1038/nphoton.2014.48.

(17) Geneaux, R.; Marroux, H. J. B.; Guggenmos, A.; Neumark, D. M.; Leone, S. R. Transient Absorption Spectroscopy Using High Harmonic Generation: A Review of Ultrafast X-Ray Dynamics in Molecules and Solids. *Philos. Trans. R. Soc. Math. Phys. Eng. Sci.* **2019**, *377* (2145), 20170463. https://doi.org/10.1098/rsta.2017.0463.

(18) Kobayashi, Y.; Leone, S. R. Characterizing Coherences in Chemical Dynamics with Attosecond Time-Resolved x-Ray Absorption Spectroscopy. *J. Chem. Phys.* **2022**, *157* (18), 180901. https://doi.org/10.1063/5.0119942.

(19) Zong, A.; Nebgen, B. R.; Lin, S.-C.; Spies, J. A.; Zuerch, M. Emerging Ultrafast Techniques for Studying Quantum Materials. *Nat. Rev. Mater.* **2023**, *8* (4), 224–240. https://doi.org/10.1038/s41578-022-00530-0.

(20) Ohmori, K. Wave-Packet and Coherent Control Dynamics. *Annu. Rev. Phys. Chem.* **2009**, *60* (1), 487–511. https://doi.org/10.1146/annurev.physchem.59.032607.093818.

(21) Townsend, D.; Sussman, B. J.; Stolow, A. A Stark Future for Quantum Control. *J. Phys. Chem. A* **2011**, *115* (4), 357–373. https://doi.org/10.1021/jp109095d.

(22) Yan, Y. X.; Gamble, E. B.; Nelson, K. A. Impulsive Stimulated Scattering: General Importance in Femtosecond Laser Pulse Interactions with Matter, and Spectroscopic Applications. *J. Chem. Phys.* **1985**, *83* (11), 5391–5399. https://doi.org/10.1063/1.449708.

(23) Ruhman, S.; Joly, A. G.; Nelson, K. A. Coherent Molecular Vibrational Motion Observed in the Time Domain Through Impulsive Stimulated Raman Scattering. *IEEE J. Quantum Electron* **1988**, *24* (2), 460–469. https://doi.org/10.1109/3.146.

(24) Dhar, L.; Rogers, J. A.; Nelson, K. A. Time-Resolved Vibrational Spectroscopy in the Impulsive Limit. *Chem Rev* **1994**, *94* (1), 157–193. https://doi.org/10.1021/cr00025a006.

(25) Hosler, E. R.; Leone, S. R. Characterization of Vibrational Wave Packets by Core-Level High-Harmonic Transient Absorption Spectroscopy. *Phys. Rev. A* **2013**, *88* (2), 023420. https://doi.org/10.1103/physreva.88.023420.

(26) Pertot, Y.; Schmidt, C.; Matthews, M.; Chauvet, A.; Huppert, M.; Svoboda, V.; Von Conta, A.; Tehlar, A.; Baykusheva, D.; Wolf, J.-P.; Wörner, H. J. Time-Resolved x-Ray Absorption Spectroscopy with a Water Window High-Harmonic Source. *Science* **2017**, *355* (6322), 264–267. https://doi.org/10.1126/science.aah6114.

(27) Warrick, E. R.; Bækhøj, J. E.; Cao, W.; Fidler, A. P.; Jensen, F.; Madsen, L. B.; Leone, S. R.; Neumark, D. M. Attosecond Transient Absorption Spectroscopy of Molecular Nitrogen:

Vibrational Coherences in the b′ $^1\Sigma_u^+$ State. *Chem. Phys. Lett.* **2017**, *683*, 408–415. https://doi.org/10.1016/j.cplett.2017.02.013.

(28) Wei, Z.; Li, J.; Wang, L.; See, S. T.; Jhon, M. H.; Zhang, Y.; Shi, F.; Yang, M.; Loh, Z.-H. Elucidating the Origins of Multimode Vibrational Coherences of Polyatomic Molecules Induced by Intense Laser Fields. *Nat. Commun.* **2017**, *8* (1), 735. https://doi.org/10.1038/s41467-017-00848-2.

(29) Wei, Z.; Tian, L.; Li, J.; Lu, Y.; Yang, M.; Loh, Z. H. Tracking Ultrafast Bond Dissociation Dynamics at 0.1 Å Resolution by Femtosecond Extreme Ultraviolet Absorption Spectroscopy. *J. Phys. Chem. Lett.* **2018**, *9* (19), 5742–5747. https://doi.org/10.1021/acs.jpclett.8b02547.

(30) Wei, Z.; Li, J.; Zhang, H.; Lu, Y.; Yang, M.; Loh, Z.-H. Ultrafast Dissociative Ionization and Large-Amplitude Vibrational Wave Packet Dynamics of Strong-Field-Ionized Di-Iodomethane. *J. Chem. Phys.* **2019**, *151* (21), 214308. https://doi.org/10.1063/1.5132967.

(31) Saito, N.; Sannohe, H.; Ishii, N.; Kanai, T.; Kosugi, N.; Wu, Y.; Chew, A.; Han, S.; Chang, Z.; Itatani, J. Real-Time Observation of Electronic, Vibrational, and Rotational Dynamics in Nitric Oxide with Attosecond Soft x-Ray Pulses at 400 eV. *Optica* **2019**, *6* (12), 1542. https://doi.org/10.1364/OPTICA.6.001542.

(32) Timmers, H.; Zhu, X.; Li, Z.; Kobayashi, Y.; Sabbar, M.; Hollstein, M.; Reduzzi, M.; Martínez, T. J.; Neumark, D. M.; Leone, S. R. Disentangling Conical Intersection and Coherent Molecular Dynamics in Methyl Bromide with Attosecond Transient Absorption Spectroscopy. *Nat. Commun.* **2019**, *10* (1), 3133. https://doi.org/10.1038/s41467-019-10789-7.

(33) Kobayashi, Y.; Neumark, D. M.; Leone, S. R. Attosecond XUV Probing of Vibronic Quantum Superpositions in Br_2^+. *Phys Rev A* **2020**, *102* (5), 051102. https://doi.org/10.1103/PhysRevA.102.051102.

(34) Kobayashi, Y.; Chang, K. F.; Poullain, S. M.; Scutelnic, V.; Zeng, T.; Neumark, D. M.; Leone, S. R. Coherent Electronic-Vibrational Dynamics in Deuterium Bromide Probed via Attosecond Transient-Absorption Spectroscopy. *Phys Rev A* **2020**, *101* (6), 063414. https://doi.org/10.1103/PhysRevA.101.063414.

(35) Zinchenko, K. S.; Ardana-Lamas, F.; Seidu, I.; Neville, S. P.; Van Der Veen, J.; Lanfaloni, V. U.; Schuurman, M. S.; Wörner, H. J. Sub-7-Femtosecond Conical-Intersection Dynamics Probed at the Carbon K-Edge. *Science* **2021**, *371* (6528), 489–494. https://doi.org/10.1126/science.abf1656.

(36) Rott, F.; Reduzzi, M.; Schnappinger, T.; Kobayashi, Y.; Chang, K. F.; Timmers, H.; Neumark, D. M.; de Vivie-Riedle, R.; Leone, S. R. Ultrafast Strong-Field Dissociation of Vinyl Bromide: An Attosecond Transient Absorption Spectroscopy and Non-Adiabatic Molecular Dynamics Study. *Struct Dyn* **2021**, *8* (3), 034104. https://doi.org/10.1063/4.0000102.

(37) Loh, Z.-H. Studies of Ultrafast Molecular Dynamics by Femtosecond Extreme Ultraviolet Absorption Spectroscopy. *Chem. Lett.* **2021**, *50* (5), 965–973. https://doi.org/10.1246/cl.200940.

(38) Poullain, S. M.; Kobayashi, Y.; Chang, K. F.; Leone, S. R. Visualizing Coherent Vibrational Motion in the Molecular Iodine B $^3\Pi_{0+u}$ State Using Ultrafast XUV Transient-Absorption

Spectroscopy. *Phys. Rev. A* **2021**, *104* (2), 022817. https://doi.org/10.1103/PhysRevA.104.022817.

(39) Chang, K. F.; Wang, H.; Poullain, S. M.; Prendergast, D.; Neumark, D. M.; Leone, S. R. Mapping Wave Packet Bifurcation at a Conical Intersection in CH_3I by Attosecond XUV Transient Absorption Spectroscopy. *J. Chem. Phys.* **2021**, *154* (23), 234301. https://doi.org/10.1063/5.0056299.

(40) Chang, K. F.; Wang, H.; Poullain, S. M.; González-Vázquez, J.; Bañares, L.; Prendergast, D.; Neumark, D. M.; Leone, S. R. Conical Intersection and Coherent Vibrational Dynamics in Alkyl Iodides Captured by Attosecond Transient Absorption Spectroscopy. *J. Chem. Phys.* **2022**, *156* (11), 114304. https://doi.org/10.1063/5.0086775.

(41) Matselyukh, D. T.; Despré, V.; Golubev, N. V.; Kuleff, A. I.; Wörner, H. J. Decoherence and Revival in Attosecond Charge Migration Driven by Non-Adiabatic Dynamics. *Nat. Phys.* **2022**, *18* (10), 1206–1213. https://doi.org/10.1038/s41567-022-01690-0.

(42) Rupprecht, P.; Aufleger, L.; Heinze, S.; Magunia, A.; Ding, T.; Rebholz, M.; Amberg, S.; Mollov, N.; Henrich, F.; Haverkort, M. W.; Ott, C.; Pfeifer, T. Resolving Vibrations in a Polyatomic Molecule with Femtometer Precision via X-Ray Spectroscopy. *Phys. Rev. A* **2023**, *108* (3), 032816. https://doi.org/10.1103/physreva.108.032816.

(43) Barreau, L.; Ross, A. D.; Kimberg, V.; Krasnov, P.; Blinov, S.; Neumark, D. M.; Leone, S. R. Core-Excited States of SF_6 Probed with Soft-x-Ray Femtosecond Transient Absorption of Vibrational Wave Packets. *Phys. Rev. A* **2023**, *108* (1), 012805. https://doi.org/10.1103/physreva.108.012805.

(44) Ross, A. D.; Hait, D.; Scutelnic, V.; Neumark, D. M.; Head-Gordon, M.; Leone, S. R. Measurement of Coherent Vibrational Dynamics with X-Ray Transient Absorption Spectroscopy Simultaneously at the Carbon K- and Chlorine $L_{2,3}$- Edges. *Commun. Phys.* **2024**, *7*, 304. https://doi.org/10.1038/s42005-024-01794-4.

(45) Frank, I.; Hutter, J.; Marx, D.; Parrinello, M. Molecular Dynamics in Low-Spin Excited States. *J. Chem. Phys.* **1998**, *108* (10), 4060–4069. https://doi.org/10.1063/1.475804.

(46) Kowalczyk, T.; Tsuchimochi, T.; Chen, P.-T.; Top, L.; Van Voorhis, T. Excitation Energies and Stokes Shifts from a Restricted Open-Shell Kohn-Sham Approach. *J. Chem. Phys.* **2013**, *138* (16), 164101. https://doi.org/10.1063/1.4801790.

(47) Hait, D.; Head-Gordon, M. Highly Accurate Prediction of Core Spectra of Molecules at Density Functional Theory Cost: Attaining Sub-Electronvolt Error from a Restricted Open-Shell Kohn–Sham Approach. *J. Phys. Chem. Lett.* **2020**, *11* (3), 775–786. https://doi.org/10.1021/acs.jpclett.9b03661.

(48) Epifanovsky, E.; Gilbert, A. T. B.; Feng, X.; Lee, J.; Mao, Y.; Mardirossian, N.; Pokhilko, P.; White, A. F.; Coons, M. P.; Dempwolff, A. L.; Gan, Z.; Hait, D.; Horn, P. R.; Jacobson, L. D.; Kaliman, I.; Kussmann, J.; Lange, A. W.; Lao, K. U.; Levine, D. S.; Liu, J.; McKenzie, S. C.; Morrison, A. F.; Nanda, K. D.; Plasser, F.; Rehn, D. R.; Vidal, M. L.; You, Z.-Q.; Zhu, Y.; Alam, B.; Albrecht, B. J.; Aldossary, A.; Alguire, E.; Andersen, J. H.; Athavale, V.; Barton, D.; Begam, K.; Behn, A.; Bellonzi, N.; Bernard, Y. A.; Berquist, E. J.; Burton, H. G. A.; Carreras, A.; Carter-Fenk, K.; Chakraborty, R.; Chien, A. D.; Closser, K. D.; Cofer-Shabica, V.; Dasgupta, S.; De Wergifosse,

M.; Deng, J.; Diedenhofen, M.; Do, H.; Ehlert, S.; Fang, P.-T.; Fatehi, S.; Feng, Q.; Friedhoff, T.; Gayvert, J.; Ge, Q.; Gidofalvi, G.; Goldey, M.; Gomes, J.; González-Espinoza, C. E.; Gulania, S.; Gunina, A. O.; Hanson-Heine, M. W. D.; Harbach, P. H. P.; Hauser, A.; Herbst, M. F.; Hernández Vera, M.; Hodecker, M.; Holden, Z. C.; Houck, S.; Huang, X.; Hui, K.; Huynh, B. C.; Ivanov, M.; Jász, Á.; Ji, H.; Jiang, H.; Kaduk, B.; Kähler, S.; Khistyaev, K.; Kim, J.; Kis, G.; Klunzinger, P.; Koczor-Benda, Z.; Koh, J. H.; Kosenkov, D.; Koulias, L.; Kowalczyk, T.; Krauter, C. M.; Kue, K.; Kunitsa, A.; Kus, T.; Ladjánszki, I.; Landau, A.; Lawler, K. V.; Lefrancois, D.; Lehtola, S.; Li, R. R.; Li, Y.-P.; Liang, J.; Liebenthal, M.; Lin, H.-H.; Lin, Y.-S.; Liu, F.; Liu, K.-Y.; Loipersberger, M.; Luenser, A.; Manjanath, A.; Manohar, P.; Mansoor, E.; Manzer, S. F.; Mao, S.-P.; Marenich, A. V.; Markovich, T.; Mason, S.; Maurer, S. A.; McLaughlin, P. F.; Menger, M. F. S. J.; Mewes, J.-M.; Mewes, S. A.; Morgante, P.; Mullinax, J. W.; Oosterbaan, K. J.; Paran, G.; Paul, A. C.; Paul, S. K.; Pavošević, F.; Pei, Z.; Prager, S.; Proynov, E. I.; Rák, Á.; Ramos-Cordoba, E.; Rana, B.; Rask, A. E.; Rettig, A.; Richard, R. M.; Rob, F.; Rossomme, E.; Scheele, T.; Scheurer, M.; Schneider, M.; Sergueev, N.; Sharada, S. M.; Skomorowski, W.; Small, D. W.; Stein, C. J.; Su, Y.-C.; Sundstrom, E. J.; Tao, Z.; Thirman, J.; Tornai, G. J.; Tsuchimochi, T.; Tubman, N. M.; Veccham, S. P.; Vydrov, O.; Wenzel, J.; Witte, J.; Yamada, A.; Yao, K.; Yeganeh, S.; Yost, S. R.; Zech, A.; Zhang, I. Y.; Zhang, X.; Zhang, Y.; Zuev, D.; Aspuru-Guzik, A.; Bell, A. T.; Besley, N. A.; Bravaya, K. B.; Brooks, B. R.; Casanova, D.; Chai, J.-D.; Coriani, S.; Cramer, C. J.; Cserey, G.; DePrince, A. E.; DiStasio, R. A.; Dreuw, A.; Dunietz, B. D.; Furlani, T. R.; Goddard, W. A.; Hammes-Schiffer, S.; Head-Gordon, T.; Hehre, W. J.; Hsu, C.-P.; Jagau, T.-C.; Jung, Y.; Klamt, A.; Kong, J.; Lambrecht, D. S.; Liang, W.; Mayhall, N. J.; McCurdy, C. W.; Neaton, J. B.; Ochsenfeld, C.; Parkhill, J. A.; Peverati, R.; Rassolov, V. A.; Shao, Y.; Slipchenko, L. V.; Stauch, T.; Steele, R. P.; Subotnik, J. E.; Thom, A. J. W.; Tkatchenko, A.; Truhlar, D. G.; Van Voorhis, T.; Wesolowski, T. A.; Whaley, K. B.; Woodcock, H. L.; Zimmerman, P. M.; Faraji, S.; Gill, P. M. W.; Head-Gordon, M.; Herbert, J. M.; Krylov, A. I. Software for the Frontiers of Quantum Chemistry: An Overview of Developments in the Q-Chem 5 Package. *J. Chem. Phys.* **2021**, *155* (8), 084801. https://doi.org/10.1063/5.0055522.

(49) Hui, K.; Chai, J.-D. SCAN-Based Hybrid and Double-Hybrid Density Functionals from Models without Fitted Parameters. *J. Chem. Phys.* **2016**, *144* (4), 044114. https://doi.org/10.1063/1.4940734.

(50) Dunning, T. H. Gaussian Basis Sets for Use in Correlated Molecular Calculations. I. The Atoms Boron through Neon and Hydrogen. *J. Chem. Phys.* **1989**, *90* (2), 1007–1023. https://doi.org/10.1063/1.456153.

(51) Kendall, R. A.; Dunning, T. H.; Harrison, R. J. Electron Affinities of the First-Row Atoms Revisited. Systematic Basis Sets and Wave Functions. *J. Chem. Phys.* **1992**, *96* (9), 6796–6806. https://doi.org/10.1063/1.462569.

(52) Wilson, A. K.; Woon, D. E.; Peterson, K. A.; Dunning, T. H. Gaussian Basis Sets for Use in Correlated Molecular Calculations. IX. The Atoms Gallium through Krypton. *J. Chem. Phys.* **1999**, *110* (16), 7667–7676. https://doi.org/10.1063/1.478678.

(53) Dyall, K. G. Interfacing Relativistic and Nonrelativistic Methods. I. Normalized Elimination of the Small Component in the Modified Dirac Equation. *J. Chem. Phys.* **1997**, *106* (23), 9618–9626. https://doi.org/10.1063/1.473860.

(54) Kutzelnigg, W.; Liu, W. Quasirelativistic Theory Equivalent to Fully Relativistic Theory. *J. Chem. Phys.* **2005**, *123* (24), 241102. https://doi.org/10.1063/1.2137315.

(55) Saue, T. Relativistic Hamiltonians for Chemistry: A Primer. *ChemPhysChem* **2011**, *12* (17), 3077–3094. https://doi.org/10.1002/cphc.201100682.

(56) Cunha, L. A.; Hait, D.; Kang, R.; Mao, Y.; Head-Gordon, M. Relativistic Orbital-Optimized Density Functional Theory for Accurate Core-Level Spectroscopy. *J. Phys. Chem. Lett.* **2022**, *13* (15), 3438–3449. https://doi.org/10.1021/acs.jpclett.2c00578.

(57) Kohn, W.; Sham, L. J. Self-Consistent Equations Including Exchange and Correlation Effects. *Phys. Rev.* **1965**, *140* (4A), A1133–A1138. https://doi.org/10.1103/PhysRev.140.A1133.

(58) Thomassen, H.; Hedberg, K. Distances, Root-Mean-Square Amplitudes of Vibration, and Vibrational Anharmonicity in Carbon Tetrabromide from a Gas-Phase Electron-Diffraction Investigation. *J. Mol. Struct.* **1990**, *240*, 151–157. https://doi.org/10.1016/0022-2860(90)80506-F.

(59) Takehiko Shimanouchi. *Tables of Molecular Vibrational Frequencies Part 1*; National Standard Reference Data Series; National Bureau of Standards, 1967.

(60) Hait, D.; Head-Gordon, M. Orbital Optimized Density Functional Theory for Electronic Excited States. *J. Phys. Chem. Lett.* **2021**, *12* (19), 4517–4529. https://doi.org/10.1021/acs.jpclett.1c00744.

(61) Hait, D.; Head-Gordon, M. Excited State Orbital Optimization via Minimizing the Square of the Gradient: General Approach and Application to Singly and Doubly Excited States via Density Functional Theory. *J. Chem. Theory Comput.* **2020**, *16* (3), 1699–1710. https://doi.org/10.1021/acs.jctc.9b01127.

(62) Boo, B. H.; Saito, N.; Suzuki, I. H.; Koyano, I. Dissociation Processes of Core-Excited CBr_4 Involving the Br(3d, 3p, 3s) and C(1s) Inner-Shells in the Range 50–460 eV. *J. Electron Spectrosc. Relat. Phenom.* **2002**, *123* (1), 73–84. https://doi.org/10.1016/s0368-2048(02)00005-1.

(63) Xu, Z.; Hu, P.; Wang, E.; Xu, S.; Wang, X.; Zhao, Y.; Deng, J.; Ning, C.; Ren, X. Experimental and Theoretical Study of Valence Electronic Structure of Tetrabromomethane by (e, 2e) Electron Momentum Spectroscopy. *Phys. Rev. A* **2019**, *99* (6), 062705. https://doi.org/10.1103/PhysRevA.99.062705.

(64) Krainov, V. P.; Reiss, H. R.; Smirnov, B. M. *Radiative Processes in Atomic Physics*, 1st ed.; Wiley, 1997. https://doi.org/10.1002/3527605606.

(65) Domke, M.; Schulz, K.; Remmers, G.; Kaindl, G.; Wintgen, D. High-Resolution Study of $^1P^o$ Double-Excitation States in Helium. *Phys. Rev. A* **1996**, *53* (3), 1424–1438. https://doi.org/10.1103/PhysRevA.53.1424.

(66) Causley, G. C.; Russell, B. R. Vacuum Ultraviolet Absorption Spectra of the Bromomethanes. *J. Chem. Phys.* **1975**, *62* (3), 848–857. https://doi.org/10.1063/1.430535.

(67) Olthoff, J. K.; Moore, J. H.; Tossell, J. A. Electron Attachment by Chloro and Bromomethanes. *J. Chem. Phys.* **1986**, *85* (1), 249–254. https://doi.org/10.1063/1.451644.

(68) Nahon, L.; Morin, P.; Farnoux, F. C. Relaxation of the $nd \rightarrow (n+1)p$ Resonances in Atomic Bromine and Iodine. *Phys. Scr.* **1992**, *T41* (T41), 104–112. https://doi.org/10.1088/0031-8949/1992/T41/017.

(69) Hait, D.; Head-Gordon, M. When Is a Bond Broken? The Polarizability Perspective. *Angew. Chem. Int. Ed.* **2023**, *62* (46), e202312078. https://doi.org/10.1002/anie.202312078.

(70) Hait, D.; Head-Gordon, M. How Accurate Are Static Polarizability Predictions from Density Functional Theory? An Assessment over 132 Species at Equilibrium Geometry. *Phys. Chem. Chem. Phys.* **2018**, *20* (30), 19800–19810. https://doi.org/10.1039/C8CP03569E.

(71) Nugent-Glandorf, L.; Scheer, M.; Samuels, D. A.; Mulhisen, A. M.; Grant, E. R.; Yang, X.; Bierbaum, V. M.; Leone, S. R. Ultrafast Time-Resolved Soft X-Ray Photoelectron Spectroscopy of Dissociating Br_2. *Phys. Rev. Lett.* **2001**, *87* (19), 193002. https://doi.org/10.1103/PhysRevLett.87.193002.

(72) Nugent-Glandorf, L.; Scheer, M.; Samuels, D. A.; Bierbaum, V. M.; Leone, S. R. Ultrafast Photodissociation of Br2: Laser-Generated High-Harmonic Soft x-Ray Probing of the Transient Photoelectron Spectra and Ionization Cross Sections. *J. Chem. Phys.* **2002**, *117* (13), 6108–6116. https://doi.org/10.1063/1.1504084.

(73) Strasser, D.; Goulay, F.; Leone, S. R. Transient Photoelectron Spectroscopy of the Dissociative $Br_2(^1\Pi_u)$ State. *J. Chem. Phys.* **2007**, *127* (18), 184305. https://doi.org/10.1063/1.2803923.

(74) Wernet, Ph.; Odelius, M.; Godehusen, K.; Gaudin, J.; Schwarzkopf, O.; Eberhardt, W. Real-Time Evolution of the Valence Electronic Structure in a Dissociating Molecule. *Phys. Rev. Lett.* **2009**, *103* (1), 013001. https://doi.org/10.1103/PhysRevLett.103.013001.

(75) Wörner, H. J.; Bertrand, J. B.; Kartashov, D. V.; Corkum, P. B.; Villeneuve, D. M. Following a Chemical Reaction Using High-Harmonic Interferometry. *Nature* **2010**, *466* (7306), 604–607. https://doi.org/10.1038/nature09185.

(76) Wörner, H. J.; Bertrand, J. B.; Corkum, P. B.; Villeneuve, D. M. High-Harmonic Homodyne Detection of the Ultrafast Dissociation of Br_2 Molecules. *Phys. Rev. Lett.* **2010**, *105* (10), 103002. https://doi.org/10.1103/PhysRevLett.105.103002.

(77) Li, W.; Jaroń-Becker, A. A.; Hogle, C. W.; Sharma, V.; Zhou, X.; Becker, A.; Kapteyn, H. C.; Murnane, M. M. Visualizing Electron Rearrangement in Space and Time during the Transition from a Molecule to Atoms. *Proc. Natl. Acad. Sci.* **2010**, *107* (47), 20219–20222. https://doi.org/10.1073/pnas.1014723107.

(78) Rouzée, A.; Johnsson, P.; Rading, L.; Hundertmark, A.; Siu, W.; Huismans, Y.; Düsterer, S.; Redlin, H.; Tavella, F.; Stojanovic, N.; Al-Shemmary, A.; Lépine, F.; Holland, D. M. P.; Schlatholter, T.; Hoekstra, R.; Fukuzawa, H.; Ueda, K.; Vrakking, M. J. J. Towards Imaging of Ultrafast Molecular Dynamics Using FELs. *J. Phys. B At. Mol. Opt. Phys.* **2013**, *46* (16), 164029. https://doi.org/10.1088/0953-4075/46/16/164029.

(79) Wernet, P. Electronic Structure in Real Time: Mapping Valence Electron Rearrangements during Chemical Reactions. *Phys. Chem. Chem. Phys.* **2011**, *13* (38), 16941. https://doi.org/10.1039/c0cp02934c.

(80) Shaw, D. A.; Cvejanovic, D.; King, G. C.; Read, F. H. Inner-Shell and Outer-Shell Excitation of HCl, HBr and Br_2 by Electron Impact with High Resolution. *J. Phys. B At. Mol. Phys.* **1984**, *17* (6), 1173–1187. https://doi.org/10.1088/0022-3700/17/6/026.

(81) Mazzoni, M.; Pettini, M. Inner Shell Transitions of Br I in the EUV. *Phys. Lett. A* **1981**, *85* (6–7), 331–333. https://doi.org/10.1016/0375-9601(81)90322-4.

(82) Nahon, L.; Morin, P. Experimental Study of Rydberg States Excited from the *d* Shell of Atomic Bromine and Iodine. *Phys. Rev. A* **1992**, *45* (5), 2887–2893. https://doi.org/10.1103/PhysRevA.45.2887.

(83) Cummings, A.; O'Sullivan, G. Discrete Structure in the 3 *d* Photoabsorption Spectra of Neutral, Singly Ionized and Doubly Ionized Bromine. *Phys. Rev. A* **1996**, *54* (1), 323–334. https://doi.org/10.1103/PhysRevA.54.323.

(84) Johnson, J.; Cutler, J. N.; Bancroft, G. M.; Hu, Y. F.; Tan, K. H. High-Resolution Photoabsorption and Photoelectron Spectra of Bromine-Containing Molecules at the Br 3d Edge: The Importance of Ligand Field Splitting. *J. Phys. B At. Mol. Opt. Phys.* **1997**, *30* (21), 4899–4917. https://doi.org/10.1088/0953-4075/30/21/024.

(85) Schmidt, M. W.; Baldridge, K. K.; Boatz, J. A.; Elbert, S. T.; Gordon, M. S.; Jensen, J. H.; Koseki, S.; Matsunaga, N.; Nguyen, K. A.; Su, S.; Windus, T. L.; Dupuis, M.; Montgomery, J. A. General Atomic and Molecular Electronic Structure System. *J. Comput. Chem.* **1993**, *14* (11), 1347–1363. https://doi.org/10.1002/jcc.540141112.

(86) Lee, S.; Pollard, W. T.; Mathies, R. A. Quasi-Classical Models of Transition State Absorption or Emission. *Chem. Phys. Lett.* **1989**, *163* (1), 11–18. https://doi.org/10.1016/0009-2614(89)80003-X.

(87) Berera, R.; Van Grondelle, R.; Kennis, J. T. M. Ultrafast Transient Absorption Spectroscopy: Principles and Application to Photosynthetic Systems. *Photosynth. Res.* **2009**, *101* (2–3), 105–118. https://doi.org/10.1007/s11120-009-9454-y.

(88) John R. Taylor. *Introduction to Error Analysis: The Study of Uncertainties in Physical Measurements*, 2nd ed.; University Science Books, 1997.

(89) Zewail, A. H. Laser Femtochemistry. *Science* **1988**, *242* (4886), 1645–1653. https://doi.org/10.1126/science.242.4886.1645.

(90) J. A. Coxon. Low-Lying Electronic States of Diatomic Halogen Molecules. In *Molecular Spectroscopy*; R. F. Barrow, D. A. Long, D. J. Millen, Eds.; The Chemical Society, 1973; Vol. 1.

(91) Linstrom, P. NIST Chemistry WebBook, NIST Standard Reference Database 69, 1997. https://doi.org/10.18434/T4D303.

(92) *The IUPAC Compendium of Chemical Terminology: The Gold Book*, 5th ed.; Gold, V., McNaught, A., The International Union of Pure and Applied Chemistry (IUPAC), Eds.; International Union of Pure and Applied Chemistry (IUPAC): Research Triangle Park, NC, 2025. https://doi.org/10.1351/goldbook.

(93) Shen, X.; Nunes, J. P. F.; Yang, J.; Jobe, R. K.; Li, R. K.; Lin, M.-F.; Moore, B.; Niebuhr, M.; Weathersby, S. P.; Wolf, T. J. A.; Yoneda, C.; Guehr, M.; Centurion, M.; Wang, X. J. Femtosecond Gas-Phase Mega-Electron-Volt Ultrafast Electron Diffraction. *Struct. Dyn.* **2019**, *6* (5), 054305. https://doi.org/10.1063/1.5120864.

(94) Filippetto, D.; Musumeci, P.; Li, R. K.; Siwick, B. J.; Otto, M. R.; Centurion, M.; Nunes, J. P. F. Ultrafast Electron Diffraction: Visualizing Dynamic States of Matter. *Rev. Mod. Phys.* **2022**, *94* (4), 045004. https://doi.org/10.1103/RevModPhys.94.045004.

(95) Marroux, H. J. B.; Fidler, A. P.; Ghosh, A.; Kobayashi, Y.; Gokhberg, K.; Kuleff, A. I.; Leone, S. R.; Neumark, D. M. Attosecond Spectroscopy Reveals Alignment Dependent Core-Hole Dynamics in the ICl Molecule. *Nat. Commun.* **2020**, *11* (1), 5810. https://doi.org/10.1038/s41467-020-19496-0.

(96) O'Sullivan, G.; McGuinness, C.; Costello, J. T.; Kennedy, E. T.; Weinmann, B. Trends in 4d-Subshell Photoabsorption along the Iodine Isonuclear Sequence: I, I^+, and I^{2+}. *Phys. Rev. A* **1996**, *53* (5), 3211–3226. https://doi.org/10.1103/PhysRevA.53.3211.

(97) Bressler, C.; Saes, M.; Chergui, M.; Abela, R.; Pattison, P. Optimizing a Time-Resolved X-Ray Absorption Experiment. *Nucl. Instrum. Methods Phys. Res. Sect. Accel. Spectrometers Detect. Assoc. Equip.* **2001**, *467–468*, 1444–1446. https://doi.org/10.1016/S0168-9002(01)00681-7.

(98) Bressler, C.; Saes, M.; Chergui, M.; Grolimund, D.; Abela, R.; Pattison, P. Towards Structural Dynamics in Condensed Chemical Systems Exploiting Ultrafast Time-Resolved x-Ray Absorption Spectroscopy. *J. Chem. Phys.* **2002**, *116* (7), 2955–2966. https://doi.org/10.1063/1.1435618.

(99) Tsai, M.-S.; Liang, A.-Y.; Tsai, C.-L.; Lai, P.-W.; Lin, M.-W.; Chen, M.-C. Nonlinear Compression toward High-Energy Single-Cycle Pulses by Cascaded Focus and Compression. *Sci. Adv.* **2022**, *8* (31), eabo1945. https://doi.org/10.1126/sciadv.abo1945.

(100) Maric, D.; Burrows, J. P.; Moortgat, G. K. A Study of the UV—Visible Absorption Spectra of Br2 and BrCl. *J. Photochem. Photobiol. Chem.* **1994**, *83* (3), 179–192. https://doi.org/10.1016/1010-6030(94)03823-6.

(101) Keller-Rudek, H.; Moortgat, G. K.; Sander, R.; Sörensen, R. The MPI-Mainz UV/VIS Spectral Atlas of Gaseous Molecules of Atmospheric Interest. *Earth Syst. Sci. Data* **2013**, *5* (2), 365–373. https://doi.org/10.5194/essd-5-365-2013.

(102) Géneaux, R.; Chang, H.-T.; Schwartzberg, A. M.; Marroux, H. J. B. Source Noise Suppression in Attosecond Transient Absorption Spectroscopy by Edge-Pixel Referencing. *Opt. Express* **2021**, *29* (2), 951. https://doi.org/10.1364/OE.412117.

(103) Wang, X.; Chini, M.; Cheng, Y.; Wu, Y.; Chang, Z. In Situ Calibration of an Extreme Ultraviolet Spectrometer for Attosecond Transient Absorption Experiments. *Appl. Opt.* **2013**, *52* (3), 323. https://doi.org/10.1364/AO.52.000323.

(104) Nakano, H.; Uchiyama, R.; Hirao, K. Quasi-Degenerate Perturbation Theory with General Multiconfiguration Self-Consistent Field Reference Functions. *J. Comput. Chem.* **2002**, *23* (12), 1166–1175. https://doi.org/10.1002/jcc.10050.

(105) Miyajima, M.; Watanabe, Y.; Nakano, H. Relativistic Quasidegenerate Perturbation Theory with Four-Component General Multiconfiguration Reference Functions. *J. Chem. Phys.* **2006**, *124* (4), 044101. https://doi.org/10.1063/1.2161182.

(106) Ebisuzaki, R.; Watanabe, Y.; Nakano, H. Efficient Implementation of Relativistic and Non-Relativistic Quasidegenerate Perturbation Theory with General Multiconfigurational Reference

Functions. *Chem. Phys. Lett.* **2007**, *442* (1–3), 164–169. https://doi.org/10.1016/j.cplett.2007.05.066.

(107) Zeng, T. A Diabatization Protocol That Includes Spin-Orbit Coupling. *J. Chem. Phys.* **2017**, *146* (14), 144103. https://doi.org/10.1063/1.4979902.

(108) Barca, G. M. J.; Bertoni, C.; Carrington, L.; Datta, D.; De Silva, N.; Deustua, J. E.; Fedorov, D. G.; Gour, J. R.; Gunina, A. O.; Guidez, E.; Harville, T.; Irle, S.; Ivanic, J.; Kowalski, K.; Leang, S. S.; Li, H.; Li, W.; Lutz, J. J.; Magoulas, I.; Mato, J.; Mironov, V.; Nakata, H.; Pham, B. Q.; Piecuch, P.; Poole, D.; Pruitt, S. R.; Rendell, A. P.; Roskop, L. B.; Ruedenberg, K.; Sattasathuchana, T.; Schmidt, M. W.; Shen, J.; Slipchenko, L.; Sosonkina, M.; Sundriyal, V.; Tiwari, A.; Galvez Vallejo, J. L.; Westheimer, B.; Włoch, M.; Xu, P.; Zahariev, F.; Gordon, M. S. Recent Developments in the General Atomic and Molecular Electronic Structure System. *J. Chem. Phys.* **2020**, *152* (15), 154102. https://doi.org/10.1063/5.0005188.

(109) Miyoshi, E.; Sakai, Y.; Tanaka, K.; Masamura, M. Relativistic Dsp-Model Core Potentials for Main Group Elements in the Fourth, Fifth and Sixth Row and Their Applications. *J. Mol. Struct. THEOCHEM* **1998**, *451* (1–2), 73–79. https://doi.org/10.1016/S0166-1280(98)00161-4.

(110) Sekiya, M.; Noro, T.; Osanai, Y.; Koga, T. Contracted Polarization Functions for the Atoms Ca, Ga-Kr, Sr, and In-Xe. *Theor. Chem. Acc.* **2001**, *106* (4), 297–300. https://doi.org/10.1007/s002140100278.

(111) Zeng, T.; Fedorov, D. G.; Klobukowski, M. Model Core Potentials for Studies of Scalar-Relativistic Effects and Spin-Orbit Coupling at Douglas–Kroll Level. I. Theory and Applications to Pb and Bi. *J. Chem. Phys.* **2009**, *131* (12), 124109. https://doi.org/10.1063/1.3211955.

(112) Ivanic, J. Direct Configuration Interaction and Multiconfigurational Self-Consistent-Field Method for Multiple Active Spaces with Variable Occupations. I. Method. *J. Chem. Phys.* **2003**, *119* (18), 9364–9376. https://doi.org/10.1063/1.1615954.

(113) Tech, J. L. Analysis of the Spectrum of Neutral Atomic Bromine (Br I). *J Res Natl Bur Stand Sect Phys Chem* **1963**, *67A* (6), 505–554. https://doi.org/10.6028/jres.067A.051.

(114) Coxon, J. A. The Low-Lying Electronic States of Diatomic Halogen Molecules. In *Molecular Spectroscopy*; Barrow, R. F., Long, D. A., Millen, D. J., Eds.; The Royal Society of Chemistry, 1973; pp 177–228. https://doi.org/10.1039/9781847556684-00177.

(115) Gomes, J. D. S.; Gargano, R.; Martins, J. B. L.; M. De Macedo, L. G. Relativistic Four-Component Potential Energy Curves for the Lowest 23 Covalent States of Molecular Bromine (Br_2). *J. Phys. Chem. A* **2014**, *118* (31), 5818–5822. https://doi.org/10.1021/jp4114283.

(116) Colbert, D. T.; Miller, W. H. A Novel Discrete Variable Representation for Quantum Mechanical Reactive Scattering via the S-matrix Kohn Method. *J. Chem. Phys.* **1992**, *96* (3), 1982–1991. https://doi.org/10.1063/1.462100.

(117) Pollard, W. T.; Friesner, R. A. Solution of the Redfield Equation for the Dissipative Quantum Dynamics of Multilevel Systems. *J. Chem. Phys.* **1994**, *100* (7), 5054–5065. https://doi.org/10.1063/1.467222.

(118) Arnoldi, W. E. The Principle of Minimized Iterations in the Solution of the Matrix Eigenvalue Problem. *Q. Appl. Math.* **1951**, *9* (1), 17–29. https://doi.org/10.1090/qam/42792.

(119) Reduzzi, M.; Hummert, J.; Dubrouil, A.; Calegari, F.; Nisoli, M.; Frassetto, F.; Poletto, L.; Chen, S.; Wu, M.; Gaarde, M. B.; Schafer, K.; Sansone, G. Polarization Control of Absorption of Virtual Dressed States in Helium. *Phys. Rev. A* **2015**, *92* (3), 033408. https://doi.org/10.1103/PhysRevA.92.033408.
(120) Kobayashi, Y.; Zeng, T.; Neumark, D. M.; Leone, S. R. NaI Revisited: Theoretical Investigation of Predissociation via Ultrafast XUV Transient Absorption Spectroscopy. *J. Chem. Phys.* **2019**, *151* (20), 204103. https://doi.org/10.1063/1.5128105.